Mari Vassdokken Sigstad

A Numerical and Experimental Study of a Multi-torus Floating Solar Island Concept

June 2019

Master's thesis

Master's thesis

2019

Mari Vassdokken Sigstad

NTNU
Norwegian University of
Science and Technology

NTNU
Norwegian University of
Science and Technology

NTNU
Norwegian University of Science and Technology

A Numerical and Experimental Study of a Multi-torus Floating Solar Island Concept

Mari Vassdokken Sigstad
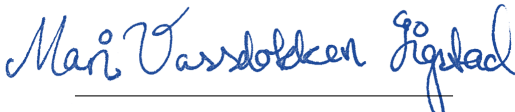
Preface

This Master's thesis is the final project of my Master of Science degree in Marine Hydrodynamics at the Department of Marine Technology, Norwegian University of Science and Technology (NTNU) in Trondheim, Norway. The work is carried out during the spring of 2019 and is a continuation of the preliminary project thesis carried out during the autumn of 2018. The workload of the thesis is corresponding to 30 ECTS.

The topic and the present multi-torus concept were suggested by Professor Trygve Kristiansen. He has also been my supervisor during the complete project with the project thesis and Master's thesis. Prof. em. Bruce Patterson and Prof. em. Frode Mo provided the main idea of a floating solar island concept furnishing energy for the production of solar fuel on an FPSO.

The reader should have basic knowledge about hydrodynamics and structural dynamics.

Mari Vassdokken Sigstad

Trondheim, June 11, 2019

Acknowledgements

Summary

Small scale model tests for a multi-torus concept, designed as a platform for a floating solar island, have been conducted with and without the solar panel deck modelled as a membrane. Models are tested in regular and irregular waves. The hydro-elastic response is investigated through measurements with a Qualisys motion capture system. The behaviour of the models was also methodically documented through videos of all regular wave series. Numerical implementation of a coupled truss and floater model in Python is rendered by the use of the Implicit-Explicit Euler and 4th order Runge-Kutta method as numerical time integration schemes. Verification studies during the implementation of the truss model are conducted using simple 2-dimensional cases with known dynamic behaviour. The coupled numerical model was debugged using a single moored torus, where the mooring lines are modelled using trusses.

Since the multi-torus has never been tested with a solar panel deck previously, one of the main goals of the experiments was to document the effect of the membrane on the multi-torus floater previously studied. The experimental results show that the membrane does not significantly affect the response of the model. In surge, a resonant behaviour has been observed. The natural period in surge is approximated to 2.71s and 2.39s with and without membrane respectively. This corresponds well with the position of the resonance peak. Both heave and pitch responses from the model tests are compared to a zero-frequency theory (ZFT) for a single floater. Results are corresponding well. For increasing wave numbers, a phase shift of the results compared to the theory is observed. In addition, the shape of the RAO changes. This can be explained by that the ZFT used only corresponds to the RAO of a single-torus. The response of the ovalizing modes shows that the model has a limited response in the horizontal radial direction, which is beneficial for the equipment mounted on the platform.

Results from irregular wave tests show that the calculated vertical RAOs correspond well with the results presented for regular waves. However, the response spectra from irregular wave tests are influenced by higher order effects for increasing wave numbers. The results also show that the higher order effects are larger for the model with membrane. Overtopping, water that floats over the tori, has previously been regarded as one of the main challenges of the multi-torus concept. Especially since it is a non-linear behaviour which is difficult to estimate. Comparison with mooring parameters from previous studies shows that overtopping is highly dependent

on pre-tension and the spring stiffness of the mooring lines. This is an interesting subject for further studies. The numerical implementation of the truss model is able to correctly describe the behaviour of simple systems with known dynamic behaviour. Unfortunately, the coupled truss and floater model has an unresolved bug that causes the geometry to explode and the results to become non-physical. Even after countless attempts, the error has not been found. Therefore, the numerical simulation model could not be used to compare the results with the model tests.

Concluding remarks can be summarized by the multi-torus concept both with and without showing potential for the wave conditions investigated. The models follow the waves well and the elastic properties of the design can be considered an advantage. Including the membrane did not change the behaviour in any significant way and the multi-torus interconnected with trusses has little ovalizing behaviour, which is beneficial for the equipment on the solar panel deck.

Sammendrag

En flytedel som skal brukes til plattform for en flytende soløy er testet i modellskala både med og uten solcellepaneldekket. En realistisk skalert membran er brukt for å tilsvare dekket. Begge modellene ble testet både i regulære og irregulære bølger, og den hydroelastiske responsen ble målt ved bruk av Qualisys-markører som målte bevegelsen i 3 retninger. Oppførselen til modellene ble også systematisk dokumentert på video. En numerisk modell som kopler en tidsavhengig fagverksmodell og flytermodell er implementert i Python. De numeriske integrasjonsmetodene Implisitt-Eksplisitt Euler og 4. ordens Runge-Kutta, henholdsvis, er brukt til å finne bevegelsen til modellen ved å løse hvert tidssteg i en simulering. Den koplete numeriske modellen ble feilsøkt ved bruk av én forankret sirkulær flyter, der forankringene er modellert ved bruk av fagverksbjelker. Enkle 2D-tilfeller med kjent dynamisk oppførsel er også brukt til å verifisere fagverksmodellen før den ble koplet med flytermodellen.

De eksperimentelle resultatene med regulære bølger viser at modellen oppfører seg svært likt med og uten membran. I jag er det observert en resonanstopp. Egenperioden i jag er tilnærmet til 2.71s og 2.39s med og uten membran henholdsvis. Dette stemmer godt overens med posisjonen til resonanstoppen. Resultatene viser at bevegelsen i svai er begrenset, og antagelsen om at disse kan neglisjeres i den numeriske modellen er derfor bekreftet. Både hiv og trim-respons er sammenlignet med en null-frekvens teori (ZFT) for en enkelt flyter og stemmer godt overens med denne. For økende bølgetall ser man en faseforskyvning av resultatene sammenlignet med teorien og i tillegg endres fasongen på responskurven. Dette skyldes at teorien kun er tilpasset én flyter, sammenlignet med fem som den testede modellen har. Responsen i ovaliserende moder viser at modellen har veldig begrenset respons i horisontal radiell retning, noe som er positivt for utstyret og solcellepanelene som skal festes på toppen av flyteren. Tester med én flyter har tidligere vist at ovalisering kan være et problem og det er derfor positivt at denne modellen viser forbedring i forhold til dette. Legg også merke til at bølgemålerne viser at desto mindre bølgene generert av bølgemaskinen er, desto større usikkerhet er det knyttet til at amplituden er lik input.

Resultatene fra irregulære bølgetester samstemmer med de regulære bølgetestene, men responsspektrene er påvirket av høyere ordens krefter for økende bølgetall. Spektrene viser også at det er knyttet større høyere ordens krefter til modellen med membran enn uten. Overtopping,

vann som slår over flyterne, har tidligere vist seg å være en av hovedutfordringene ved konseptet, fordi dette er ulineær oppførsel som er vanskelig å beregne. Ved å sammenligne parametrene fra tidligere studier viser det seg at overtopping er svært avhengig av forspenningen og stivheten i forankringslinene. Observasjoner fra modelltestene viser at overtoppingen avtar når stivheten i forankringslinene og forspenningen avtar. Dette bør studeres nærmere. De numeriske verifikasjonsstudiene viser at implementasjonen av fagverksmodellen klarer å fremstille enkle dynamiske modeller med riktig resultat i forhold til teorien. Dessverre har den koplede flyter- og fagverksmodellen en feil i implementasjonen som gjør at geometrien eksploderer og resultatene blir ikke-fysiske. Selv etter utallige forsøk er feilen ikke funnet, og modellen kunne derfor ikke brukes til å sammenligne resultatene med modellforsøkene.

For å konkludere viser multi-torus modellen potensial, selv med membran klarer den å beholde de elastiske egenskapene som skal til for å følge bølgene den blir utsatt for på en god måte. Den begrensede ovaliseringen er også positiv for utstyret som skal installeres på toppen av flyteren. Videre studier med fokus på å optimalisere dimensjonering bør være neste steg.

Table of Contents

Nomenclature

Abbreviations

$\frac{H}{\lambda}$ Wave steepness [-]

2D   Two-dimensional

3D   Three dimensional

CO2   Carbon dioxide

D   Wave diffraction

FK   Froude-Kriloff

LST   Low-frequency slender body theory

ODE   Ordinary differential equation

PSD   Power-spectral density

PV   Photovoltaic (type of solar panels)

Q   Source density constant

RAO   Response amplitude operator

RK4   Runge-Kutta 4$^{\text{th}}$ order method

SWL   Still water level

ZFT   Zero-frequency theory

Greek Letters

α_n Constant dependent of mode n, $\alpha_0 = 2, \alpha_n = 1$ for $n \geq 1$

β Angle used to describe angular position on torus (see figure 2.3)

η_1 Surge motion (x-direction)

η_2 Sway motion (y-direction)

η_3 Heave motion (z-direction)

λ Wave length $[m]$

ω Wave frequency $[s^{-1}]$

ϕ In general, velocity potential

ϕ^F Far-field description velocity potential

ϕ^N Near-field description velocity potential

ϕ_0 Incident wave velocity potential

ϕ_I^F Inner expansion of far-field description velocity potential

ρ Water density in fresh water, $1000 kg/m^3$

σ Standard deviation

ζ_a Wave amplitude $[m]$

Roman Symbols

$\ddot{a}_n(t)$ Vertical acceleration of mode n

$\hat{s}_k$ Tangential unit vector of truss k

$a_{33}^{(n)}$ Vertical added mass for mode n

$a_n(t)$ Vertical motion of mode n

a_{11} Added mass in surge

b_w Cross-sectional diameter, $2c$ $[m]$

c Cross-sectional radius of torus

EI Floater/Torus bending stiffness

$f_3^{\text{added mass}}$ Vertical force from added mass

f_3^{exc} Vertical wave excitation forces

f_3^{truss} Vertical truss forces

g Gravity, $9.81 m/s$

H Wave height, $H = 2\zeta_a$

h Water depth $[m]$

$H(\omega)$ Transfer function representing the response amplitude operator in irregular waves

H_s Significant wave height

J_n — Bessel function of first kind, order n

k — Wave number $[m^{-1}]$

kR — Wave number k times the radius of the outer torus, $R = 0.5[m]$

l_k — Length of truss number k

l_{0k} — Initial length of truss number k

m — Mass per unit length $[kg/m]$

$m_{i,j}$ — Mass of node i, j

n — In subscript n means mode number, while in superscript n means time step number

N_H — Number of mooring lines/trusses attached to floater

R — Radius of the outer torus, $R = 0.5[m]$

T — Wave period $[s]$

T_f — Full-scale wave period $[s]$

T_k — Tension of truss number k

T_{1n} — Natural period of multi-torus in surge

V_n — Velocity normal to body

w — Vertical motion

M — Total mass of model

Chapter 1

Introduction

According to *The Sustainable Development Goals* (SDGs) of the United Nations Development Programme [UNDP, 2015], *Affordable and Clean Energy* (No. 7) is a necessity of the near future. As the access of energy increases throughout the world and the world's population is still increasing, the need for larger amounts of energy every year makes it necessary to create reliable, affordable and clean energy sources. [UNDP, 2015] states that fossil fuels are causes of climate change and renewable energy sources as solar and wind are the future. [Lewis and Nocera, 2006] estimates that global energy consumption will increase from 13.5 TW in 2001 to 27 TW within 2050. As climate change becomes a fact and the world's oil reserves decrease, there are few other known options that are as interesting as solar and wind energy. Also, taking into account the limited amount of land areas, offshore wind and floating solar energy plants can be more optimal alternatives. To be able to supply 27 TW of energy within 2050, which is an increase of about 10 TW from 2016, it would be necessary to install 20 million 10MW wind turbines [Kristiansen and Borvik, 2018]. This signifies an installation rate of 2000 turbines a day for the next 30 years, which is unrealistic considering the status of expansion. A solar plant of 10 TW is estimated to cover approximately 500x500 [km^2] with a panel efficiency of 20 % [Kristiansen and Borvik, 2018]. That is manageable considering the enormous amounts of surface area available in the oceans.

[Patterson et al., 2015, p.76] proposes a concept of an artificial floating island which supports a membrane of photovoltaic (PV) panels producing solar energy and further powers a factory of synthetic methanol either on a Floating Production Storage and Offloading unit (FPSO), as illustrated by 1.1. Synthetic methanol can be produced through an electrochemical process of capturing CO2 in seawater. By recycling CO2 from seawater, this creates a zero-emission process where equal amounts of carbon are used in production as burned through consumption. Liquid fuel from methanol has about half the energy density of gasoline [Goeppert et al., 2014], which means it is a good alternative to fossil fuels. The concept proposed needs a convenient marine floater which can support impact from waves up to a significant wave height $H_s = 7$m.

In this master thesis, an experimental and numerical study of a floating solar island concept will be presented. The motivation is to contribute to the research of an adequate marine platform which is affordable and suited to the demands of wave conditions. Model tests will be conducted to investigate the seakeeping properties of the concept. Numerical implementation of a coupled truss and floater model will have the intention to better describe the motion of the concept numerically than what is possible with existing models. Verification studies using simple famous dynamic models will be used to test the truss model, before implementing the floater model. The future goal is to gradually be able to compare a numerical model of increasing complexity with the model tests, to verify the behaviour of the concept in waves.
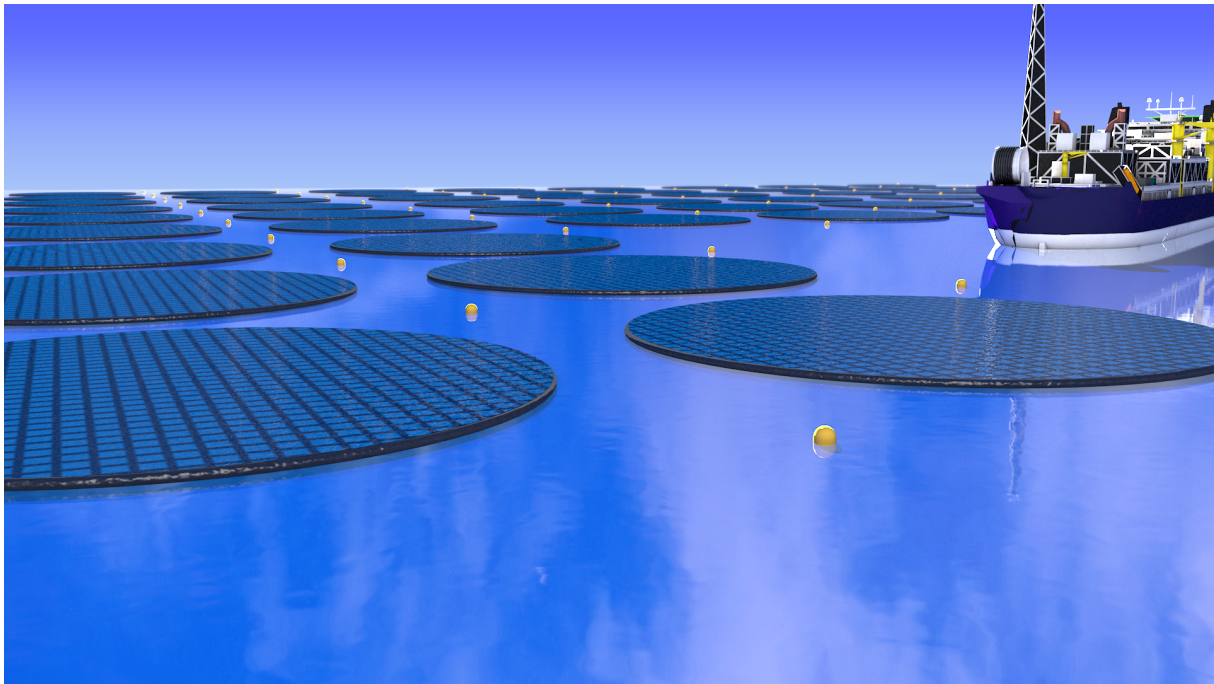
Figure 1.1: Illustration of solar island production plants installed in a facility and connected to FPSO for production of solar fuels. Idea by Bruce Patterson & Frode Mo. Courtesy of [Frode Mo, 2019].

1.1 Objectives

As only limited research is performed concerning a multi-torus floating solar island concept previously, this master's thesis will investigate the hydro-elastic response of the multi-torus concept, with and without a solar panel deck, in wave conditions of interest. Responses in regular and irregular waves are investigated through small-scale model tests with a developed multi-torus model. The multi-torus concept is a model consisting of five circular elastic tori interconnected through pre-tensioned elastic trusses. A weighted membrane will be used as a scaled version of a solar panel deck. In addition to measurements with a Qualisys motion capture system, the behaviour of the model will be observed and documented through videos of all wave series in regular waves. This will permit to document overtopping behaviour thoroughly, with focus on differences between the model with and without membrane.

A numerical implementation of a moored torus model by use of the truss model [Marichal, 2003] and the floater model based on zero-frequency theory (ZFT) [Faltinsen, 2011] will be attempted in the open-source object-oriented programming language Python. Numerical methods like the Implicit-Explicit Euler and 4th order Runge-Kutta (RK4) will make it possible to simulate the behaviour of the model in regular waves.

The project is a continuation of a preliminary study performed from August to December 2018. With the goal to contribute to the present knowledge of the behaviour of a multi-torus floating solar island concept, the main objectives of this master's thesis are summarized by the following steps:

1. Present a background and previous research relevant to this master's thesis

2. Give an overview of the theoretical approaches used in the model tests and in the numerical implementation of the floater and truss models, in addition to the numerical methods used

3. Conduct small scale model tests with an improved multi-torus model with and without a weighted membrane to investigate the behaviour of the model in regular and irregular waves, as well as the effect of the membrane

4. Implement a coupled floater and truss model in Python by use of numerical ordinary differential equation solvers, making it possible to simulate a single-torus model attached by mooring lines exposed to regular waves

5. Verify the implementation of the numerical models using case studies with known dynamic behaviour and compare experimental results with earlier studies

1.2 Scope

The scope of this master's thesis is limited to small scale model tests in regular and irregular waves. The Small Towing Tank, *Lilletanken*, will be used for the purpose. Two multi-torus models will be tested. One consisting of the five interconnected tori attached to a set-up of four symmetrically positioned mooring lines and the other with a weighted membrane stretched over the surface and attached to each torus. Current is assumed to have negligible effects on the model and will therefore not be tested.

Limiting the complexity of the numerical implementations, only vertical external forces from the floater model will be implemented. Sway is assumed to be negligible, while surge response has not been accounted for. The complete multi-torus will not be implemented in the numerical code, due to the complexity of the geometry. A single torus attached to mooring lines modelled by trusses will be a first verification of the code.

1.3   Outline of Master's Thesis

This section will briefly describe the structure of this master's thesis.

Chapter 1 further includes a background study and previous research on Solar Islands.

Chapter 2 consists of theoretical approaches and models used in the thesis. This includes theory on which experimental assumptions are based on and the theoretic models behind the numerical simulations.

Chapter 3 presents the numerical implementation of the model, as well as numerical iteration methods and comparative solutions of the case studies used to verify the numerical model.

Chapter 4 includes the presentation and planning of the model tests.

Chapter 5 presents and discusses the results of the experiment and numerical simulation.

Chapter 6 draws conclusions from the study carried out in the thesis and suggests topics for further research.

Appendix A furnishes the reader with additional theory.

Appendix B includes additional tables.

Appendix C presents the set-up and observations of the model tests conducted in November, during the work with the project thesis.

Appendix D includes additional information about the numerical verification studies, as well as the 12 truss case used for testing of the coupled truss and floater model.

Appendix E presents additional numerical results from verification studies.

Appendix F consists of additional plotted results from the experiment.

1.4 Background

The section will describe the main parts included in the floating solar island concept studied and present the previous studies done on the subject. An alternative platform concept that is under current research is also presented briefly.

1.4.1 Solar Energy and PV cells

According to [Lewis and Nocera, 2006], renewable energy and especially solar energy is the most future-oriented energy source, regarding the climate goals of reducing CO2 emissions. Other possibilities as nuclear plants are not realistic since one would have to install a new plant almost every day for the next 40 years to increase the production only by 10 TW. This is the least increase needed to keep the emission levels where they are today, not even accounting for reduction according to the climate goals. Other renewable sources as wind is a good alternative to contribute to a more carbon neutral future. Increasing global energy production by 10 TW using only wind energy alone, it is necessary to install more than 2000 wind turbines a day for the next 30 years. In addition to this, there is a need for large surfaces as illustrated on the right-hand side of figure 1.2.

According to *DNV GL Energy Transition Outlook - Renewables, Power and Energy Use Forecast to 2050* [DNV-GL, 2017], solar photovoltaic (PV) energy will dominate the global electricity production. Together with the other renewable sources, it will account for 85% of the global electricity production in 2050. The energy efficiency of PV cells is currently around 22% [DNV-GL, 2017] and is expected to increase due to new advanced technology. Solar energy is promising due to its reliability in areas with high insolation per year. Additionally, the amount of solar energy available is without bounds. A floating solar plant of 10 TW is estimated to cover about 500x500 $[km^2]$ [Kristiansen and Borvik, 2018]. This is a realistic perspective confirmed by figure 1.3, that shows the enormous ocean areas that satisfy the wave conditions assumed.

The challenges of solar energy are mainly cost efficiency, available surface and storage. PV panel technology has been too expensive for solar energy production at a large scale to be cost-effective earlier. As material technology is developing, new and effective absorbing materials better suited for large scale more cost-efficient production are being developed. [DNV-GL, 2017] estimates that the technology and price of PV panels will not be a scaling factor of the increase in solar energy production over the next 30 years.

1.4.2 Storage and solar fuels as an alternative

There exist three possible storage concepts according to [Lewis and Nocera, 2006]. These include battery storage, solar thermal technology and an artificial photosynthesis process which transforms solar energy into liquid fuel. Batteries are expensive, the weight-size capacity ratio is low and reliability is a problem as the battery ages. Thus, batteries are not well suited for large scale storage. For thermal technology to be an efficient option, more efficient materials
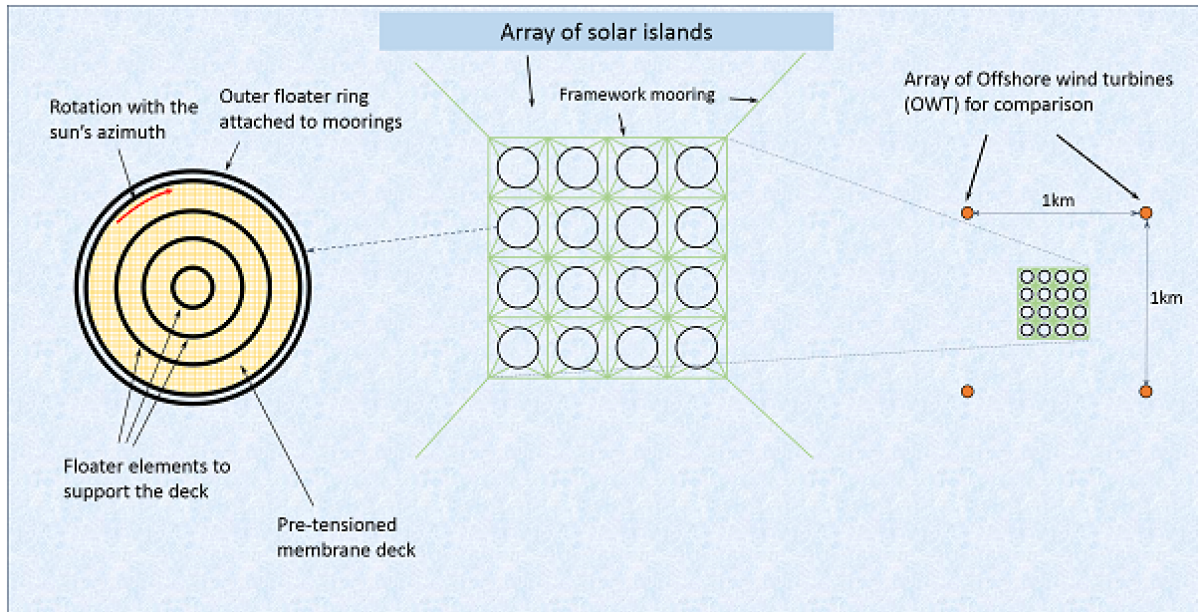
Figure 1.2: Illustration of the proposed concept as an array of floating solar islands. The figure shows a concept like the multi-torus in an array of several solar islands connected in a mooring framework. This is a possible mooring arrangement inspired by the fish-farming industry. It also illustrates how a floating solar energy plant will cover significantly smaller surface areas than what an offshore wind turbine park does. [Kristiansen et al., 2017]

than what exists today are needed. Transformation of solar energy to synthetic fuel in the form of hydrogen or methanol is a futuristic option. CO_2 can be transformed into liquid methanol through an electrochemical process. Methanol can easily be used as fuel in existing fossil fuel burning engines, with only simple modifications. This is a huge advantage, as it currently does not exist any alternative to fossil fuels that can supply the extreme amounts needed in the shipping and aeroplane industries. The density of energy in methanol is about half the density of gasoline [Goeppert et al., 2014]. There exist few other alternatives which have as high energy density as methanol. [Kristiansen and Borvik, 2018] states batteries, solar thermal technology, transformation to biofuel, hydrogen or liquid carbon-based solar fuels as options for energy storage in connection to solar energy. But the only option with global potential as liquid carbon-based fuels.

[Patterson et al., 2015] proposes an idea of production of solar fuels like methanol on FPSOs, connected to floating solar islands on the sea surface like illustrated in figure 1.1. The density of CO_2 in seawater is significantly higher than in air, which makes it possible to extract huge amounts through an electrochemical process powered by the electricity produced on the solar islands. For this to be possible, the islands must be situated at a location where the currents in the water are large enough to supply sufficient amounts of CO_2 to be extracted without affecting the vivid environment in the sea.
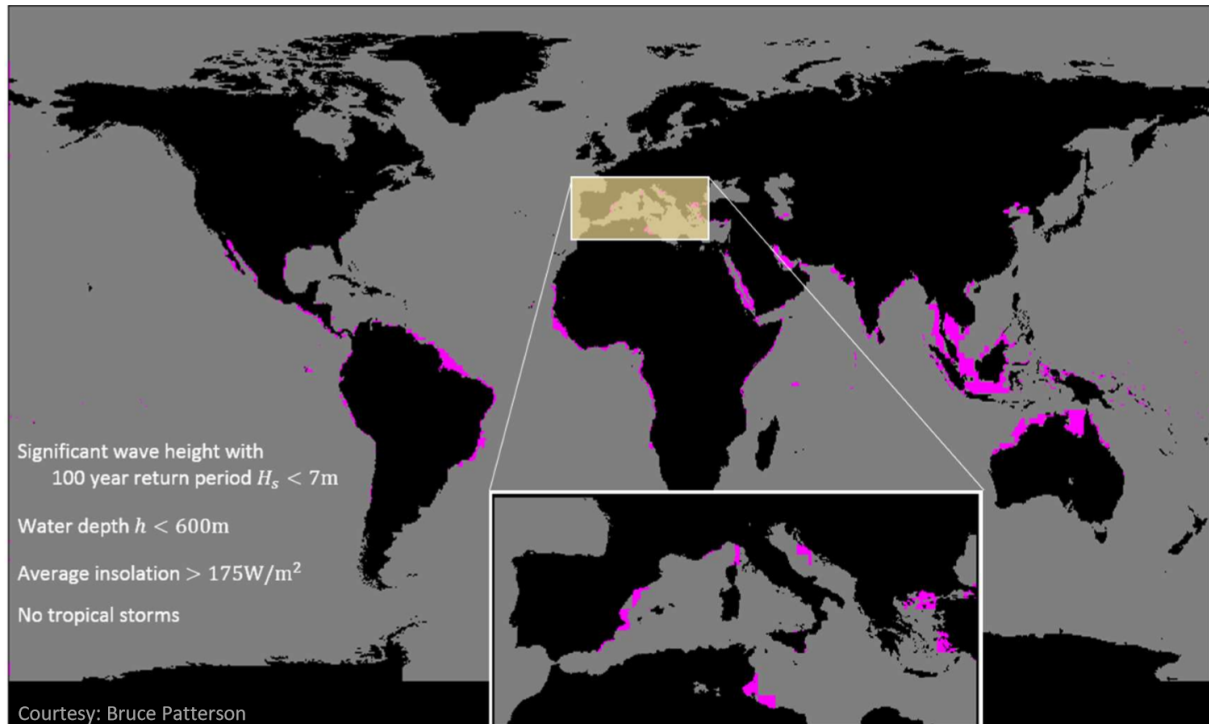
Figure 1.3: Illustration of ocean areas which satisfies the conditions of having a floating solar island. It points out all sea surfaces over the world which has a significant wave height with 100 year return period lower than $H_s < 7$ [m], an average insolation larger than 175 [W/m^2], a water depth lower than $h < 600$ [m] and no tropical storms. Courtesy of B. Patterson. [Kristiansen and Borvik, 2018]

1.4.3 Floating Solar Islands

Several concepts of floating solar islands have been proposed over the last few years. The concepts vary in size, design and operation limits. It is proposed to connect the solar energy plants directly to the power grid in proximity to ocean-near cities in need of energy sources. This is interesting for cities which are lacking surface space to produce sufficient amounts of electricity. Developing a storage option as the ones already mentioned is also a researched possibility. Figure 1.3 points out all sea surfaces over the world which has a significant wave height with 100 year return period lower than $H_s < 7$m, an average insolation larger than 175W/m^2, a water depth lower than $h < 600$m and no tropical storms. This is all areas that [Patterson et al., 2015] assume can be well suited for installation of floating solar islands.

For this to be realised, a stable marine platform which can operate in $H_s < 7$ [m] is necessary to design. A possible design is the multi-torus which will be studied in this thesis. The structure must withstand wind, wave and current forces according to the 100 year return period of the location. The design also needs to be simple enough for production to be affordable and competitive. Figure 1.2 shows a stand-alone concept like the multi-torus in an array of several solar islands connected in a mooring framework. This is a possible mooring arrangement

inspired by the fish-farming industry. The right part of figure 1.2 also illustrates how a floating solar energy plant will cover significantly smaller surface areas than what an offshore wind turbine park does. Four 10 MW offshore wind turbines covering a surface of $1km^2$ corresponds to an equally producing solar plant covering 1/4 of the area if 20 % panel efficiency is considered [Kristiansen and Borvik, 2018]. Included in the idea, a rotation of the island with the sun's azimuth to keep the angle of the sun rays optimal on the PV panels is subject of investigation.

1.4.4 Solar panel deck

An eventual artificial island concept must include a deck which can carry the weight of the solar panels. This has not been included in earlier research on the multi-torus concept studied. A weighted membrane is used in the model tests of this study to simulate the properties of a deck. Elastic properties of the deck are important, such that it can handle the motions of an elastic floater and have limited influence on the elastic properties of the floater. It is ideal that the complete model follows the sea surface motions as much as possible. The deck needs to be pierced or not water-tight in some way such that rainwater or eventually flooded seawater can be drained as fast as possible. A pre-tensioned deck is proposed, in order to avoid snap loads. A pre-tensioned membrane deck is proposed included in the left-hand side of figure 1.2. Further studies are necessary to investigate whether slamming can be a problem for the deck or the solar panels mounted on the deck.

Curiosity is related to how a pre-tensioned deck can change the behaviour of the multi-torus concept which will be studied here. The eigenfrequencies the model will have including a pre-tensioned membrane is also of interest, but will not be further looked into in this study. In full scale, a type of material which can match the elastic properties of the model scale needs to be used. This could be some kind of aquaculture nylon net for example. Challenges related to ageing and durability in seawater must be considered.

1.4.5 Challenges

There is a wide range of challenges which might be relevant in the design process of a suited marine platform to be used as a floating solar energy plant at sea. The structure needs to withstand wind and wave loads from the environment. Current loads are not considered as a problem, as the draft is very limited in the proposed concept. Wind loads can be an issue related to the membrane deck supporting the solar panels. These loads may lift the platform out of the water surface, which can cause large slamming loads or resonance effects on the structure. This again can lead to fatigue damage, local or global fractures.

It is desired that the model moves as much with the sea surface as possible, instead of working against the motions of the waves. This increases the complexity of the design process, as numerous possibilities of sea conditions need to be accounted for. Problematic related to overtopping is especially interesting in relation to this. Overtopping occurs when the model does not follow the wave conditions completely and as water follows the top surface of the

structure, flooding parts of it. This might be relatively undramatic if there are only small amounts of water and it follows the structure. In worse cases, this may cause flooding of larger parts of the structure, critical mooring loads, sea spray or slamming loads on the PV panels and again damage on the structure. To avoid this, the model needs to be relatively flexible.

Salt sea water on the PV panels in case of flooding or sea spray is another issue. It is a well-known phenomenon that metals, electricity, water and salt has a high probability of malfunction and corrosion. This means some kind of coating technology must be applied for the PV panels to avoid corrosion or short-circuiting.

Sloshing effects between the floaters are another issue, as in the multi-torus model where there are several watertight tori placed one inside the other. Large wave motions can cause sloshing effects between the rings. This causes large forces which might lead to resonance motions. In general, all types of resonance motions should be avoided as far as possible. No sloshing or slamming has been observed in earlier model tests with the multi-torus. Asymmetry in the model geometry due to large mooring line forces can also cause problems. This can cause yaw resonance motions and ovalization due to large surge/sway motions. A thorough resonance study is therefore important to accomplish before the project is further developed.

In total, the challenges mentioned above are just a few of a large amount of small and large problems which needs to be studied in detail before a full-scale island can realized.

1.5 Previous research on Solar Islands

[Newman, 1977] first introduced studies of motions of a floating slender axisymmetric torus. He introduced a slender-body theory under the assumptions of axisymmetry and that the incident wavelength is comparable with the radius of the cross-section and much smaller than the radius of the complete tori. [Faltinsen, 2011] developed a 3D slender body theory considering the hydro-elasticity of a single-torus. Matched asymptotic expansions with a far-field and near-field descriptions are used, and by this follows that strip theory is appropriate. The study was motivated by the desire of moving fish farms to sites exposed to larger waves and the single-torus was used to model a single or two closely spaced circular floating collar of a fish farm. This made the basis for further studies concerning a single-torus by [Li and Faltinsen, 2012].

1.5.1 Single-torus

[Li and Faltinsen, 2012] developed a 3D low-frequency slender body theory for the vertical added mass, damping and wave excitation loads. The calculated loads on an elastic semi-submerged torus were derived by asymptotic expansions and a Haskind-type expression for the wave excitation loads was presented. 3D frequency-dependent interaction was shown to be significant on the scale of the torus diameter and hydro-elasticity was confirmed to be important in the studied case of the single-torus. Further, [Li et al., 2014] presented results of experiments and numerical simulations of a moored single-torus. The experiments were conducted with
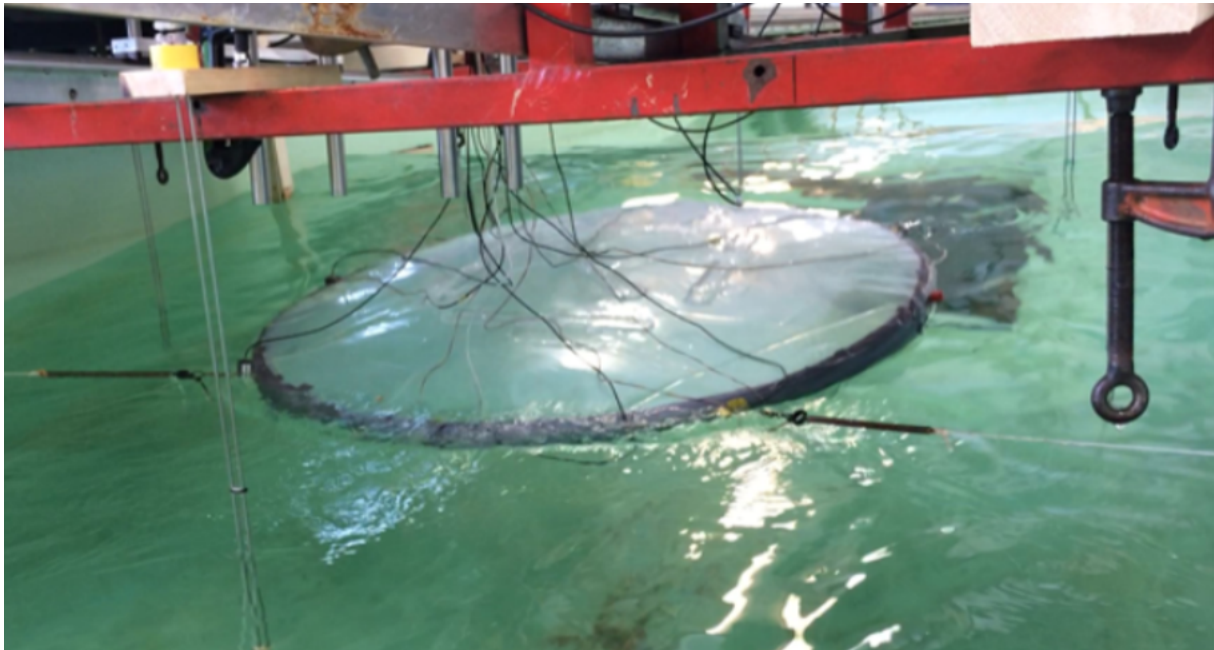
Figure 1.4: Model of air-cushion supported solar island tested in *Lilletanken* with regular waves. Mooring-line springs, forces rings and devices measuring motion. Courtesy of [Kristiansen and Brovik, 2018].

different regular wave conditions defined by the wave period and steepness. Local overtopping on the torus was observed in steep wave conditions. Vertical acceleration components were studied. Higher order harmonic acceleration components were found from experiments and matched with second-order harmonic acceleration components using the weak-scatter method for all other wave steepnesses than the highest one tested ($H/\lambda = 1/15$). Predictions of higher order vertical accelerations corresponded less with the experimental results.

[Li, 2017] developed a low-frequency linear slender-body theory (LST) for vertical radiation loads on an elastic semi-submerged torus. The study consisted of theoretical approaches, numerical simulations and experiments. The previously mentioned reports were used as a basis for the theory and it is verified by numerical simulations using WAMIT. The analysis showed that there is a strong dependency related to hydrodynamic frequencies, and essential to consider hydro-elasticity for the vertical wave loads and responses of the torus considered in the study. Experiments with two models of different flexibility were conducted. Overtopping and water-exit of the torus was observed. The results showed a good correlation between theory, numerical studies and experiments for linear response, but not a satisfactory correlation between numerics and experiments for the non-linear response. The two latter reports also consider the single-torus as a circular floating collar of a fish farm.

1.5.2   Air-cushion supported solar island

[Kristiansen and Brovik, 2018] studied a single-torus covered by an air-supported membrane. The model was called an air-cushion supported solar island, where the membrane should carry the weight of PV panels. A vertical skirt was added along the outer part of the torus to avoid air leakage. Model tests in regular and irregular wave conditions were conducted. A picture of the model exposed to regular waves is shown in figure 1.4. The study investigated the general behaviour of the model, as well as failure modes. Overtopping with flooding as a consequence was observed at certain wave conditions. Out-of-water incidents of the vertical skirt were not observed, but air leakage due to a fissure of the membrane might be an issue over time. A modal analysis comparing the first flexible mode motions to theory using linear potential flow assumption was validated for global behaviour, but important nonconformities were found. Due to these results, a change in the concept idea to the multi-torus design was suggested.

1.5.3   Multi-torus

[Windsvold, 2018] built, tested and studied a multi-torus model of small scale under supervision of Prof. T. Kristiansen. The model was built consisting of five concentric cylinders, connected together by pre-tensioned nylon-covered rubber bands at eight angular positions symmetrically around the tori. Mooring lines consisting of elastic springs were attached at four symmetric angular positions during testing. Both a model of a single-torus and a multi-torus were tested in different regular and irregular wave conditions. The results from the two different models were compared and in addition, the low-frequency linear slender-body theory [Li, 2017] was compared to the resulting vertical radiation loads. The zero frequency theory of [Faltinsen, 2011] was also used for comparison.

The experimental results of the single-torus corresponded well with the predictions of linear theory. Concerning test results with the multi-torus, there was a certain agreement to theory for response in long wave periods. However, the results from wave-interaction in small wave periods showed that the vertical motion of the model relative to the wave amplitude was lower than the theoretical prediction indicated. This was based on response theory of the single-torus. The main challenge was overtopping of the outer aft torus in certain of the larger regular wave conditions tested. In irregular waves, the overtopping phenomenon occurred at random positions around the tori, but most frequently at the fore of the two outer tori. There was also a less clear tendency of which wave conditions that caused overtopping in irregular waves compared to regular waves.

[Windsvold, 2018] concluded that the multi-torus design studied has potential, but that more research is needed to be able to develop a functioning design of a floating solar island. By suggestion from supervisor Prof. T. Kristiansen, the previous studies resulted in this study. The multi-torus previously used by [Windsvold, 2018] is first reused during observation tests in November. Then, necessary changes to optimize the model is completed and a membrane is

designed an built during this thesis. The new multi-torus model will be tested in regular and irregular waves with and without the membrane simulating the solar panel deck in the further studies. Numerical implementation and coupling of a floater model based on the ZFT developed by [Faltinsen, 2011] and the truss model developed by [Marichal, 2003] will also be part of this study.

1.5.4 Alternative concept by Moss Maritime

An alternative concept to the multi-torus design has been suggested by Moss Maritime. This concept consists of several connected standardized modules. The barge-like modules are rectangular and will be connected into a large grid of modules. The modular design is said to ease construction and repair, as all modules are equal and connected together through links such that each module can be changed individually. The size of the solar park can be customized, according to desired power demand and availability of surface at the location [MossMaritime, 2018]. An artistic impression of the solar island is given in figure 1.5. The concept is currently under study at the Department of Marine technology, as part of a master thesis by Magnus Onsrud, under supervision of Professor T. Kristiansen.
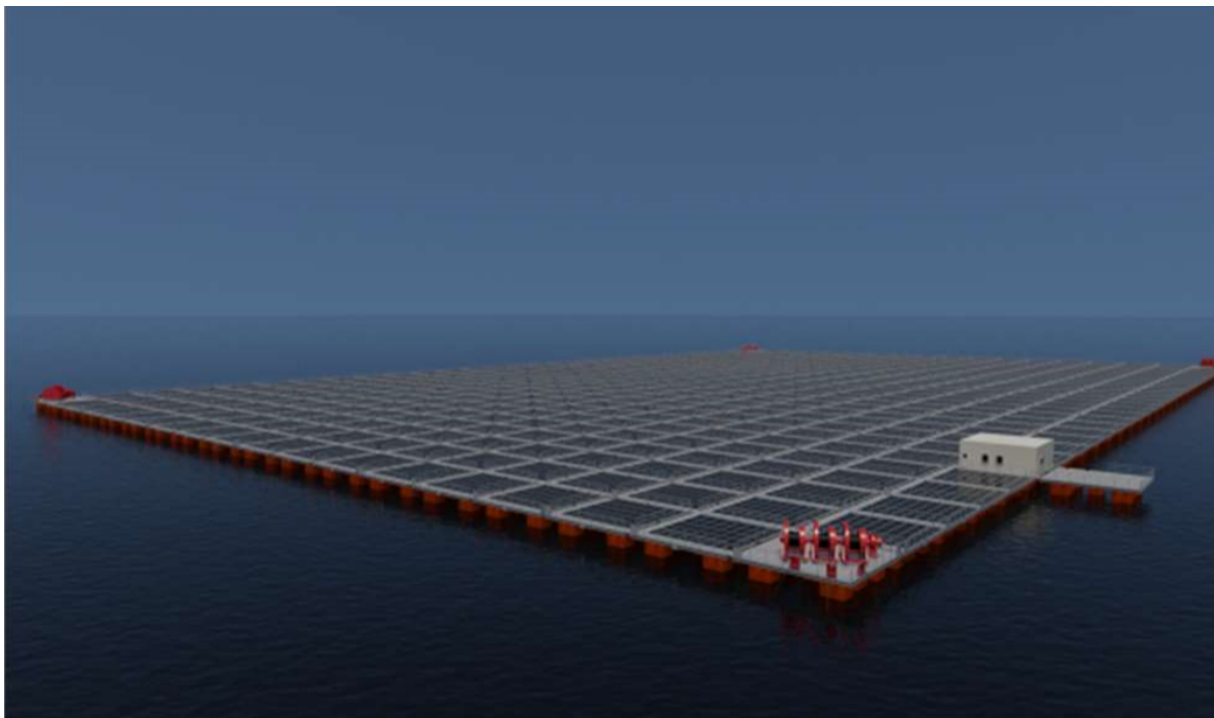
Figure 1.5: An artistic impression of the solar island concept from Moss Maritime. This concept consists of several connected standardized modules. The barge-like modules are rectangular and will be connected into a large grid of modules. The modular design is said to ease construction and repair, as all modules are equal and connected together through links such that each module can be changed individually. Courtesy to [MossMaritime, 2018]

Chapter 2

Theory

In this chapter, the theory which leads to the numerical implementation and model tests will be presented and described. All relevant theory has been derived and developed by others but is essential as a basis for both the experimental and numerical study. Additional theoretical approaches as regular wave theory and Froude scaling can be found in Appendix A.

2.1 Wave generation

The wavemaker installed in *Lilletanken* and used during the model tests is a piston wavemaker. A simplified theory for plane wavemakers in shallow water is proposed by Galvin (1964), and presented in [Dean and Dalrymple, 1984]. The same theory is used to calculate the stroke of the wavemaker used in the model tests. Figure 2.1 defines the parameters used to find the stroke S of the wavemaker. Galvin (1964) proposes that *"the water displaced by the wavemaker should be equal to the crest volume of the propagating wave form"* [Dean and Dalrymple, 1984].
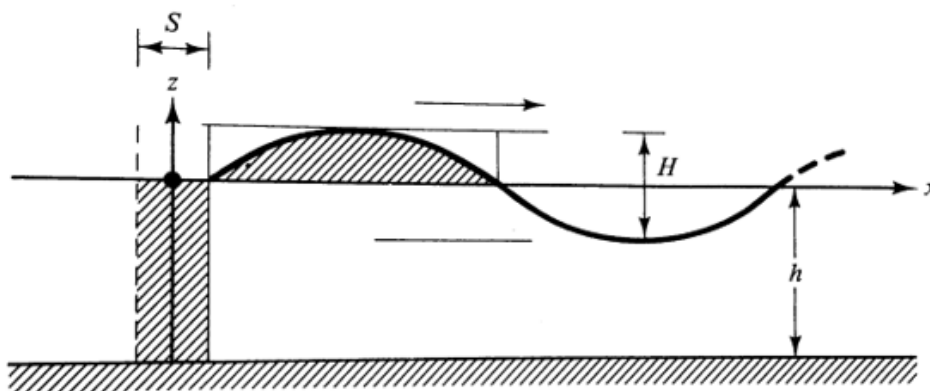
Figure 2.1: Plane piston wavemaker in shallow water. S is stroke, H is wave height and h is water depth in the figure. Theory by Galvin (1964), courtesy to [Dean and Dalrymple, 1984]

$$Sh = \frac{H}{k} = \frac{H}{2} \left(\frac{\lambda}{2}\right) \frac{2}{\pi} \tag{2.1}$$

This leads to equation (2.1), where H is wave height, h is water depth, k is wave number and λ is wavelength. A factor of $\pi/2$ is included to account for the ratio of the shaded area on the wave in figure 2.1. The relation presented is valid for $kh < \pi/10$.

2.2 Floater bending stiffness

To find the bending stiffness of each torus, cantilever beam theory can be used. By applying a force F_c at the end of the torus section of length L_c, the resulting deflection δ_c can be measured. The bending stiffness can then be calculated from equation (2.2). Cantilever beam theory from [Irgens, 2003, p. 69], the formula of maximum deflection at the end with point force.

$$EI = \frac{F_c L_c^3}{3\delta_c} \tag{2.2}$$

2.3 Linear stiffness relationship of trusses

The relative elongation of the trusses attaching the tori together can be assumed small relative to the force applied. That means a linear load-deflection (F-x) relationship according to equation (2.3) can be used for simplicity. The same theory can be assumed valid for the mooring-lines and the stiffness of the springs used as mooring lines can be found by the same formula.

$$F = kx \tag{2.3}$$

2.4 Overtopping
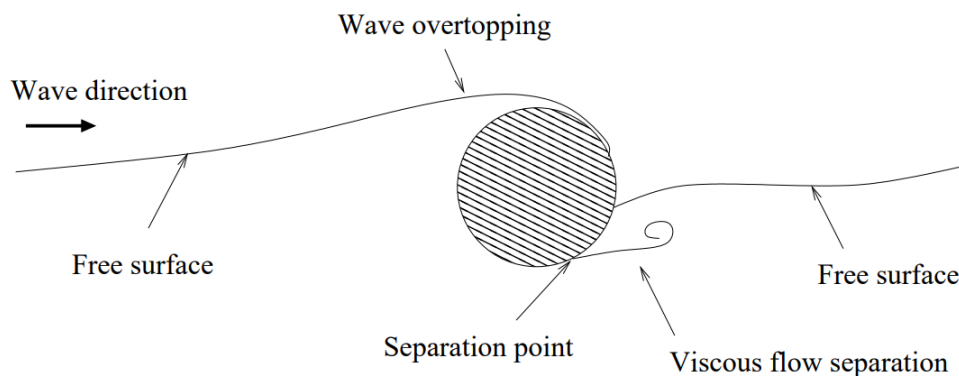
Figure 2.2: Illustration of overtopping on a circular floater in beam sea waves. Courtesy to [Kristiansen, 2010]

The overtopping phenomenon is what happens when seawater flows over the top of the platform's structure, which in this case is characterized as the tori. The phenomenon is

illustrated by [Kristiansen, 2010] in figure 2.2. [Greco, 2001] defines the wave elevation which exceeds the freeboard in two main groups which are referred to as *plunging wave* and *dam breaking* - type water on deck. The first which is described as a wave plunging directly against the eventual structures on top of the freeboard and the other where the mass of water above freeboard flows along the top surface of the structure. A plunging wave will give a greater impact load on the structure than a dam breaking type of overtopping. Her descriptions are related to water on the deck of a ship, but the descriptions are also good to describe the overtopping of a cylindrical torus. Dam breaking type of overtopping is most relevant in this case, as there is no sharp edge, but a circular wall which the water can follow over the top of the structure. Overtopping is a non-linear phenomenon, which can not be described by linear potential flow theory [Kristiansen, 2010].

Overtopping can be a cause of flooding of a structure if a large area is exposed to overtopping or if the water cannot be drained fast enough. If the overtopping event occurs due to a breaking wave which hits the structure either at the side or on top, impact loads from a plunging wave-type of overtopping can cause a local fracture or fatigue damage to the structure. It can also cause slamming loads on the solar panels. Overtopping is the main challenge to the multi-torus design of a floating solar island, as the freeboard is relatively low.

2.5 Elastic body modes

Modal analysis is a method to describe the motion of a model by relating the local response from waves with theoretically known modes described by cosine functions. The elastic response for each mode n is calculated from a sum of cosine functions multiplied by a constant $b_n(t)$ which describes mode n at time t, as presented in equation (2.4).

2.5.1 Modal analysis of vertical modes

The vertical motion of the floater is measured at 16 points symmetrically distributed around the outer tori as described in figure 2.3. Through modal analysis, the sum of the vertical response in M modes is found. $w_m^{exp}(t)$ is the recorded vertical motion at a position β_m on the outer torus. Mode $n = 0$ is heave motion, $n = 1$ is pitch angle, $n = 2$ is the first flexible and so on. A system of equations (2.5) with N unknown constants $b_n(t)$, describing vertical modes is used. The system is solved by transposing and inverting the $\mathbb{A}$ matrix as shown in equation (2.6).

$$w_m^{exp}(t) = \sum_{n=0}^{N} b_n(t) \cos n\beta_m \tag{2.4}$$

$$\begin{bmatrix} w_1^{exp}(t) \\ w_2^{exp}(t) \\ \vdots \\ w_M^{exp}(t) \end{bmatrix} = \begin{bmatrix} 1 & \cos\beta_1 & \cos 2\beta_1 & \cdots & \cos N\beta_1 \\ 1 & \cos\beta_2 & \cos 2\beta_2 & \cdots & \cos N\beta_2 \\ \vdots & \vdots & \vdots & \ddots & \vdots \\ 1 & \cos\beta_M & \cos 2\beta_M & \cdots & \cos N\beta_M \end{bmatrix} \begin{bmatrix} b_0(t) \\ b_1(t) \\ \vdots \\ b_N(t) \end{bmatrix} \tag{2.5}$$
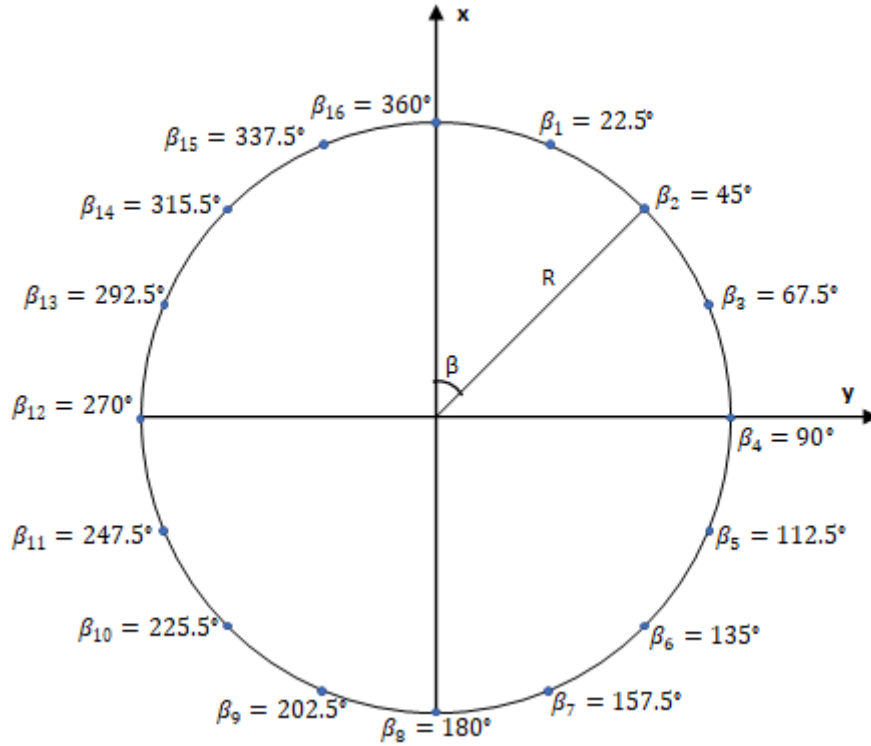
Figure 2.3: Definition of the 16 measurement points where the OQUS globes are positioned at the outer torus to track the motion of the model. The angle β is used to describe the position of the globes around the circular floater with radius R = 0.5m.

$$\mathbb{A}\mathbf{b}(t) = \mathbf{w}(t) \Longleftrightarrow \mathbf{b}(t) = \left[(\mathbb{A}^T \mathbb{A}^{-1}) \mathbb{A}^T \right] \mathbf{w}(t) \tag{2.6}$$

In total, 7 vertical modes are found by using modal superposition. A physical description of 4 out of 7 modes is seen in figure 2.4. The higher modes, which are not described, are a development of the flexible modes.
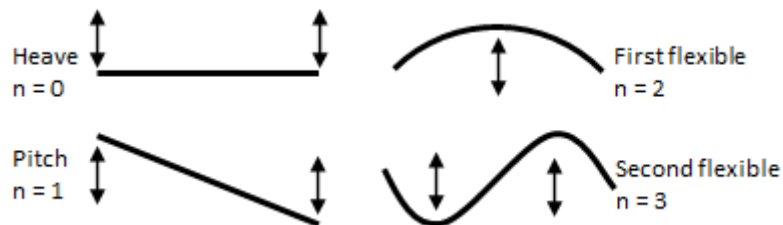
Figure 2.4: Physical description of 4 vertical response modes. Mode $n = 0$ equals to heave motion, $n = 1$ is pitch angle, $n = 2$ is the first flexible, $n = 3$ is the second flexible and so on.

2.5.2 Surge and sway

The horizontal rigid body modes, surge η_1 and sway η_2, are described through the mean value of the x - and y - motions measured at the 16 globes distributed over the outer torus, as shown in equation (2.7) and (2.8). This method is used since the model is circular, which means the horizontal modes cannot be described directly.

$$\eta_1(t) = \frac{1}{M} \sum_{m=1}^{M} x_p(\beta_m, t) \tag{2.7}$$

$$\eta_2(t) = \frac{1}{M} \sum_{m=1}^{M} y_p(\beta_m, t) \tag{2.8}$$

$x_p(\beta_m, t)$ and $y_p(\beta_m, t)$ are the measured motions in the x- and y-direction respectively.

2.5.3 Modal analysis of elastic horizontal modes

The elastic horizontal modes of the circular model are ovalizing modes of which not all are possible to describe physically. The elastic horizontal modes are found using modal analysis of the parameter $v(\beta_m)$, which is defined in equation (2.9). Mode n = 0 is the floater moving radially, which is not physical and therefore has to be excluded from the modal analysis. The mode is not physical since the torus is rigid and to a little extent able to stretch. Also, mode $n = 1$ is surge motion and, therefore, has to be excluded from the modal analysis.

$$v(\beta_m, t) = \sqrt{\tilde{x}_p(\beta_m, t)^2 + \tilde{y}_p(\beta_m, t)^2} \tag{2.9}$$

$$v(\beta_m, t) = \sum_{n=1}^{N} a_n(t) \cos n\beta_m \tag{2.10}$$

The parameters used to describe v, $\tilde{x}_p(\beta_m, t)$ and $\tilde{x}_p(\beta_m, t)$, are defined in equations (2.11) and (2.12).

$$\tilde{x}_p(\beta_m, t) = x_p(\beta_m, t) - \eta_1(t) = v(\beta_m, t) \cos \beta_m \tag{2.11}$$

$$\tilde{y}_p(\beta_m, t) = y_p(\beta_m, t) - \eta_2(t) = v(\beta_m, t) \sin \beta_m \tag{2.12}$$

2.6 Experimental RAO for regular waves

Response amplitude operators (RAO) will be used to describe the response of the model induced from waves. It is describing the relation between the response amplitude and the wave amplitude acting on the model. The RAO curves are affected by the proximity between the natural frequencies and the wave frequency of the interacting wave. The response amplitude a_n is defined using the standard deviation of the modal constants σ_b, found through modal analysis, as described in equation (2.13). The same method is used to find the wave amplitude, using measurements from a wave probe which is positioned in front of the model. From this, the experimental response amplitude operator for mode n is calculated from equation (2.14).

$$a_n = \sqrt{2}\sigma_b, \quad \text{since} \quad \sigma_b = \text{std}(b_n(t)) \tag{2.13}$$

$$\text{RAO}_n^{exp} = \left| \frac{\sigma_b}{\sigma_w} \right| \tag{2.14}$$

2.7 Experimental RAO for irregular waves

As for regular waves, the RAO will be used to describe the response of the model as a function of wave frequencies. As irregular wave series is intended to represent realistic sea states [Steen, 2014], a series of wave frequencies are present during one sea state. This makes it convenient to use spectral analysis of the measured time series to present results from irregular wave tests. Each sea state is represented by a known spectral peak period T_p and significant wave height H_s, commonly calculated by use of a JONSWAP spectrum. As shown by equation (2.15), the response spectrum S_{yy} and the wave spectrum S_{xx} from a sea state is used to find the transfer function $H(\omega)$. This transfer function represents the irregular RAO for the time series measured from the present sea state. RAOs for different modes n can be found using the response time series of mode n calculated from modal analysis.

$$\left| H(\omega) \right|^2 = \frac{S_{yy}(\omega)}{S_{xx}(\omega)} \tag{2.15}$$

2.8 Zero-frequency theory

The zero-frequency theory (ZFT) was developed by [Faltinsen, 2011] for circular collars in fish-farms. It is used in numerical simulations to describe the forces and motions of one torus in this thesis. [Kristiansen, 2012] used this theory in the implementation of the truss model and developed a couple of aspects. Only vertical motions and forces are developed in this section. The theory is based on the following assumptions:

- The body cross-section $2c$ is small compared to the wavelength $\lambda \gg 2c$, which indicates long-wave theory is valid and wave radiation and scattering from the floater is negligible

- Current loads are negligible

- The torus is semi-submerged

- Deep water $\omega^2 = kg$

- Surrounding water has an infinite horizontal extent

- Potential flow theory of incompressible water is valid

- Linear hydrodynamic loads on the floater
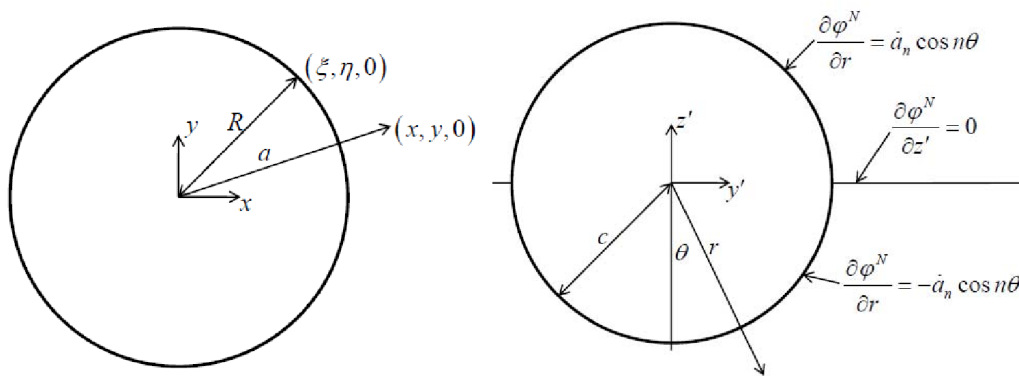
Figure 2.5: Left figure shows the coordinate system seen from the far-field description, where R is the radius of the torus from the circular centre-line and ξ, η describes the position of the source points. The right figure shows the cross-section of a torus in a coordinate system and boundary conditions assumed in the near-field solution. c is the cross-section radius, while ϕ is the velocity potential. Snapshot from [Faltinsen, 2011]

Slender-body theory based on a rigid free-surface condition is developed. This is valid since the limiting case where $\omega \to 0$ is considered. The slender-body theory is based on the assumption that the torus cross-section radius is small compared to the radius of the circular centre-line of the torus $R \gg c$. The coordinate systems and boundary conditions used in the theory are defined in figure 2.5.

A near-field description of the system in question is combined with a far-field description using a matched asymptotic expansion. When the non-convergent series is matched, this determines a constant in the near-field solution that gives a unique solution.

Far-field description

In the far-field description, the torus is defined as a distribution of 3D sources with constant density Q, along the centre-line of the torus. Source points are positioned at $(\xi, \eta, \zeta) = (R\cos\alpha, R\sin\alpha, 0)$. The velocity potential of the far-field description is defined from the definition of 3D sources along a circle, as presented in (2.16). The inner expansion of the

far-field velocity potential ϕ_I^F is determined from the limiting case $r \to 0$. Coordinate systems in figure (2.5) can be used to redefine r, generalizing the expression.

$$\phi^F = \frac{QR}{4\pi} \int_0^\pi \frac{1}{r} d\theta, \quad r \to 0 \quad \Rightarrow \phi_I^F = \frac{Q}{2\pi} \log\left(\frac{8R}{r}\right) \tag{2.16}$$

Near-field description

In the near-field description, a semi-submerged circular cross-section of radius c is assumed. This means a semi-circle is submerged in water and mirroring the semi-circle about the mean free surface ($z = 0$), the rigid free surface condition is satisfied as shown in figure 2.5. The flow is symmetric about the mean free surface and the near-field velocity potential is defined in two dimensions in equation (2.17).

$$\phi^N = \dot{\eta} \left[C \log\left(\frac{r}{R}\right) + A_0(\beta) + \sum_{n=1}^\infty A_n \frac{\cos n\theta}{r^n} \right] \tag{2.17}$$

It is necessary to find the unknown constants C, A_0 and A_n in the expression of the near-field velocity potential. A_0 is found from matching the near-field and the far-field description at the limiting case $\phi^N(r \to \infty) = \phi^F(r \to 0) = \phi_I^F$, which gives $A_0 = -C \log(8)$. C is found from solving the boundary value problem $\frac{\partial \phi^N}{\partial n} = \pm V_n$, which means using the free surface condition at the limiting case $\omega \to 0$. A_n is found from a mathematical trick, by multiplying the velocity potential by $\cos m\theta$ for $m \geq 1$ and integrating the expressions from 0 to 2π.

2.8.1 RAO for heave and pitch of single torus using ZFT

$$RAO_i^{ZFT} = \left| \frac{b_i}{\zeta_a} \right| \tag{2.18}$$

The theoretical vertical RAO for one torus in regular waves of mode 0 (b_0) and 1 (b_1) are defined using ZFT. Mode 0 corresponds to heave motion, while mode 1 corresponds to pitch. Pitch is presented as dimensionless, so it is important to remark that the expression does not correspond to the pitch angle, but a general definition of the pitch mode response. As described by equation (2.18), the response amplitude operator is defined as the absolute value of the measured amplitude motion, divided by the wave amplitude from incident waves. Equations (2.19) and (2.20) are developed from the zero-frequency theory developed above, only taking into account one floater. These equations will be used to compare the theoretical approach to the results of the experiment.

$$\frac{b_0}{\zeta_a} = \frac{(\rho g b_w - \omega^2 a_{33}^{(0)}) J_0(kR)}{-(m + a_{33}^{(0)})\omega^2 + \rho g b_w}, \quad n = 0 \tag{2.19}$$

$$\frac{b_1}{\zeta_a} = \frac{-(\rho g b_w - \omega^2 a_{33}^{(1)})2J_1(kR)}{-(m + a_{33}^{(1)})\omega^2 + \rho g b_w + \frac{EI}{R^4}}, \quad n = 1 \tag{2.20}$$

2.9 Floater model from equation of motion for curved beam

In equation (2.21), the equation of motion for a curved beam is presented. It is based on Newton's 2nd law and the first term on the left side includes a mass per unit length m and a vertical acceleration term $\frac{\partial^2 w}{\partial t^2}$. The second term is accounting for the buoyancy, the third term includes axial stiffness and the fourth term is a stiffness term accounting for the curvature in the beam. On the right hand side of the equation, $f_3 = f_3^{\text{added mass}} + f_3^{\text{exc}} + f_3^{\text{truss}}$ is the sum of vertical forces. $f_3^{\text{added mass}}$ is added mass forces, f_3^{exc} is wave excitation forces and f_3^{truss} is truss forces. The last are representing forces from the modelled trusses in the moorings and the trusses connecting the tori.

$$m\frac{\partial^2 w}{\partial t^2} + \rho g b_w w + EI\frac{\partial^4 w}{\partial s^4} + \frac{EI}{R^2}\frac{\partial^2 w}{\partial s^2} = f_3(s, t) \tag{2.21}$$

A vertical motion decomposition as in equation 2.22, is used to define the vertical motion as a sum of vertical mode components a_n dependent of time t, and the angular position β along the torus radial centre-line.

$$w(t, \beta) = \sum_{n=0}^{\infty} a_n(t)\cos n\beta \tag{2.22}$$

The vertical motion decomposition is inserted into the equation of motion for a curved beam (2.21). Further, both sides of the equation are multiplied with $\cos m\beta$ and β is integrated from 0 to 2π. The last is a mathematical trick, in order to get the result in equation (2.23). After including the last mentions into the equation of motion, this results in the simplified expression in equation (2.24).

$$\int_0^{2\pi} \cos n\beta \cos m\beta d\beta = \begin{cases} \pi, & n = m \\ 0, & n \neq m \end{cases} \tag{2.23}$$

$$m\ddot{a}_n(t) + \rho g b_w a_n(t) + EI\left(\frac{n}{R}\right)^4 a_n(t) - \frac{EI}{R^2}\left(\frac{n}{R}\right)^2 a_n(t) = \frac{1}{\alpha\pi}\int_0^{2\pi} f_3 \cos n\beta d\beta \tag{2.24}$$

Added mass

An expression for the added mass of the torus is found from the near-field solution as described in equation (2.25).

$$a_{33}^{(n)} = -\rho \int_{S_1+S_2} \bar{\phi}^N n_3 ds \tag{2.25}$$

$$= 2\rho c^2 \left\{ \frac{2}{\pi} \left[\log\left(\frac{8R}{c}\right) - K_n \right] + \underbrace{\frac{3 - 4\log(2)}{\pi}}_{=0.07238725793} \right\} \tag{2.26}$$

K_n presented in equation (2.27) is a definite integral defined by Timokha (2010) [Faltinsen, 2011]. The expression first is used in the generalized expression of the inner expansion of the far-field velocity potential.

$$K_n = \frac{1}{2\sqrt{2}} \int_0^{2\pi} \frac{1 - \cos nx}{\sqrt{1 - \cos x}} dx \tag{2.27}$$

As the added mass force per unit length is known as $f_3^{\text{added mass}} = \frac{A_{33}^n}{2\pi R}\ddot{\eta}_3 = a_{33}^n \ddot{a}_n(t)$, the term can be moved to the left hand side, as seen in equation (2.28). Further, expressions for the wave excitation forces and truss forces need to be developed.

$$(m + a_{33}^n)\ddot{a}_n(t) + \left[\rho g b_w + \frac{EI^4}{R}(n^4 - n^2)\right] a_n(t) = \frac{1}{\alpha\pi} \int_0^{2\pi} (f_3^{\text{exc}} + f_3^{\text{truss}}) \cos n\beta d\beta \tag{2.28}$$

Wave excitation forces

$$f_3^{\text{exc}} = f_3^{FK} + f_3^D \tag{2.29}$$

Wave excitation forces f_3^{exc} is a sum of Froude-Kriloff (FK) and diffraction (D) forces, as shown in equation (2.29). Froude-Kriloff loads are caused by hydrodynamic loads on the body, as flow due to ϕ_0 penetrates the body. Diffraction forces are associated with recovering the body impermeability, as the body presence causes a flow. Velocity potential for diffraction is unknown, but the rigid free-surface condition can be applied to the Laplace equation is governing [Greco, 2012]. The loads are defined in equations (2.30) and (2.31), where S_0 is the mean wetted torus surface.

$$\begin{aligned} f_3^{FK} &= \rho \int_{S_0} \frac{\partial \phi_0}{\partial t} n_3 dS \\ &= \Re\left[\rho g \zeta_a i \left\{ J_0(kR) + \sum_{n=1}^{\infty} 2i^n J_n(kR) \cos n\beta \right\} b_w \exp(-i\omega t)\right] \end{aligned} \tag{2.30}$$

$$
\begin{aligned}
f_3^D &= \rho \int_{S_0} \frac{\partial \phi_D}{\partial t} n_3 dS \\
&= \Re \left[-i\omega^2 \zeta_a \left\{ J_0(kR)a_{33}^{(0)} + \sum_{n=1}^{\infty} 2i^n J_n(kR)a_{33}^{(n)} \cos n\beta \right\} \exp(-i\omega t) \right]
\end{aligned} \tag{2.31}
$$

The incident wave velocity potential is shown in equation (2.32) and only the real part of the velocity potential is physical. J_n is the Bessel function of first kind and order n (eq. (2.33)). Order n refers to mode number n. kR is the wave number k multiplied by the radius R of the floater.

$$
\begin{aligned}
\phi_0 &= \Re \left[\frac{g\zeta_a}{\omega} \exp(kz + ikx - i\omega t) \right] \quad \text{where } i = \sqrt{-1}, \\
k &= \frac{\omega^2}{g} \quad \text{and} \quad e^{ikx} = J_0(kR) + \sum_{n=1}^{\infty} 2i^n J_n(kR) \cos n\beta
\end{aligned} \tag{2.32}
$$

$$
J_n(kR) = \frac{1}{\pi} \int_0^{\pi} \cos(n - \tau) - kR \sin \tau d\tau \tag{2.33}
$$

Truss forces

The truss forces are the tensions from the trusses and mooring lines attached to the floater. These are unknown and will be approximated using the truss model. This will be further explained in chapter 3 Numerical Simulations. In equation (2.34), an estimated expression for the truss forces acting on the floater is presented. The expression is developed in [Kristiansen, 2012]. As there is a finite number of attached trusses, the integral can be estimated by a sum of the tensions acting on the floater, dependent on the direction of the tension force. N_H is the number of trusses attached to the floater and β is the angular position corresponding to the position of the truss attachment.

$$
\begin{aligned}
\frac{1}{\alpha_n \pi} \int_0^{2\pi} f_3^{\text{truss}} \cos n\beta d\beta &\simeq \frac{1}{\alpha_n \pi} \sum_{p=1}^{N_H} f_3^{\text{truss},p} \cos n\beta_p \Delta\beta \\
&= \frac{1}{\alpha_n \pi \Delta s} \sum_{p=1}^{N_H} \left[-T_p(\hat{s}_p \hat{k}) \right] \cos n\beta_p \Delta\beta \\
&= \frac{1}{\alpha_n \pi R} \sum_{p=1}^{N_H} \left[-T_p(\hat{s}_p \hat{k}) \right] \cos n\beta_p
\end{aligned} \tag{2.34}
$$

Finally, the expressions for the forces explained above can be included in the equation of motion presented in equation (2.28). This leads to the expression which is written out in equation (2.35).

The system will be further used in the coupling of the floater with the trusses in the numerical simulations.

$$(m + a_{33}^n)\ddot{a}_n(t) + \left[\rho g b_w + \frac{EI^4}{R}(n^4 - n^2)\right]a_n(t) =$$

$$\left[\rho g b_w - \omega^2 a_{33}^{(n)}\right]2\zeta_a J_n(kR)\Re\left[i^{n+1}\exp(-i\omega t)\right] + \frac{1}{\alpha_n \pi R}\sum_{p=1}^{N_H}\left[-T_p(\hat{s}_p\hat{k})\right]\cos n\beta_p \quad (2.35)$$

$$\iff A\ddot{a}_n(t) + Ba_n(t) = F$$

2.10   Truss model by [Marichal, 2003]

The model described in this section was derived by *D. Marichal* in 2003 to be used in a numerical study of a cod-end. It has since then been used in several papers by *Prof. O. Faltinsen & Prof. T. Kristiansen* to model the net panels in aquaculture fish farms as trusses. Prof. T. Kristiansen has suggested this model is used for the mooring lines and elastic trusses between the floaters in the multi-torus. In this section, the model will be derived and explained, as done in [Marichal, 2003].

The model is to be used in a numerical simulation to calculate the unknown internal tensions in the trusses at each time step, using a numerical method. From this, it will be possible to calculate how the displacement of the model changes over time as loads are applied. The model consists of a given number of trusses N_{truss} and a given number of nodes N_{node}. Each truss k is defined by 2 nodes i and j, as seen in figure 2.6. The nodes have coordinates in 3 directions $\{x, y, z\}$. Remark that the enumeration is somehow different in the description below than in the original model by [Marichal, 2003].
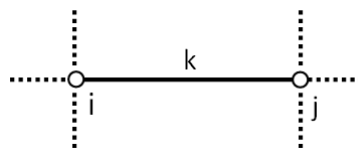

Figure 2.6: Definition of truss element k and corresponding nodes i and j.

Mechanical equations

The fundamental principle of dynamics is applied to each node i, as described by equation (2.36). The mass of the truss is lumped into the nodes, such that each node has the mass m_i. The acceleration of the node a_i is the only unknown parameter in this equation.

$$\sum_{i=1}^{N_{node}} \vec{F}_{i,external} = m_i \vec{a}_i$$

$$= \left\{ m_i \vec{g} + \sum_{l=1}^{N_l} T_{il}^n \hat{s}_{il}^n \right\}$$

(2.36)

The internal tension or linking forces in each truss is considered as external forces which are acting on the node connecting the trusses. N_l is the number of adjacent trusses acting on node i, while T_{il} and $\hat{s}_{il}$ are the axial tensions and corresponding tangential unit vectors acting on node i. The tangential unit vector is defined by equation (2.44). In the standard case, only gravity forces and internal tension are considered as forces in the system. Remark that the sum of the external forces $F_{i,external}$ also can consist of other external loads acting on the nodes or trusses. In a case where loads are distributed on the trusses, these are also lumped into the nodes, such that the sum of the loads are equally distributed between the 2 nodes which form the ends of the truss. If a floater is connected to a truss through a node, the dynamic equation of motion for the floater (2.35) needs to be considered, in order to include relevant forces.

$$l_k^2 = l_{0k}^2 \left(1 + \chi T_k \right)^2$$

(2.37)

The model is based on the truss length constraint described in equation (2.37). The length of a truss is dependent on the initial length and the elasticity properties. Thus, the length of each truss l_k can be defined by the initial length l_{0k}, the elasticity coefficient $\chi = 1/EA$, where E is Young's modulus and A the cross-sectional area of the truss and the tension in each truss T_k. The initial length l_{0k} should be calculated from the truss before pre-tension is applied and can, therefore, be found using the relation in equation (2.38), developed from the truss length constraint and using the pre-tension T_p as tension T_k. Remark that l_{pk} is the pre-tensioned length of the truss and k is the spring stiffness, which is known from the geometry and parameters of the system.

$$l_{0k} = l_{pk} - \frac{T_p}{k}$$

(2.38)

The length constraint will form a system of equations with N_{truss} equations. The system is currently of second order and non-linear. To solve the system, the Euler methods described below will be used. Since the method is a time-step method, the constraint needs to be transferred to be dependent on time, since the tension is time-dependent.

Deriving system of equations

Applying time-dependency to the length constraint in equation (2.37), the definition in equation (2.39) is valid. This states that the length at time step (n+1) is equal to the norm of the distance between the nodal positions of node j and i, $\vec{x}_j^{n+1}$ and $\vec{x}_i^{n+1}$ respectively.

$$l_{0k}^2\left(1 + \chi T_k^{n+1}\right)^2 = \left(\vec{x}_j^{n+1} - \vec{x}_i^{n+1}\right)\left(\vec{x}_j^{n+1} - \vec{x}_i^{n+1}\right) \tag{2.39}$$

Further, the change in tension between two time steps can be defined as $T_k^{n+1} = T_k^n + \Delta T_k$, as seen in equation (2.40). Since it can be assumed that the tension in the trusses is low when an equilibrium position is searched for, the terms which are dependent on change in tension ΔT_k are neglected.

$$
\begin{aligned}
l_{0k}^2\left(1 + \chi T_k^{n+1}\right)^2 &= l_{0k}^2\left(1 + \chi\left[T_k^n + \Delta T_k\right]\right)^2 \\
&= l_{0k}^2\left(1 + 2\chi T_k^n\right)
\end{aligned}
\tag{2.40}
$$

After neglecting the ΔT_k dependent terms, the length constraint can be rewritten as in equation (2.41).

$$l_{0k}^2\left(1 + 2\chi T_k^n\right) = \left(\vec{x_j^{n+1}} - \vec{x_i^{n+1}}\right)\left(\vec{x_j^{n+1}} - \vec{x_i^{n+1}}\right) \tag{2.41}$$

From here, the definition of nodal positions $\vec{x_i^{n+1}}$ from the Euler method can be used (ref. eq. (3.3)), as described by equation (2.42).

$$
\begin{aligned}
l_{0k}^2\left(1 + 2\chi T_k^n\right) &= \left[\Delta t\left(\vec{u}_j^{n+1} - \vec{u}_i^{n+1}\right) + \left(\vec{x}_j^n - \vec{x}_i^n\right)\right]\left[\Delta t\left(\vec{u}_j^{n+1} - \vec{u}_i^{n+1}\right) + \left(\vec{x}_j^n - \vec{x}_i^n\right)\right] \\
&= \left(\vec{x}_j^n - \vec{x}_i^n\right)\left(\vec{x}_j^n - \vec{x}_i^n\right) + 2\Delta t\left(\vec{u}_j^{n+1} - \vec{u}_i^{n+1}\right)\left(\vec{x}_j^n - \vec{x}_i^n\right)
\end{aligned}
\tag{2.42}
$$

In equation (2.42), the second order terms $(\Delta t)^2$ are neglected since $\Delta t \ll 1$. This is an approximation made to simplify the system of equations. From this, the definition of velocity at the next time step (n+1) from the acceleration in time step n in the Euler method (ref. eq. (3.3)) is used. The acceleration a_i is then expressed from the fundamental principle of dynamics (ref. eq. (2.36)).

$$
\begin{aligned}
\vec{u}_i^{n+1} &= \vec{u}_i^n + \Delta t \vec{a}_i^n \\
&= \vec{u}_i^n + \frac{2\Delta t}{m_i}\left\{m_i\vec{g} + \sum_{l=1}^{N_l} T_{il}^n \hat{s}_{il}^n\right\}
\end{aligned}
\tag{2.43}
$$

Equation (2.43) can be applied to node i and j, which is end 1 and 2 of the corresponding truss k, as shown in equation (2.45). When summing up the contribution of the forces, the direction of the tension force needs to be taken into account. This is assured by the tangential unit vector $\hat{s}_k^n$ of each truss k, defined in equation (2.44).

$$\hat{s}_k^n = \frac{\left(\vec{x}_j^n - \vec{x}_i^n\right)}{\left|\left(\vec{x}_j^n - \vec{x}_i^n\right)\right|} \tag{2.44}$$

$$
\begin{aligned}
\vec{u}_i^{n+1} &= \vec{u}_i^n + \frac{2\Delta t}{m_i}\left\{m_i \vec{g} + \sum_{l=1}^{N_l} T_{il}^n \hat{s}_{il}^n\right\} \\
\vec{u}_j^{n+1} &= \vec{u}_j^n + \frac{2\Delta t}{m_j}\left\{m_j \vec{g} + \sum_{l=1}^{N_l} T_{jl}^n \hat{s}_{jl}^n\right\}
\end{aligned}
\tag{2.45}
$$

Then, by reorganizing equation (2.42), and inserting the expressions for the velocity $\vec{u}_i^{n+1}$ and $\vec{u}_j^{n+1}$ in node i and j respectively, all terms in the system of equations can be expressed at the same time step n. This is shown by equation (2.46).

$$
\left(\vec{u}_j^{n+1} - \vec{u}_i^{n+1}\right)\left(\vec{x}_j^n - \vec{x}_i^n\right) = \frac{1}{2\Delta t}l_{0k}^2\left(1 + 2\chi T_k^n\right) - \frac{1}{2\Delta t}\left(\vec{x}_j^n - \vec{x}_i^n\right)\left(\vec{x}_j^n - \vec{x}_i^n\right) \Leftrightarrow
$$
$$
\left[\vec{u}_j^n + \frac{2\Delta t}{m_j}\left\{m_j \vec{g} + \sum_{l=1}^{N_l} T_{jl}^n \hat{s}_{jl}^n\right\} - \vec{u}_i^n - \frac{2\Delta t}{m_i}\left\{m_i \vec{g} + \sum_{l=1}^{N_l} T_{il}^n \hat{s}_{il}^n\right\}\right]\left(\vec{x_j^{n+1}} - \vec{x_i^{n+1}}\right) \tag{2.46}
$$
$$
= \frac{1}{2\Delta t}l_{0k}^2\left(1 + 2\chi T_k^n\right) - \frac{1}{2\Delta t}\left(\vec{x_j^n} - \vec{x_i^n}\right)\left(\vec{x_j^n} - \vec{x_i^n}\right)
$$

Finally, equation (2.46) is reorganized with the tension-dependent terms on the left-hand side, and the others on the right-hand side of the equation. Thus, for a given system consisting of N_{truss} trusses, a linear system of equations $\mathbf{A}T = b$ can be defined from N_{truss} equations on the form described in equation (2.47). The system can be solved for T at each time step n, since the tensions are the only unknown parameters of the system at time step n.

$$
\left[\frac{2\Delta t}{m_j}\sum_{l=1}^{N_l} T_{jl}^n \hat{s}_{jl}^n - \frac{2\Delta t}{m_i}\sum_{l=1}^{N_l} T_{il}^n \hat{s}_{il}^n\right]\left(\vec{x_j^n} - \vec{x_i^n}\right) - \frac{l_{0k}^2}{\Delta t}\chi T_k^n
$$
$$
= \frac{l_{0k}^2}{2\Delta t} - \left\{\frac{1}{2\Delta t}\left(\vec{x_j^n} - \vec{x_i^n}\right) + \left(\vec{u_j^n} - \vec{u_i^n}\right)\right\}\left(\vec{x_j^n} - \vec{x_i^n}\right)
$$
$$
\tag{2.47}
$$

2.11   Coupling zero-frequency floater model with truss model

In order to develop a numerical model that can be compared to the multi-torus, the first step is to couple the truss model to a floater model. The zero-frequency theory and dynamic equation of motion described in section 2.9 are used for the floater. The floater equation (2.35) includes terms with unknown tension forces. The truss model by [Marichal, 2003] described in section 2.10 is used to model the trusses in the system. Trusses are used to describe mooring lines and elastic links connecting the tori together. In the system, trusses of which at least one of the node ends are located on a floater will be referred to as floater trusses. For standard trusses, the ones that are not connected to a floater node, the truss equation (2.47) will remain unchanged when implementing the floater. These will only change dependent on the boundary conditions. The floater truss equation is adapted using the expression of the nodal acceleration expressed by the dynamic equation of motion (2.35), developed for the floater model. When the nodal acceleration of the floater node j is inserted into the truss equation (2.47), it results in equation (2.48). Here, N_H is the number of trusses attached to the corresponding floater.

$$
\left[-\Delta t \sum_{p=1}^{N_H} h_{jp} T_p \hat{s}_p - \frac{2\Delta t}{m_i} \sum_{l=1}^{N_l} T_{il}^n \hat{s}_{il}^n \right] \left(\vec{x_j^n} - \vec{x_i^n} \right) - \frac{l_{0k}^2}{\Delta t} \chi T_k^n = \frac{l_{0k}^2}{2\Delta t}
$$

$$
- \left\{ \frac{1}{2\Delta t} \left(\vec{x_j^n} - \vec{x_i^n} \right) + \left(\vec{u_j^n} - \vec{u_i^n} \right) + \Delta t \sum_{n=0}^{\infty} \left\{ \frac{1}{m + a_{33}^n} \left[f_3^{exc} - C_{3n} a_n \right] \cos n\beta_j \right\} \right.
$$

$$
\left. -2\Delta t \vec{g} \right\} \left(\vec{x_j^n} - \vec{x_i^n} \right) \quad \text{where} \quad h_{jp} = \sum_{n=0}^{\infty} \frac{cos n\theta_p \cos n\beta_j}{(m + a_{33}^n)\alpha \pi R}
$$

$$
C_{3n} = \rho g b_w + \frac{EI^4}{R} (n^4 - n^2)
$$

(2.48)

Chapter 3

Numerical Methods and Implementation

In this chapter, the numerical implementation of the model in Python will be described. The goal is to couple the ZFT floater model with the truss model describing the mooring lines and trusses, connecting the floaters together. The truss model described in section 2.10 and the floater model presented in section 2.9 will be implemented to describe the components of the model. As the multi-torus has a quite complicated geometry, as a first step it is chosen to model only the outer torus together with the mooring lines. In a later step, another torus could be connected to the outer torus with trusses and further developing the model.

3.1 Python

The object-oriented programming language Python is used in the numerical implementation of the model. A Scientific Development Environment named Spyder, in the Anaconda package, is used working with Python. It is an open-source programming language, with thousands of available built-in modules and libraries. This makes it flexible and easy to use, which is why it is chosen for this project.

3.2 Implicit-Explicit Euler method

An Implicit-Explicit Euler method is used as a time integration scheme. It is a time step method which can be used to solve an ordinary differential equation (ODE). The method can be derived from a time difference scheme when assuming an initial condition to the problem. The initial condition is stated as $y(t_0) = y_0$, with the initial value problem $\dot{y}(t) = f(t, y(t))$ here, to derive the method by use of finite differences. The method described here is derived in its complete form in [Atkinson, 1978].

Using a finite difference scheme on the form of equation (3.1), by definition the derivative of y is approximated to be equal to the finite difference when $\Delta t > 0$ & $\Delta t \ll 1$.

$$\dot{y}(t) = \lim_{\Delta t \to 0} \left[\frac{y(t + \Delta t) - y(t)}{\Delta t} \right] \approx \frac{y(t + \Delta t) - y(t)}{\Delta t} \tag{3.1}$$

That means $y(t + \Delta t)$, which is the next value of the next time step $(n + 1)$ can be found from reorganizing the finite difference equation as done in equation (3.2), using the initial value problem.

$$y(t + \Delta t) = y(t) + \Delta t f(t, y(t)) = y(t) + \Delta t \dot{y}(t) \tag{3.2}$$

From this, the velocity of the next time step can be solved for explicitly using the acceleration in the given time step, as done in equation (3.3). An Implicit scheme is then used to solve for the nodal positions, as done in the second line of equation (3.3). Since the velocity of the next time step is defined explicitly, this can be used to define the nodal positions of the next time step explicitly as well. This is valid since the derivative of the acceleration is defined by velocity, and the derivative of the velocity is defined by a position. Thus, a double finite difference scheme is used, by redefining the initial value problems $\ddot{\vec{x}} = \vec{a}$, $\vec{u} = \dot{\vec{x}}$ to $\dot{\vec{u}} = \vec{a}$, $\dot{\vec{x}} = \vec{u}$.

$$
\begin{aligned}
\vec{u}_i^{n+1} &= \vec{u}_i^n + \Delta t \vec{a}_i^n \\
\vec{x}_i^{n+1} &= \vec{x}_i^n + \Delta t \vec{u}_i^{n+1} \\
&= \vec{x}_i^n + \Delta t \left(\vec{u}_i^n + \Delta t \vec{a}_i^n \right)
\end{aligned} \tag{3.3}
$$

3.3 Runge-Kutta 4$^{\text{th}}$ order method

Runge-Kutta 4$^{\text{th}}$ order (RK4) is an explicit numerical method to approach the solution of ordinary differential equations (ODE). There exist several Runge-Kutta methods of different orders, but RK4 is the most well-known since it is easy to implement and gives good approximations. The reason it gives good results is that a total of four estimates of the next time step are included in the approximation [Vistnes, 2018].

$$A \ddot{a}_n(t) + B a_n(t) = F \iff \frac{d^2 a}{dt^2} = \frac{-B}{A} a + \frac{F}{A} \tag{3.4}$$

A second order ODE is defined in equation (3.4), describing the equation of motion developed from zero-frequency theory. The constants A, B and F are defined in equation (2.35). To be able to use RK4, it is necessary to transform the second order ODE into two linear ODE. This is done by introducing a variable y, as shown in equation (3.5).

$$
\begin{aligned}
\frac{da}{dt} &= y \\
\frac{dy}{dt} &= \frac{d^2 a}{dt^2} \iff \frac{dy}{dt} = \frac{-B}{A} a + \frac{F}{A} = C_1 a + C_2
\end{aligned} \tag{3.5}
$$

When introducing a new variable, it is possible to describe the second order ODE as a system of two linear ODE, which is introduced on matrix form in equation (3.6).

$$\begin{bmatrix} \dot{a} \\ \dot{y} \end{bmatrix} = \begin{bmatrix} 0 & 1 \\ C_1 & 0 \end{bmatrix} \begin{bmatrix} a \\ y \end{bmatrix} \begin{bmatrix} 0 \\ C_2 \end{bmatrix} \tag{3.6}$$

$$\begin{aligned} \frac{da}{dt} &= f(a, y, t) \\ \frac{dy}{dt} &= g(a, y, t) \end{aligned} \tag{3.7}$$

In order to use RK4, the two unknowns are defined as functions (ref. eq. (3.7)), dependent on known parameters at time step n. The functions' values at the next time step $(n+1)$ can then be approximated by the RK4. Since the ODE had to be split into a two-equation system, the RK4 has to be applied for both equations, coupling the weighted slopes as explained by equation 3.8. That means the present value of the function is used to approximate the next value, which also means the method is explicit. As mentioned earlier, four weighted slopes are used to determine the next value. The contribution of the four slopes is averaged and added to the present value. k_1 and l_1 are approximated by the slope at the present value like in standard Explicit Euler method. k_2 and l_2 are based on the midpoint of the increment $(dt/2)$ using k_1, l_1, whereas k_3 and l_3 are also based on the midpoint of the time step using k_2, l_2. k_4 and l_4 are found from the slope at the next step using dt and k_3, l_3. The two midpoint values contribute two times to the average, and the complete sum of the weighted slopes is divided by 6 and multiplied with the time step dt.

$$\begin{aligned} t_{n+1} &= t_n + dt \\ a_{n+1} &= a_n + \frac{dt}{6}(k_1 + 2k_2 + 2k_3 + k_4) \\ y_{n+1} &= y_n + \frac{dt}{6}(l_1 + 2l_2 + 2l_3 + l_4) \\ \text{where} \quad k_1 &= f(a_n, y_n, t_n) \\ l_1 &= g(a_n, y_n, t_n) \\ k_2 &= f(a_n + \frac{k_1}{2}, y_n + \frac{l_1}{2}, t_n + \frac{dt}{2}) \\ l_2 &= g(a_n + \frac{k_1}{2}, y_n + \frac{l_1}{2}, t_n + \frac{dt}{2}) \\ k_3 &= f(a_n + \frac{k_2}{2}, y_n + \frac{l_2}{2}, t_n + \frac{dt}{2}) \\ l_3 &= g(a_n + \frac{k_2}{2}, y_n + \frac{l_2}{2}, t_n + \frac{dt}{2}) \\ k_4 &= f(a_n + k_3, y_n + l_3, t_n + dt) \\ l_4 &= g(a_n + k_3, y_n + l_3, t_n + dt) \end{aligned} \tag{3.8}$$

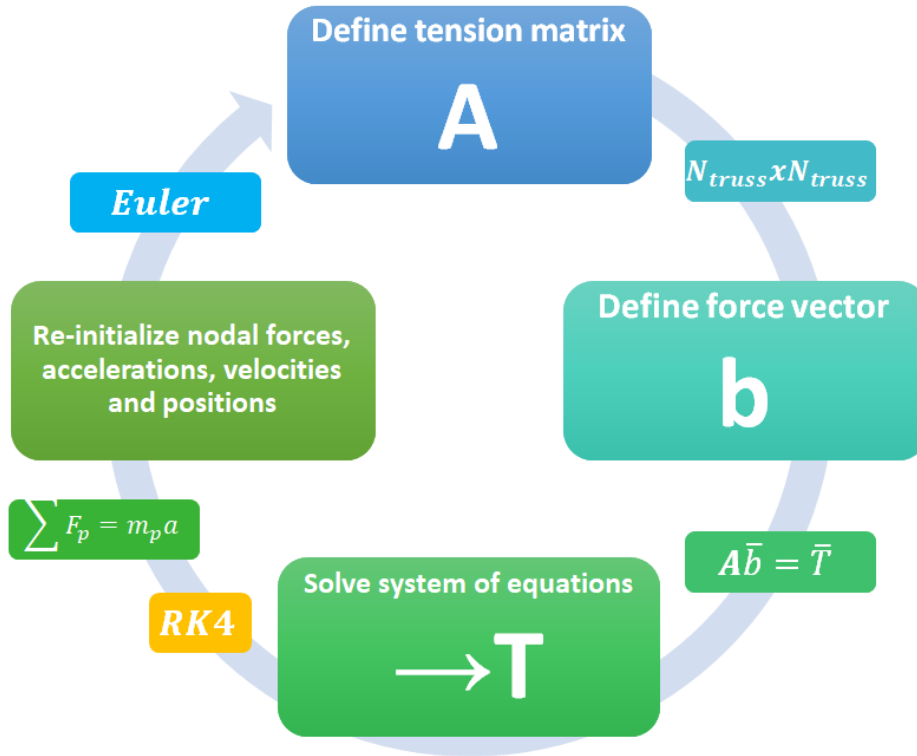## 3.4 Numerical implementation of truss model

Figure 3.1: Illustration of the time-stepping loop implemented in the numerical simulation model in Python. Each step is based on creating the matrix $\mathbf{A}$, which defines the dependencies of the nodes and trusses with the tension force, and the force vector b in order to solve the linear equation system for the tensions T. Then the nodal forces, accelerations, velocities and positions are re-initialized, before the next time step starts. Pay attention to that the RH4 solver will only be necessary when the model is coupled with the floater.

Implementation of the truss model in Python is mainly done by use of a time-stepping loop, solving the linear system of equations $\mathbf{A}T = b$ where T are the unknown tensions. Equation (2.47) in section 2.10 is the basis for each line in the system of equations, where the tension dependent terms are positioned at the left-hand side in matrix form. The system is solved for each time step, using an Implicit-Explicit Euler time difference scheme (see section 3.2) to define the necessary unknown parameters of the next time step. The loop calculates time-dependent parameters and solves the equation system numerically. In figure 3.1, the loop is illustrated. Pay attention to that the RH4 solver will only be necessary when the model is coupled with the floater.

The time-stepping process consists of defining the $\mathbf{A}$ matrix, the b-vector, solving the system of equations and then re-calculating the time-dependent parameters before the next time step starts. The left-hand side of the system in equation (2.47) is dependent of the tensions T_k and
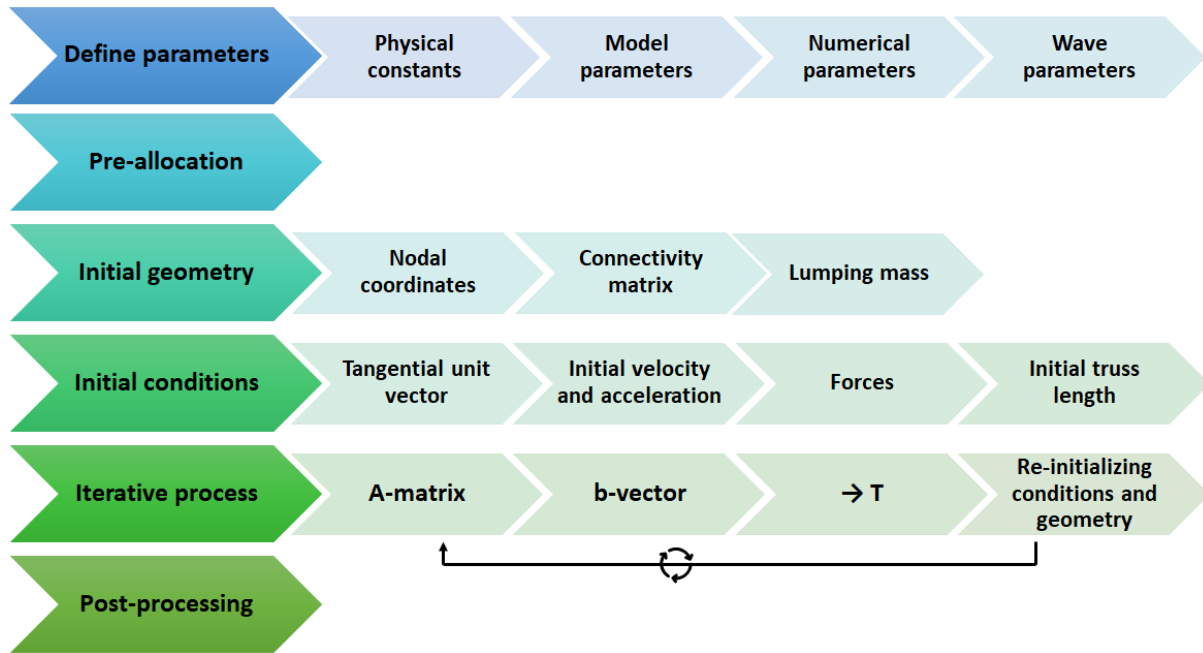
Figure 3.2: Numerical implementation of the truss model in Python requires the following steps. The truss model itself is built into the time integration process, which repeats with increasing time step n. $\mathbf{A}$ is a matrix made from the left-hand side of the truss model equation, whereas the b-vector is the force-dependent expressions on the right-hand side of the equation. T are the tensions which are found from solving the linear equation system $\mathbf{A}T = b$. Wave parameters are only needed when coupling the model with the floater.

is therefore assigned in $\mathbf{A}$, whereas the right-hand side of the same equation is defined in the force vector b. The matrix $\mathbf{A}$ is saved as a sparse in coordinate format to save computational time since a large number of the entries are equal to zero. The system of equations is solved by use of a built-in library in Python named *scipy* and the function *scipy.sparse.linalg.spsolve* which solves sparse linear systems on the form $\mathbf{A}T = b$ with $\mathbf{A}$ and b as input.

The complete implementation model is illustrated in figure 3.2. A pre-definition of parameters, initial conditions and geometry definitions of the model are necessary prior to the time loop. In this step, all variables are also pre-allocated, to save computational time. For-loops are used to define the geometry of the system depending on the shape and the number of trusses, which are changeable in the model parameters. Using the geometry, initial length and tangential unit vectors of the system are defined. A connectivity matrix of two columns and N_{truss} number of rows is also defined, where the node number of the end 1 and 2 of truss number k is placed on the corresponding row and column. Initial conditions for velocity is set, and boundary conditions are applied by setting the velocity of the fixed nodes to zero, which means the corresponding nodal positions will be kept constant.

The Implicit-Explicit Euler method is further used to find the corresponding velocity and nodal positions at time step $(n + 1)$ (ref. eq. 3.3). From this, the new tangential unit vector for each truss is calculated by use of the new nodal positions (ref. eq. 2.44). The tangential unit vectors are defined positive from node 1 (i) of the truss, and the change in $\hat{s}$-direction for node 2 (j) needs to be taken into account when calculating the weights of the **A**-matrix and the b-vector.

Theoretically, trusses can take compression, but in a physical model without bending stiffness, the trusses will act as chords which have slack when forces are less than zero. Even though, due to the theory, it has been considered that it is most conform to keep the eventual compression forces after discussion with Prof. J. Kiendl. As the tensions are solved for at time step n, the Newton's 2nd law (ref. eq. 2.36) is solved for the acceleration at time n. The fixed node(s) are not solved for, instead, the sum of forces is set to zero to keep the acceleration and velocity vectors equal to zero, such that the nodal position of the fixed node(s) is kept constant. This is a method for applying the necessary boundary conditions. That means the eventual mass in the fixed node is ignored. Masses in fixed nodes are therefore only used for numerical reasons.

The nodal positions, mass distribution, initial and boundary conditions are according to the desired physical model to be implemented. This is the only changes necessary in the implementation when changing model.

3.5 Verification studies of truss model

Four different verification studies are carried out during the implementation of the truss model. These include a suspended flexible wire, a simple rigid pendulum, a double rigid pendulum and a compound flexible pendulum. Elasticity is also applied and tested on all rigid pendulum models. Note that only 2D cases have been studied. This is not the case in the extended coupled model, but it is not expected to cause a problem, as everything is implemented in 3D, just setting the y-coordinates to zero. The physical properties used to define flexibility in the trusses are defined in table 3.1. The same physical parameters are used in all verification studies, but for the simple and double pendulum, the trusses are modelled as massless. This is simple to obtain as a lumped mass principle is used in the model. That means the cross-sectional area is not used to calculate the mass of the truss, as the truss is expected to be massless.

In the case testing, both the numbers of trusses and time step length is tested for convergence. Since the pendulum studies are well documented in theory, their expected behaviour will be compared with the numerical results. The physical properties used to define flexibility in the trusses during verification studies are defined in table 3.1. The same physical parameters are used in all cases, but for the simple and double pendulum, the trusses are modelled as massless. This is simple to obtain as a lumped mass principle is used in the model. The compound flexible pendulum is compared with a numerical solution by [Marino et al., 2019], using beam elements. It is expected that the pendulum will act more like a chord and bend more by use of the truss model, as truss elements without bending stiffness are used.

Table 3.1: Physical properties used for flexible pendulums. Note that if the pendulums are considered to be massless, the cross-sectional area and material density are not used.

Physical variable	Parameter	Unit	Value
Truss diameter	d_{truss}	$[m]$	0.01
Material density	ρ	$[kg/m^3]$	1100
Young's modulus	E	$[Pa]$	$5\cdot10^6$
Total length	L	$[m]$	1

Considering the pre-tensioned wire, it is modelled by five truss elements with equal length and mass is uniformly distributed over the wire. As the model includes a pre-tension, it is expected that the wire will vibrate around its initial position and no stable equilibrium will be obtained since only gravity is the only external force applied. Gravity will at all times work to equalize the internal tensions. In Appendix D.1.1, an example where the system of equations is written out can be found. As the wire is modelled by five truss elements, the system of equations will contain five equations with five unknown tensions at each time step.

$$T_0 = 2\pi\sqrt{\frac{L}{g}}\Big(1 + \frac{\theta_0^2}{16} + \frac{11}{3072}\theta_0^4 + ...\Big) \tag{3.9}$$

For the implementation of the pendulums, point masses of $1\ kg$ have been positioned in the nodes. Three initial position angles have been tested for each case: 45°, 90° and 135°. As goes for the simple rigid pendulum, it is expected to move symmetrically around the vertical axis with the initial position angle as the maximum angle of deflection. The oscillation period can be estimated by the power series in equation (3.9), which is developed by the ODE of the simple pendulum. Expected oscillation periods dependent on the initial position can be found in table 3.2. This will be compared to the numerical solutions using the truss model. As elasticity is applied to the truss, tension forces will cancel the oscillatory movement and create non-symmetric oscillations. The truss will now act like a combination of a rigid oscillatory system and a spring-mass system vibrating in the axial direction.

The double pendulum will be tested both with rigid trusses, flexible trusses and compound mass

Table 3.2: Approximate oscillation periods for rigid simple pendulums estimated by power series developed from ODE. Only the terms of order less than 5 are included. (Ref eq. (3.9)).

Initial position θ_0 [°]	Oscillation period T_0 [s]
45	2.0861
90	2.3592
135	2.9235

distribution with flexible trusses. The first truss including the first point mass will initially be expected to oscillate like the simple rigid pendulum, but as the second mass starts influencing the system, a more unsymmetric and chaotic behaviour is expected. The amount of chaos will depend on the distribution of mass between the first and second point mass, as well as the initial position. In all tests, each of the two point masses is kept at an equal initial position angle. Including flexibility, the behaviour will be even more unpredictable as spring vibrations of the trusses needs to be included. The rigid pendulum will be compared to a numerical analysis using the fourth order Adams-Bashforth method [Calvão and Penna, 2015]. As the double compound pendulum is tested, the rotative behaviour of the second point mass around the first point mass is expected to increase, as the second point mass is half the first in weight. This is true since smaller forces are needed to induce rotation of the smaller mass. However, when the mass is lower, the velocity induced by gravity forces are also smaller.

At last, a compound flexible pendulum is modelled in two different configurations. One with four trusses, and the other one with 20 trusses. The important difference from the other pendulum models is that the cross-sectional area and density of the truss material is used to calculate the mass of the trusses. This is done in order to assure a realistic relationship between mass and stiffness. Figure 3.3 shows a numerical solution by [Marino et al., 2019], using beam elements. It shows the position of the pendulum at given time steps from 0 - 1 s and the vertical tip displacement during the first second. The resulting displacement and deformation have been compared to other relevant studies and results show good correspondence to the related articles using both implicit and explicit numerical methods. The results are therefore used for comparison with the truss model. The mass and flexibility properties in the two cases are equal. As truss elements without bending stiffness are used in here, an expected difference between the two models is that the truss model will bend more in the tip and the angle will change more brutally between the elements. Yet more elements are used in the model by
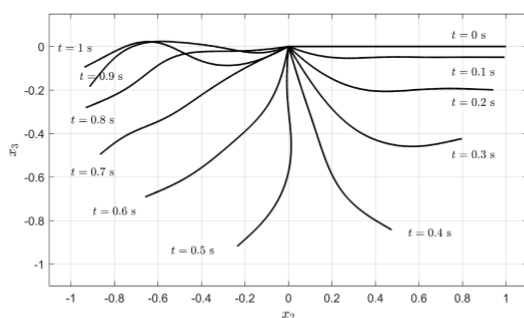

Fig. 6. Snapshots of a swinging flexible pendulum from time 0 to 1 s with increments of 0.1 s. $p = 4$, n = 30, $h = 1 \times 10^{-5}$ s.
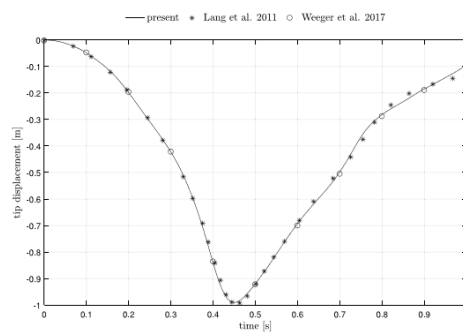
Fig. 7. Vertical tip displacement of a swinging flexible pendulum: comparison of the present case for $p = 4$, n = 30, $h = 1 \times 10^{-5}$ s (solid line) with Lang et al. [39] (∗) and Weeger et al. [28] (o).

(a) Position of the pendulum at given time steps with initial position 90°

(b) Vertical tip displacement of pendulum during first second of motion

Figure 3.3: Comparison of vertical tip displacement of a swinging flexible pendulum from [Marino et al., 2019]. The elements are modelled by beams with bending stiffness.

[Marino et al., 2019], than in the truss model also, which makes the movement of the beam model much more realistic.

In Appendix D.1, more details on the different verification studies can be found. Both numerical properties, physical parameters and examples of expected behaviour can be found there.

3.6 Numerical implementation of coupled floater-truss model

In order to develop the numerical simulation script into a model that can be compared to the multi-torus, the first step is to implement the floater model and couple it with the truss model already implemented. The zero-frequency theory and dynamic equation of motion described in section 2.9 are used to implement the floater equation. Trusses are used to describe mooring lines and elastic links connecting the tori together. Since the floater equation is also time-dependent, it will be added to the time integration loop. As there will be trusses connected to the floater, the truss equation (2.47) has to be adapted for the so-called floater trusses. An adapted equation is developed in section 2.11.

As seen in the adapted floater-truss equation (2.48), the right-hand side of the equation includes the unknown vertical displacement for mode n, $a_n(t)$. This can be found by solving the floater equation at each time step. Remark that n is mode number, since the vertical motion is described by $w(t, \beta) = \sum_{n=0}^{\infty} a_n(t) \cos n\beta$. The Runge-Kutta 4th order method described in section 3.3 is used as solver. In a numerical solver, the infinite sum needs to be limited to a finite number. $N = 10$ has been chosen as sufficiently accurate in this case.

Initial geometry from the pre-tensioned wire in the verification study is adapted for a circular model. Wave parameters are implemented by use of an implicit function iterating the solution to find the correct wave number k, according to the desired wave period. The connectivity matrix, mass lumping and tangential unit vector rest unchanged. Initial conditions for velocity and acceleration are set to zero. The added mass, mooring forces and wave excitation forces are initialized, a first calculation the dynamic equation of motion and a modal sum to find the vertical motion are resolved before the time step loop starts.

Figure 3.4 is an example of how a combined floater and truss model can be discretized with nodes positioned on the floater. As more than one torus is implemented, it will be necessary to separate the different types of floater trusses, depending on whether there is a floater connected in both ends or not.

3.7 Single torus attached by four mooring lines

A first step towards simulating the behaviour of the multi-torus is to test the coupled floater and truss model with one torus and attached mooring lines modelled by trusses. The scale is equal to the multi-torus tested in the experiment. That means the radius of the torus is $R = 0.5$ m and four mooring lines are symmetrically attached at 45°, 135°, 270°and 315°, fixed at ± 1.25

m from the centre of the torus in both x- and y-direction. The model is discretized in figure 3.4. Truss discretization is shown in table 3.3. Remark that the floater model is only implemented in the vertical direction, but the nodal coordinates and necessary variables are updated in 3D for each time step. That means only vertical forces are applied to the system, but the system is allowed to move in all directions.

When developing the Python script, it has been assured that the number of trusses easily can be changed, as long as the number of trusses discretizing each mooring line is kept equal. For simplicity, the model presented here is made with only 12 trusses, which is the least number possible assuring that all cases of truss combinations are included. This means at least one floater truss, one standard truss and one truss affected by boundary conditions is present in the system. Each mooring line has therefore been divided into three trusses. As the number of trusses is increased, only the number of standard trusses will be increasing as long as the model
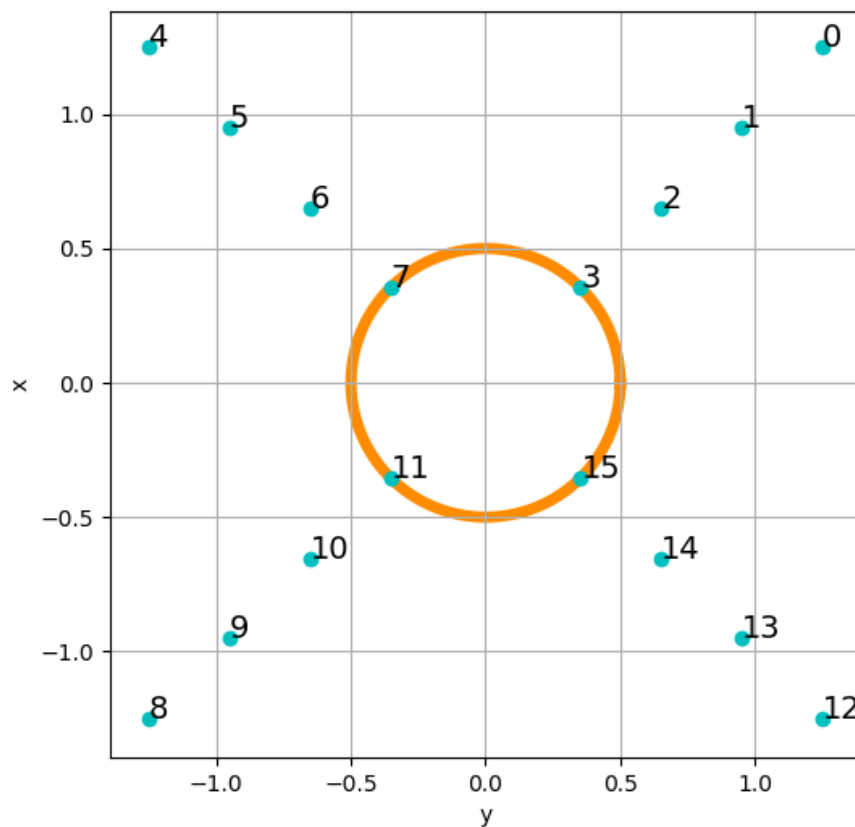

Figure 3.4: Defining truss and node numbers of 12 truss model with connected with floater. Each mooring line is divided into 3 trusses, one which is fixed at end 1, one standard truss and one truss with end 2 connected to the floater. That means all three possible cases for trusses are included in the modelling.

is kept the same. An example of the development of the equation system $\mathbf{A}b = T$ from the combined truss and floater model for 12 trusses is carried out in Appendix D.2.

3.8 Two tori connected with trusses

As the multi-torus consists of five connected tori, it is complicated to predict its behaviour. It is likely to believe that the tori are positioned close enough to change the predicted movement of a single torus exposed to waves. Especially since they are connected by pre-tensioned links. This is why it is interesting to develop a numerical model with two or more connected tori and mooring line attachments. As the number of tori increases, the complexity of the geometry and numerical implementation augments. A model with two tori connected together at 8 symmetrical positions and four mooring lines attached equally as in the previous case will be presented. The connecting links between the tori will be modelled by trusses. As a first step, each connecting link is modelled by one truss, but with the possibility to increase the number of trusses discretizing this. The discretized model is presented in figure 3.5, with the corresponding connectivity matrix in table 3.4. A new truss case has been developed, as the linking trusses will have floater nodes at both ends. The scale of the model is still kept the same as the two outer tori in the model tests of the multi-torus.

3.9 Limitations of the model

The most limiting feature of the model is that the dynamic equation of motion for the floater only is implemented in the vertical direction. Sway (y) is assumed to be negligible [Kristiansen, 2012]. There exist terms for the forces in surge developed in [Kristiansen, 2012] which are possible to implement, but these have not been a priority due to the limited amount of time available for the project. Limitations of the used theoretical methods also have to be kept in mind. Zero-frequency theory assumes that current loads are negligible, the long-wave theory is valid, the wave radiation from the floater is negligible, the deep water dispersion relation is valid, surrounding water has infinite horizontal extent potential theory and linear hydrodynamic loads.

Truss number	0	1	2	3	4	5	6	7	8	9	10	11
Node end 1	0	1	2	4	5	6	8	9	10	12	13	14
Node end 2	1	2	3	5	6	7	9	10	11	13	14	15

Table 3.3: Connectivity matrix of the discretized model in figure 3.4 showing which nodes corresponds to end 1 and 2 of the truss in between. Since the floater is included, the connectivity matrix will no longer be banded.
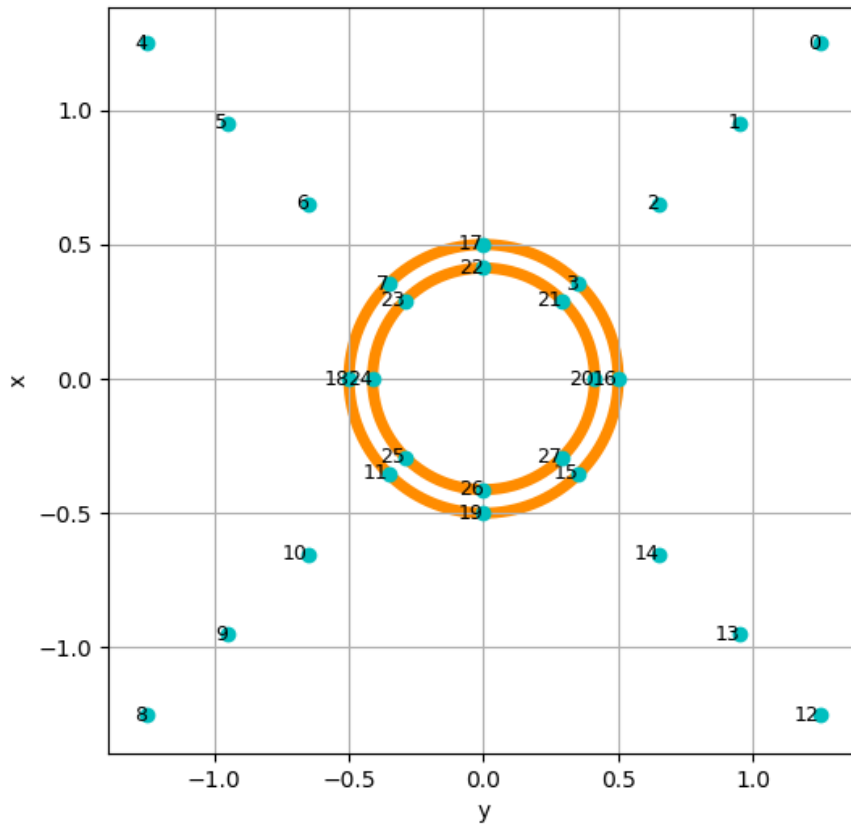
Figure 3.5: Discretization of the two-tori connected through trusses. The computational solution time of the linear system of equations will be quite dependent of the bandedness of the matrix.

Truss number	0	1	2	3	4	5	6	7	8	9
Node end 1	0	1	2	3	17	4	5	6	7	18
Node end 2	1	2	3	21	22	5	6	7	23	24
Truss number	10	11	12	13	14	15	16	17	18	19
Node end 1	8	9	10	11	19	12	13	14	15	16
Node end 2	9	10	11	25	26	13	14	15	27	20

Table 3.4: Connectivity matrix of the discretized model in figure 3.5 showing which nodes corresponds to end 1 and 2 of the truss in between. The discretization of the model will be important concerning the computational solution time of the linear equation system, therefore the truss numbers are sorted in a way that will keep as much of the non-zero entries as possible close to the diagonal of the matrix.

Chapter 4

Model Tests

In this chapter, the preparation, execution and post-processing of the model tests conducted in Lilletanken during February will be described. The original multi-torus model was made by Jonathan Windsvold during his master's thesis in 2018, but the model has been modified and rebuilt. During the work with the project thesis, a visualization experiment with the model made by Windsvold was carried out. Details about this can be found in Appendix C.1.

Trond Innset from NTNU assisted in the modification and building of the model. Terje Rosten and Torgeir Wahl contributed to the installation of measuring instruments and conduction of the model tests. The multi-torus has been tested in regular and irregular waves with and without a weighted membrane. The main goal of the experiment has been to measure the differences in behaviour between the models with and without membrane. The model was made in scale 1:50 and all dimensions were scaled according to Froude scaling of which the theoretical approach is presented in Appendix A.1.
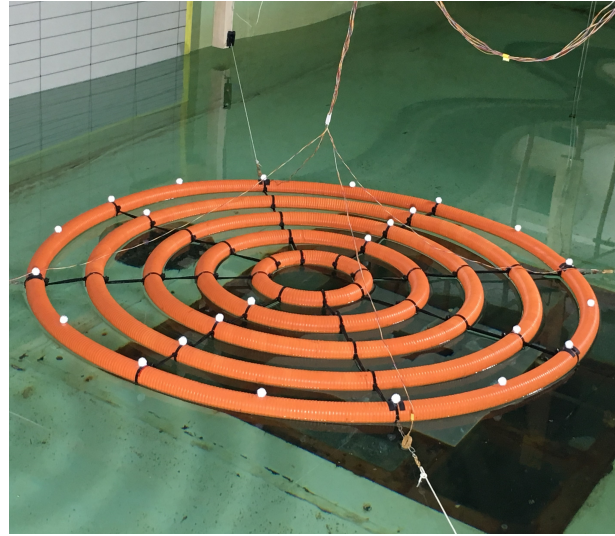
4.1 Multi-torus

Figure 4.1 shows the multi-torus model tested during the first stage of the experiment. The model is composed of 5 floating tori connected with trusses at 8 symmetrical positions around each torus. The connection points correspond to the blue circles illustrated in figure 4.1 (a). Each truss has an initial pre-tensioned length of 65.25mm and the tori has a diameter of 32mm. This gives the total diameter of the floating multi-torus to have a diameter of 1.0m. It should be noted that the properties of the trusses installed in this model are different from the ones used in the model tested by [Windsvold, 2018]. Changes and effects seen from this will be discussed later. The main parameters of the multi-torus in model and full scale can be found in table 4.1.

Corrugated plastic tubes with water-repellent tape wrapped around, as shown in figure 4.2 (c), is used to model the tori. The tape is applied to make the tubes smoother, as well as increasing the bending stiffness of the tubes. The bending stiffness EI was calculated from equation (2.2) after testing done by [Windsvold, 2018]. Elastic rings, attached with a simple knot around the
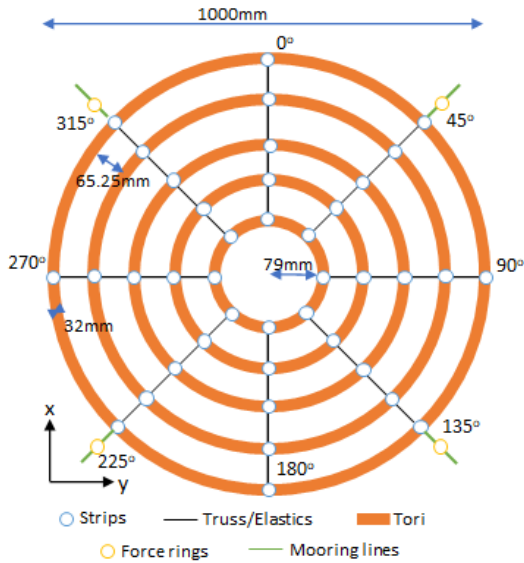
(a) Definition of multi-torus model components.

(b) Multi-torus installed in basin with motion capture globes registering motion during the tests.

Figure 4.1: Illustration of model with truss attachment points at 8 symmetrical positions around the tori and 4 mooring line attachment points. The model diameter D is 1.0m, the torus diameter d_t is 32mm and the truss length l_t is 65.25mm. The global coordinate system has its origin at the centre of the tori.

strips at each end, are used as trusses to connect the tori together, as seen in figure 4.2 (a) and (b). Length of the elastics is adapted such that they are installed with an initial pre-tension to avoid snap loads in the trusses. Elastics have a diameter of 3 mm and consists of a rubber core with a polyester coating. As the load-deflection relationship of the truss stiffness is defined according to equation (2.3), the spring stiffness coefficient k_t is found by applying an axial load and measuring the axial deflection. The model was built after design as in figure 4.1 (a) and the actual weight/dimension properties in model and full scale are displayed in Appendix B.1.

Table 4.1: Main parameters of multi-torus in model scale and full scale. Some of the data are taken from [Windsvold, 2018].

Description	Parameter	Model scale	Full scale
Cross-sectional diameter of torus	d_t	32 mm	1.6 m
Torus mass per unit length	m_t	0.257 kg/m	642.5 kg/m
Torus bending stiffness	EI	0.8467 Nm^2	2.65 $\times 10^8 Nm^2$
Mooring-line spring stiffness	k_s	14.0 N/m	35.9 kN/m
Truss spring stiffness	k_c	57.9 N/m	148.4 kN/m
Cross-sectional diameter of truss	d_c	3 mm	0.15 m

(a) Connecting tori together.

(b) Elastic knotted on strips in each end.

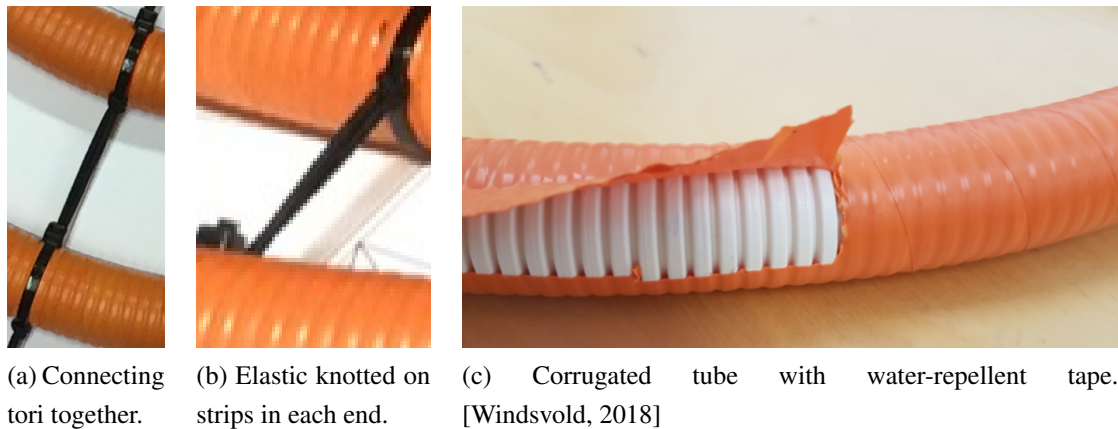(c) Corrugated tube with water-repellent tape. [Windsvold, 2018]

Figure 4.2: Illustrations of how the tori are connected together with an elastic ring knotted on strips in each end and the corrugated tube with water-repellent tape. The picture in (c) is from [Windsvold, 2018].

4.2 Multi-torus with membrane

In the second stage of the experiment, a membrane is installed onto the model as illustrated in figure 4.3. 5g weights are distributed over the surface to model a realistic total weight of the membrane, which in reality will be solar panels which are installed on top of the floater. That means only the floater is tested during the first stage of the experiments, while the complete

(a) Model with membrane and weights distributed over membrane surface

(b) Model with membrane installed in basin
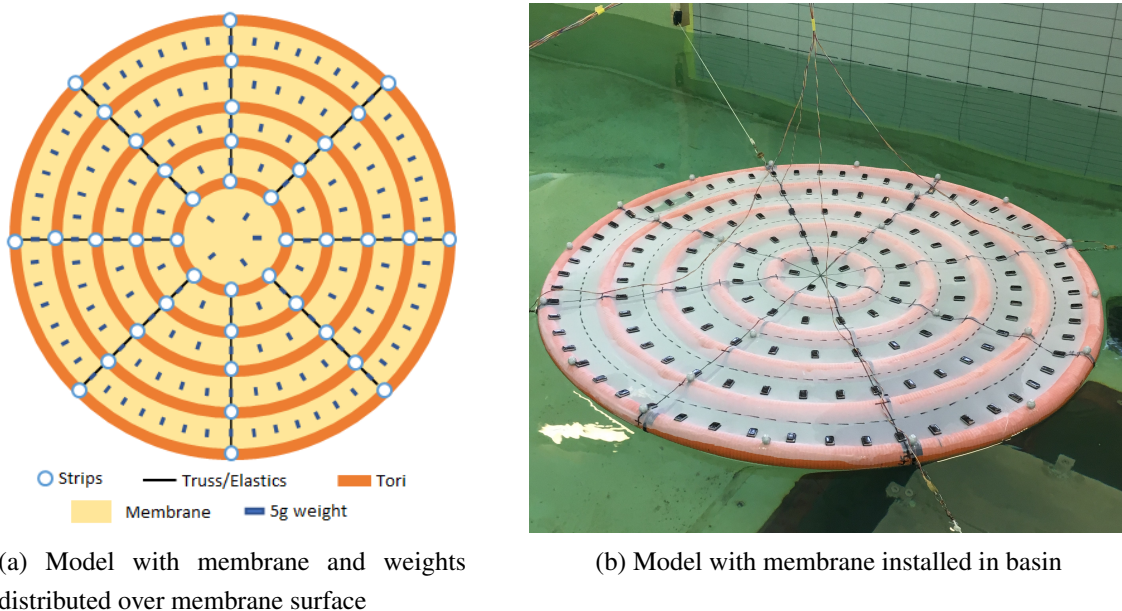
Figure 4.3: Illustration of model with membrane. The membrane is made of a 2-way stretch polyamide material and a number of 5g weights is distributed over the surface to model the correct mass of the solar panels in model scale.

Table 4.2: Weight distribution on membrane. 5g weights are distributed as symmetrically and equally as possible over the surface of the membrane. The weights are positions in between the tori.

Position	5g pieces [-]	Total weight [g]
Torus 1 - 2	56	280
Torus 2 - 3	40	200
Torus 3 - 4	24	120
Torus 4 - 5	16	80
Inside torus 5	5	25
Membrane	-	80
Total	141	785

planned structure is tested during the second stage. The goal is to compare the results, in order to see if the behaviour of the model changes when the membrane is installed. It is desired to use a flexible and elastic membrane, in order to keep most of the floater elasticity disturbed by waves. The membrane is modelled by a 2-way stretch polyamide material.

As it is assumed that the weight of the solar panels in full scale will be 50kg/m^2, the weight of the membrane will be 1kg/m^2 in model scale. As the total area of the membrane covers 0.785 m^2, the total weight of the membrane is 785g. The membrane material weighs 80g, which means 780g should be distributed over the surface. 5g metal weights with a dimension $L \times B \times H = 1cm \times 1.9cm \times 0.2cm$ are chosen to model the solar panels. The distribution of mass can be found in table 4.2. The weights are positioned symmetrically onto the model, in between the tori in order to keep as much of the natural membrane behaviour as possible. The membrane is pre-tensioned when installing onto the model and attached to the top of each torus by glue. As the first membrane set-up (m1) collapsed after a few days of use and exposure to waves, a new and more pre-tensioned membrane (m2) was installed to repeat certain tests. The two membrane set-ups are referred to as m1 and m2 in the rest of the report.

4.3   Set-up

The laboratory basin *Lilletanken* has a length L of 25m, a width B of 2.5m and the water depth h is set to 0.7m. The experimental set-up is described by figure 4.4. A piston wavemaker is installed in the testing facilities, generating waves which are propagating in the negative x-direction. A parabolic beach together with wave dampers are mounted in the opposite end of the basin from the wave maker, in order to avoid reflection of the waves and for the water surface to calm down faster between the wave tests. The centre of the model is positioned 16m from the wave maker. The global axis system is placed with the origin in the centre of the model and at the water surface.
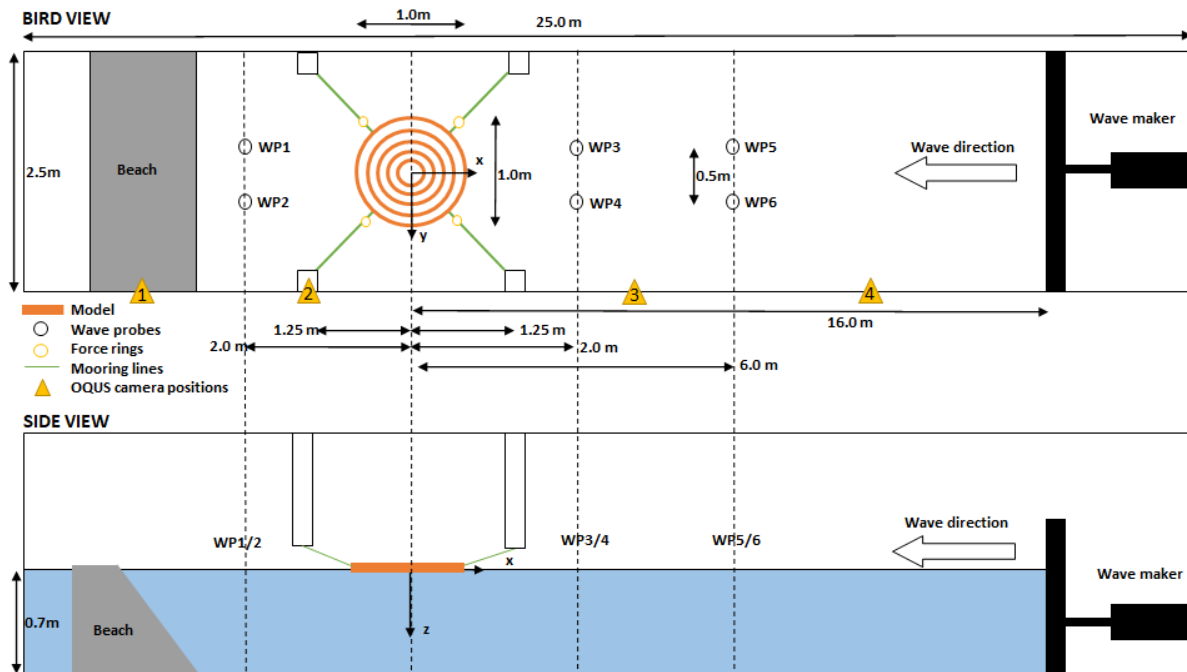
Figure 4.4: Illustration of model test set-up in basin, bird and side view. Global coordinate system defined from the origin of the model initial position.

The model is moored to an initial position with four mooring lines attached to the outer torus at 45°, 135°, 225°and 315°, as illustrated in figure 4.5. The mooring fixations are situated 1.25m horizontally and vertically away from the origin, in order to keep the angles of the mooring lines orthogonal. Each line consists of a force ring, a thin nylon rope, a spring and a chain in the order mentioned, as illustrated in figure 4.5. The spring stiffness coefficient of the springs used in the mooring lines are found by a load-deflection test using equation (2.3) and the main parameters of the mooring lines can be found in table 4.1. Springs are used to modelling the flexibility a mooring rope in full scale normally would have. The mooring lines are tread through a hoise, which is assumed frictionless, at the tank wall. The hoise is positioned only 5cm over water level for the moorings to be horizontally attached. Since the force rings were attached close to the model and the deflection of the ropes are small compared to the forces applied, it is assumed that the eventual elasticity does not affect the mooring line forces. The mooring lines were pre-tensioned with a force of approximately $T_p = 2.6\ [N]$ with accuracy $\pm\ 0.1\ [N]$. The pre-tension is used to avoid snap loads and submergence of the mooring lines during motion in large waves.

The water depth in the tank is not constant since there is a small leakage from the wave maker. To keep the water depth as constant as possible, there is a pump which moves the water back into the basin. The frequency of the water leakage and the pumping is an unknown parameter, and the water depth, therefore, is assumed to be constant during the tests.

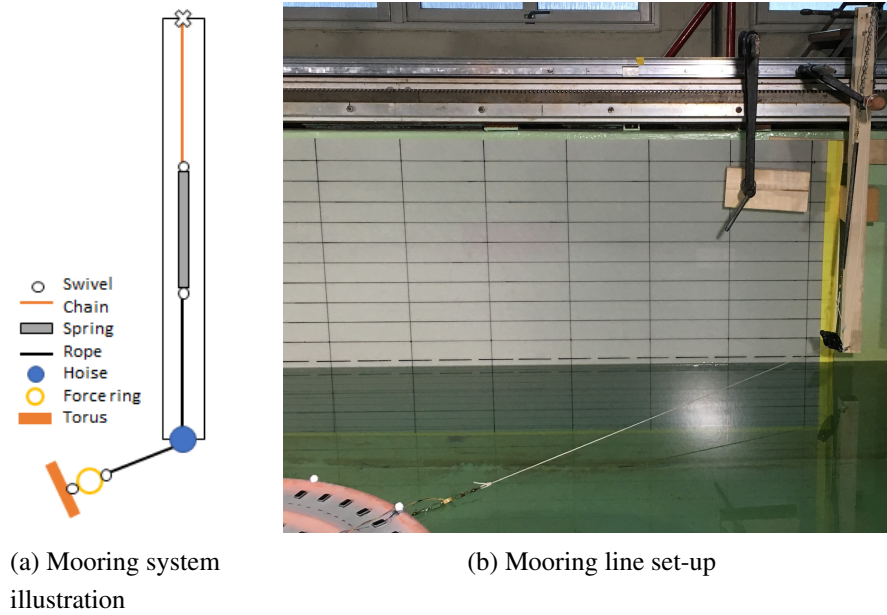(a) Mooring system
illustration

(b) Mooring line set-up

Figure 4.5: Illustration of mooring system set-up which is composed of a chain, a spring, a rope which goes through a frictionless hoise a few centimetres above water level and a force ring fixed between the mooring rope and the outer torus.

4.3.1 Instrumentation

Motions of the model are measured by 24 Qualisys markers in x-, y- and z-direction. The 24 marker globes are symmetrically distributed over the model in the y-direction. There are 16 globes on the outer torus (No. 1), 4 on torus 2 as well as 2 on torus 3 and 4 on the model without membrane. No globes are positioned on torus 5. When it comes to the model with membrane, the globes are positioned equally as earlier explained on torus 1 and 2, while the 4 last globes are positioned between torus 3 and 4 in order to try to catch up the motions of the membrane during impact from waves. For specific information on position, see figure 4.6. The waves are propagating in the negative x-direction. The globes' positions are captured by 4 cameras mounted on the side walls of the laboratory at positions illustrated in figure 4.4. At least 2 cameras need to be able to capture each marker at all times for the specific position to be registered. If less than 2 cameras are able to register the marker's position, the specific marker's position will be lost. The sampling frequency of the cameras is 20Hz.

The model is also instrumented by 4 force rings which are positioned in the mooring system. Each ring is fixed between the outer torus and the corresponding mooring line rope at 45°, 135°, 225°and 315°. Swivel keys are used to connect the force ring to torus and mooring line. 6 wave probes are installed in the basin, positioned as in figure 4.4. All wave probes are placed in pair of 2 with 0.5m distance. That means they are all positioned 1.0m from the wall on each side. WP1/2 are positioned 2m behind the model in the x-direction, WP3/4 2m in front of the model and WP5/6 6m in front of the model. The sampling frequency of the wave probes and the force

(a) No membrane   (b) With membrane
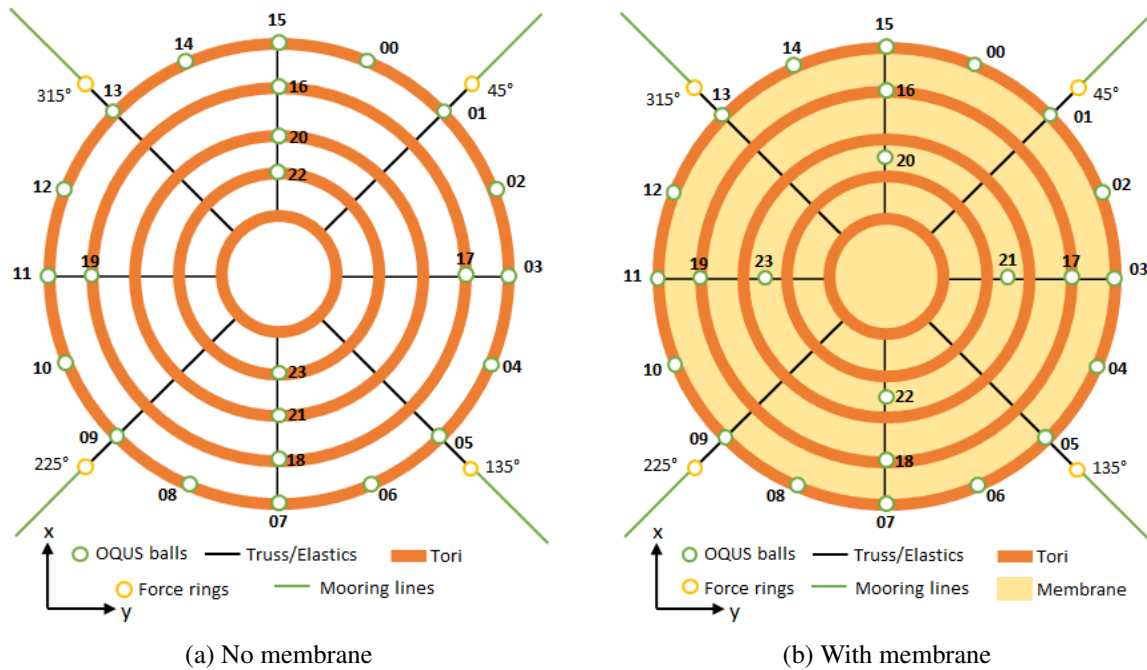
Figure 4.6: Definition of position of Qualisys globes on model during tests with and without membrane. During the tests without membrane, all 24 motion capture globes were positioned symmetrically on top of the tori. 16 globes were placed on the outer torus (No. 1), 4 globes on torus 2 with position 0°, 90°etc. and 2 at 0°and 180°on torus 3 and 4. No globes were positioned on torus 5.

rings is 200Hz with a low pass filter with cut-off frequency 20Hz.

The channel description explaining which measurement devices are attached to each channel is attached in Appendix B.2.

4.3.2 Calibration

Calibration of the physical measuring devices was done by lab technician Terje Rosten from NTNU. Before calibrating, a zero reference is taken on all measuring equipment. This is done as the sensors are sensitive to numerous parameters, like temperature, which is not interesting in these tests. By calibrating, the goal is to find a reference to the signal in a relevant physical unit [Steen, 2014]. As both wave probes and force rings are transducing voltage, it is necessary to apply known loads (x) to find an output voltage (y) for several points. From these known values, a calibration factor a can be found by drawing a calibration curve and assuming a linear relation $y = ax + b$. All force rings and wave probes are calibrated separately after a common zero reference has been taken. Calibration of the Qualisys system was completed by lab technician Torgeir Wahl from NTNU.

4.4 Observation studies

During the model tests with regular waves, two cameras with a slow-motion video possibility are positioned in the set-up. The cameras are used to systematically record the behaviour of the different models during exposition to regular waves. This is especially interesting concerning observation and detection of overtopping, but also to discover other behaviour patterns induced by the regular waves. Approximately 10 s of video from each wave test of all test matrices in regular waves are captured during the tests. These are structured and saved in folders according to model and wave series, in order to thoroughly investigate when overtopping occurs on the model.

4.5 Test matrix

In advance of the model tests, planning is necessary in order to use the time available in the laboratory effectively and producing useful test results. Interesting wave periods and steepnesses were chosen based on the conditions pointed out by [Kristiansen and Borvik, 2018], shown in figure 1.3. It is assumed that the solar islands should be possible to station at ocean area's having a significant wave height with 100 year return period lower than $H_s < 7$ m and water depth lower than $h < 600$ m. As the scale of the multi-torus is 1:50, the produced wave series is within the limits of the interesting areas, in addition to using experiences from earlier model tests done by [Windsvold, 2018]. Wave series are made from the Matlab scripts named *generateRegular.m* and *generateIrregular.m* prepared by professor Trygve Kristiansen. The code takes in a *.txt* file with input parameters and writes out a binary file that is read by the program which runs the wave maker and produces the desired wave series. As the sampling frequency of the wavemaker is 50Hz, the output file is written with sampling frequency 50Hz.

Table 4.3: Input to test matrix generation script for regular waves. k is wave number, D is model diameter, N_k is number of wave numbers, H/λ is steepness, $\Delta(H/\lambda)$ is change in steepness for each step, h is water level, N_T is number of wave periods, N_{ramp} is number of ramping periods at start and end of a series and t_{zero} is the pause time between each series of waves.

Test	kD_{min} $[m^2]$	kD_{max} $[m^2]$	N_k [-]	$(H/\lambda)_{min}$ [-]	$(H/\lambda)_{max}$ [-]	$\Delta(H/\lambda)$ [-]	h [m]	N_T [-]	N_{ramp} [-]	t_{zero} [s]
1060	1.3764	12.5759	60	60	60	60	0.7	60	5	180
1050	1.3764	12.5759	60	50	50	50	0.7	60	5	180
1040	1.3764	12.5759	60	40	40	40	0.7	60	5	180
1030	1.3764	12.5759	60	30	30	30	0.7	60	5	180
3000	3.2146	5.5938	1	60	30	30	0.7	60	5	180

4.5.1 Regular waves

For the regular wave files, the test matrix gradually runs through the desired wave numbers k with constant steepness H/λ, before the steepness is changed and the wave number series are run through again. The reason k is used as the variating parameter for the wave series is that then the wave number varies linearly. Results will have a better flow since it will be most interesting to present the results as a function of kR, where R is the radius of the torus.

The necessary input parameters to produce regular waves are the variation in wave number, the variation in steepness, the water level h, the number of wave periods N_T, the number of ramping wave periods N_{ramp} and the pause time between each wave series t_{zero}. In general, the water depth is set to 0.7m, there are run 60 wave periods for each wave type and the pause is set to 180s. N_k describes the number of different wave numbers which are going to be generated linearly between the minimum and maximum value set. $\Delta(H/\lambda)$ is the variation in steepness between each test from minimum to maximum. The parameters and test matrices used in the regular wave series tests can be found in table 4.3.

4.5.2 Irregular waves

For the irregular wave files, the input parameters are different. The spectral peak period T_p and the significant wave height H_s are the variating parameters. γ, the seed and the amplification factor are given for reproducibility of the irregular wave series. The wave generation file is
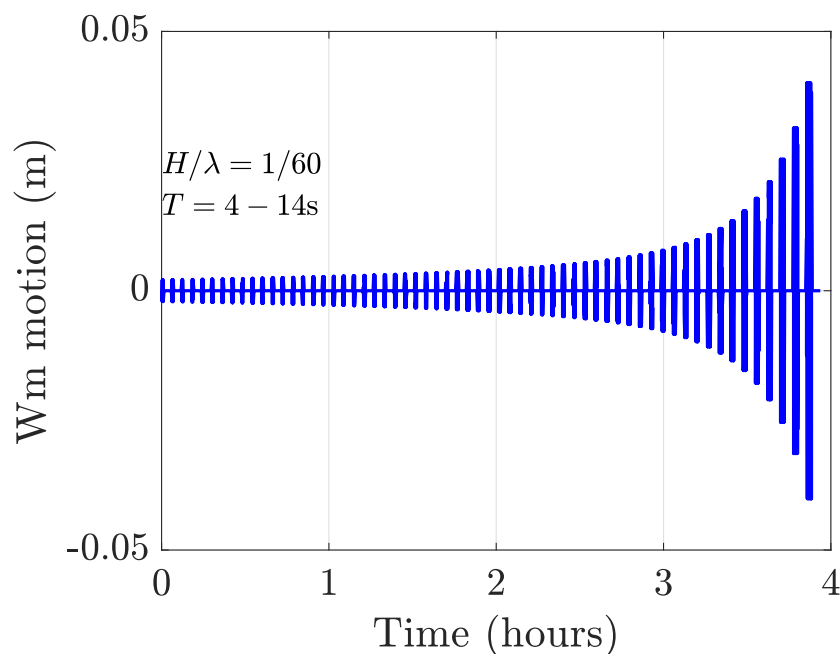
Figure 4.7: The figure illustrates the wave maker motion of a test file named 1060, which runs through 61 wave periods from 4-14s (full scale) with constant steepness 1/60 (model scale). W_m is the wave maker motion.

Table 4.4: Input to test matrix generation script for irregular waves. T_p is spectral peak period, H_s is significant wave height, NH_s is number of series with variating significant wave height, dH_s is change in significant wave height per step, h is the water level, Seed, Amp. factor and γ are JONSWAP spectrum parameters and t_{zero} is the pause time between each series of waves.

Test series	T_p	H_s	NH_s	dH_s	γ	h	Seed	Amp. factor	t_{zero}
	[s]	[m]	[-]	[m]	[-]	[m]	[-]	[-]	[-]
2006	6.0	1.0	4	0.5	0	0.7	101	1	240
2008	8.0	2.0	3	0.5	0	0.7	101	1	240
2010	10.0	2.0	3	0.5	0	0.7	101	1	240
2012	12.0	3.0	3	0.5	0	0.7	101	1	240

using a JONSWAP spectrum. NH_s is the number of significant wave heights which are to be tested for the given spectral peak period, while dH_s is the step which the significant wave height increases by for each test. The pause time t_{zero} between each wave series is 240s. The combination of parameters run is selected from [Faltinsen, 1993, table 2.2, p.30] which gives information about the joint frequency of significant wave height and the spectral peak period for the North Sea.
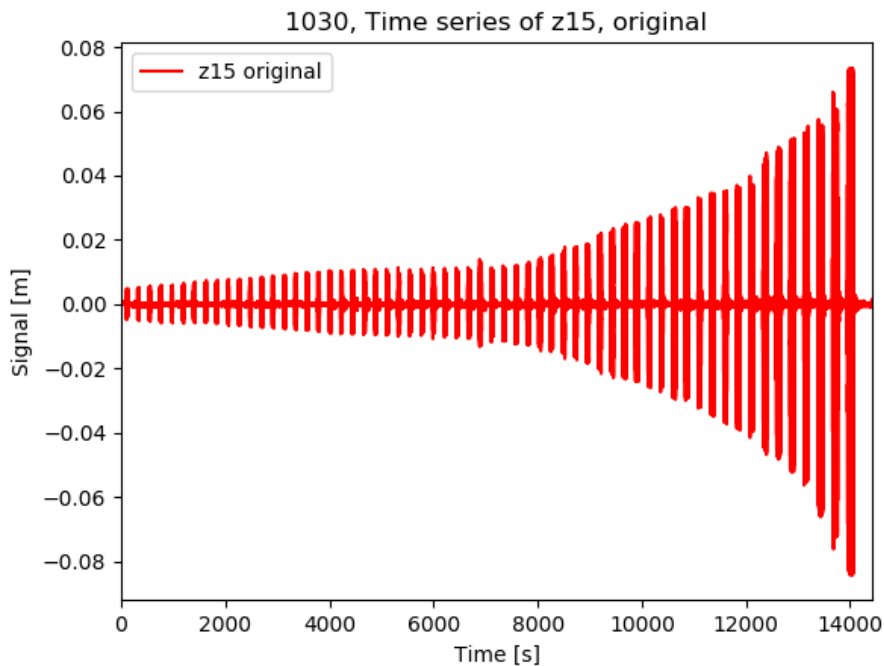
Figure 4.8: Time series of globe no. 15 in z-direction during wave test 3, test number 3000, on model with membrane 2. Globe 15 is positioned on the outer torus, at 0°.

(a) Original
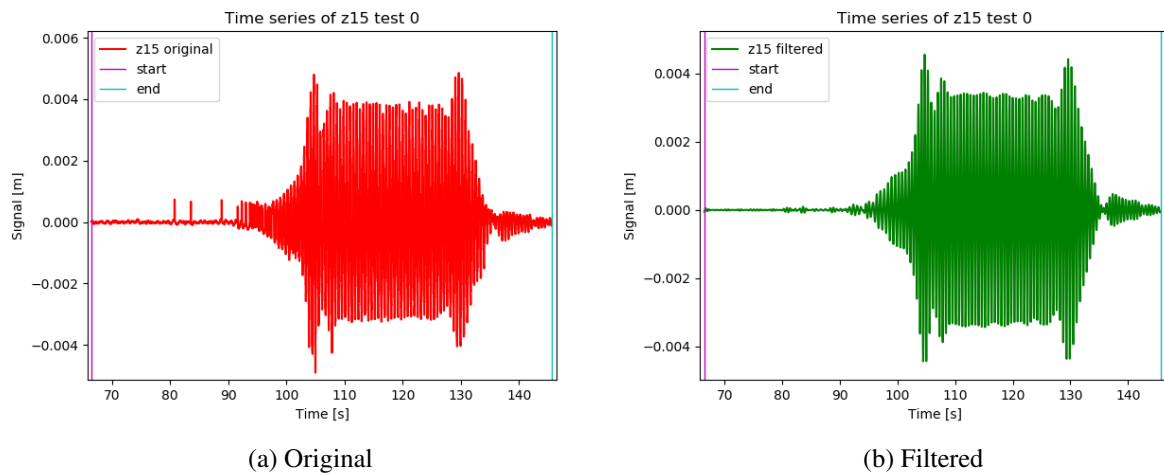
(b) Filtered

Figure 4.9: Chosen time interval to be filtered for wave no. 0, test no. 1030 of globe 15 in vertical direction. This time series is used when the data from this test number is filtered with a bandpass filter of 0.7 to 1.3 times the wave period to extract the first harmonic response. Original data to the left, filtered data to the right.

4.6 Post-processing

Python has been used for post-processing of the experimental results. A total of 88 channels were recorded during each test. Out of these were 24 Qualisys globes in three directions, 6 wave probes, 4 force rings, the wavemaker flap position and time. Specific information about each channel can be found in Appendix B.2. 46 tests were collected measurement data from and 28 out of these produced usable data. A large amount of data makes the job to post-process relevant and correct results important. Discrete binary Catman files are saved from the tests and imported to Python by a function named *catmanreader.py* (version February 2019) made by David Kristiansen.

All data is saved with a sampling frequency of 200 Hz. That means a sample is saved every 0.005 s. The data collected from the Qualisys system have a sampling frequency of 20 Hz but are saved with the same sampling frequency as all the other results. This makes filtering of these measurements even more important, for the data to be usable. In the right plot of figure 4.10, an example of a time series collected from the motion capture system is presented. It can be discussed whether the sampling frequency of the Qualisys system is high enough to capture all variations of the model's behaviour. According to Nyquist frequency, at least 2 samples per wave period are necessary to draw a reasonable picture of the motion [Steen, 2014]. Looking at the right plot of figure 4.10 again, it is seen that there are about 12 registered points through one wave period, which should be enough. Remark that the test presented in the figure is the smallest wave period tested, corresponding to T = 4.0 s in full scale. For complete wave properties of all waves tested, see Appendix B.3.

Table 4.5: Overview of tests with false measurements in regular waves. Tests with wave steepnesses 1/40 and 1/50 are not included here, as analyses of these have not been completed due to too many false tests and lack of time to repeat these steepnesses for both models. Table B.3 shows the wave parameters corresponding to the test numbers.

Test name	Test matrix	Model	False tests from Qualisys markers
1030	1030	No membrane	31,49,50
1060_complete	1060	No membrane	60
1030_m1	1030	Membrane set-up 1	34-43
1060_m1	1060	Membrane set-up 1	47-52
1030_m2	1030	Membrane set-up 2	All (other error)
1060_m2	1060	Membrane set-up 2	All (other error)

4.6.1 Regular waves

After extracting the binary files using the Catman reader function, the complete time series of all channels are saved in a large matrix. The different channels are saved into smaller matrices, corresponding to the signal type before the post-processing starts. Since the finite water depth function of the wave number k is implicit, an iteration function is needed to find the wave number corresponding to the smallest largest wave period tested. Further, a linear vector of wave numbers corresponding to the one made in the test matrices is found. The wave period, velocity and group velocity are also found, since they will be used later.

A choice is made to run the complete time series of the wave probes and force rings through a low-pass filter of 0.1 Hz, in order to set the mean value to zero throughout the series. This is necessary due to 2 different reasons. Since the water level in the basin is not constant throughout the tests, that would cause an error source when comparing the different waves. By suppressing the mean value, the water level mean value is set to zero between each wave series. The second reason is drifting of the force rings since the test matrices are up to 4 hours long. Looking at the complete test series of globe 15 in the vertical direction in figure 4.8, it is considered that the Qualisys system is able to stabilize around zero between each wave series and therefore not necessary to use the low-pass filter on these ahead of the next steps of analysis.

For some of the tests, the results are missing due to loss of signal on the OQUS camera 2 in the Qualisys system. This causes some of the wave series to be incomplete and some times there is not enough data to extract a stationary time window. In these cases, the stationary part of the wave series either has to be deleted from the analysis or replaced by repeated tests. That means all tests have to be verified before the stationary time window is further used. When it is possible, usable data is sewn together to create a complete data set of the current steepness and model. False tests deleted from the measurements used in the results are presented in table 4.5.
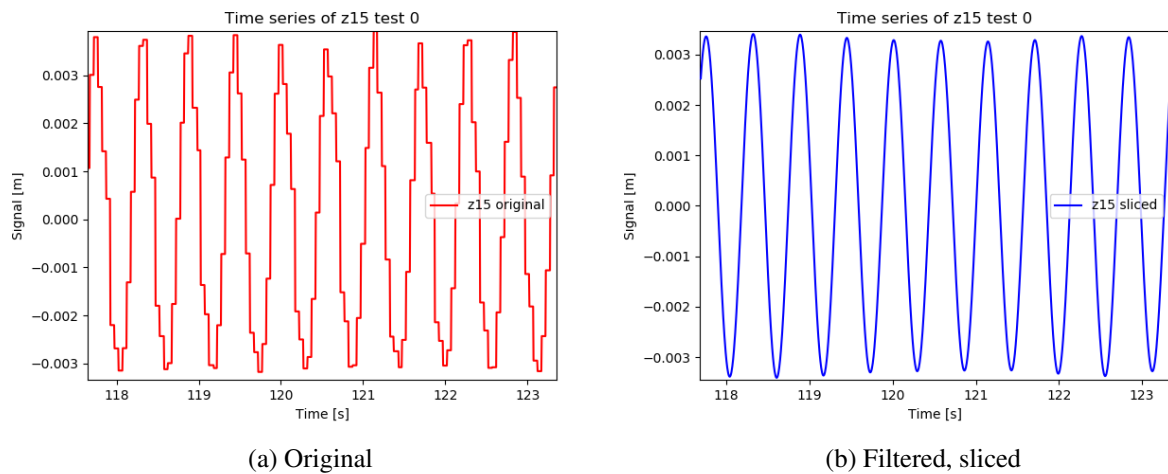
(a) Original

(b) Filtered, sliced

Figure 4.10: Chosen time interval to be saved for further processing. Wave no. 0, test no. 1030 of globe 15 in vertical direction. This time series is extracted after the time series in figure 4.9 has been filtered to signify only the first harmonic response. The time series displayed here represents 10 wave periods. Original data to the left, filtered data to the right.

The raw data of the flap position is used to find the starting time of the first wave. Further, the wave velocity, group velocity and distances between the different devices have been used to find the relevant time interval. In the first place, a time interval of around 150 time periods around each wave series is chosen for a filtering process to extract the first harmonic response. A time window like in figure 4.9 is chosen for this matter. The original data series is presented in the left plot of the figure, while the filtered series is plotted to the right. Further, since the test matrices include a ramping of 5 wave periods at both start and end of each wave series, the stationary part of the signal needs to be selected for further ahead of further analysis. A time window of 10 wave periods is selected in the stationary part of the time series like presented in figure 4.10. The original and filtered measurements are plotted on top of each other in figure 4.13 to make it possible to see the difference between the steps. Finally, the extracted time windows are saved in a binary file format named pickle, which is commonly used in Python.

Vertical RAOs from regular wave tests

Wanting to plot the vertical response amplitude operators of the outer torus, the stationary time intervals extracted from the raw data will be used. As there are 16 Qualisys globes on the outer torus, a modal analysis, as described in section 2.5, will be used to combine the motions recorded by each globe and separate them into modal responses. To find the amplitude of the modal responses, the standard deviation is used. Further, the amplitude of the modal response of each mode is divided by the amplitude of the corresponding wave. This is described further in section 2.6.

Horizontal RAOs from regular wave tests

Since the model is circular and the motion capture globes are positioned around the tori, horizontal responses cannot be directly extracted. It is necessary to estimate the responses in surge and sway by averaging the measured motions in the corresponding directions. This is described in section 2.5.2 To find the horizontal responses of the outer torus, the measurements of the 16 motion capture globes are used in the averaging. Finally, the standard deviation is used to estimate the amplitude and the modal response amplitude is divided by the wave amplitude of the corresponding wave, like for the vertical modes.

As the model has a circular shape, it will also have modes related to this. Different ovalization modes are the effect of the shape. A radial parameter is found from the measured motions in the horizontal directions. Through modal analysis, the modal responses in the radial direction can also be extracted. From this, the RAOs are found using the same method as described above. Remark that the first mode (n=0) is unphysical, and the first row and column from the modal analysis system needs to be deleted.

RAOs for 7 modes are found in the vertical direction, while surge, sway and 6 ovalization modes are calculated in the horizontal direction for regular waves. All regular wave tests with usable data are run through the procedure described above.

4.6.2 Irregular waves

As for the regular time series, the measurement files are extracted using the Catman reader. The file is saved in exactly the same format. Looking at figure 4.11, a complete time series of an irregular test matrix is shown. From this, each a time interval from each test is chosen out and filtered before it is saved in a pickle format. Wanting to calculate the vertical RAOs of the outer torus, as well as wave and response spectra, the time series are treated in a repeating loop completing the same procedure for each test.

Vertical RAOs from irregular wave tests

As for the regular wave tests, the measurements of the 16 Qualisys markers on the outer torus have to be run through a modal analysis function, in order to sum up the contribution to each mode from each marker. Further, the results of the modal analysis are run through a built-in function in the scipy signal package named *welch* that completes a spectral analysis and returns a frequency vector together with the power spectral density of the time series. The result of the spectral analysis using welch is dependent of the input variables like length of the time window, the length of the overlapping time window and the length of the segments that are run through the Fast Fourier. These parameters are carefully tuned in order to give a correct representation of the resulting spectra.

The power spectral density of a modal response time series is thus the response spectrum of each vertical mode. The same spectral analysis is completed for WP1, which is the wave probe the least impacted away by the model. This returns the measured wave spectrum. The response spectrum is divided on the wave spectrum, which returns the transfer function squared. The square root of the absolute value of the transfer function returns the response amplitude operator of the irregular wave time series, as described in equation (2.15).

Figure 4.12 shows an example of a heave RAO from a wave series with T_p = 6s and H_s=1.0m. A response amplitude operator calculated directly from the spectral analysis is plotted towards a smoothed RAO. The RAO is smoothed by use of a second order Savitzky-Golay filter averaging the vector over a time window of 11 values.
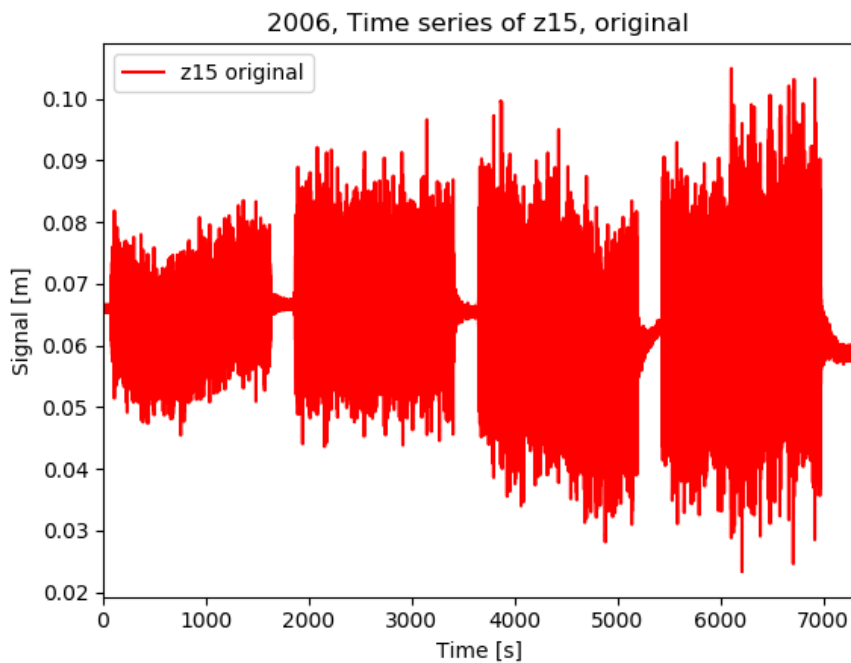
Figure 4.11: Example of irregular times series, T_p = 6.0s, H_s = 1.0m, 1.5m, 2.0m, 2.5m.
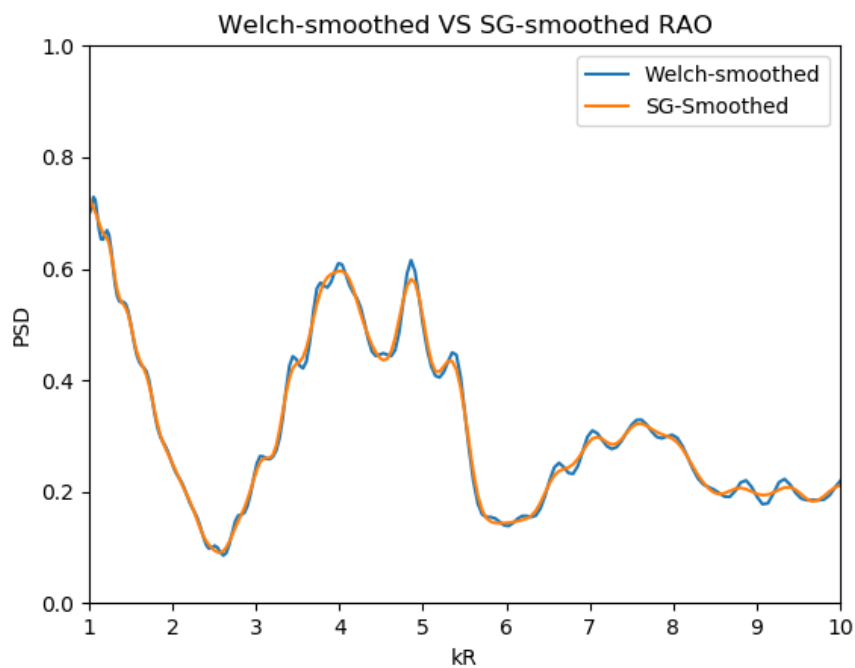
Figure 4.12: Example of smoothing of heave RAO. The heave RAO of the irregular wave series of T_p= 6s and H_s= 1.0m has been run through a smoothing filter for better representation. As the Welch PSD filter from the scipy signal package is used for the spectral analysis. The input parameters using this are also tuned in order to give a smoother representation of the RAO. A second order Savitzky-Golay filter has been used to average the values of selected small value time windows in order to smooth the RAO.
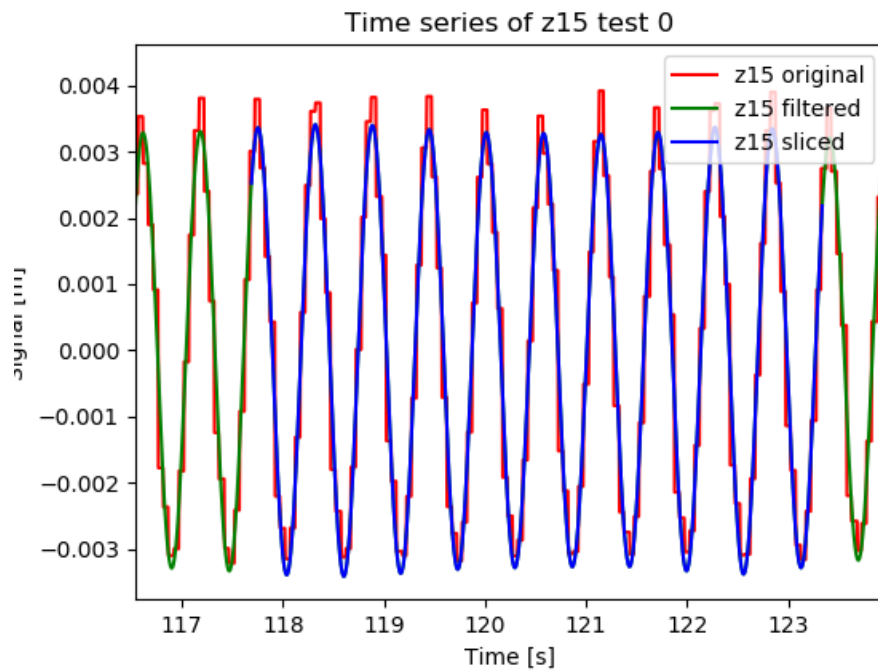
(a) Zoomed
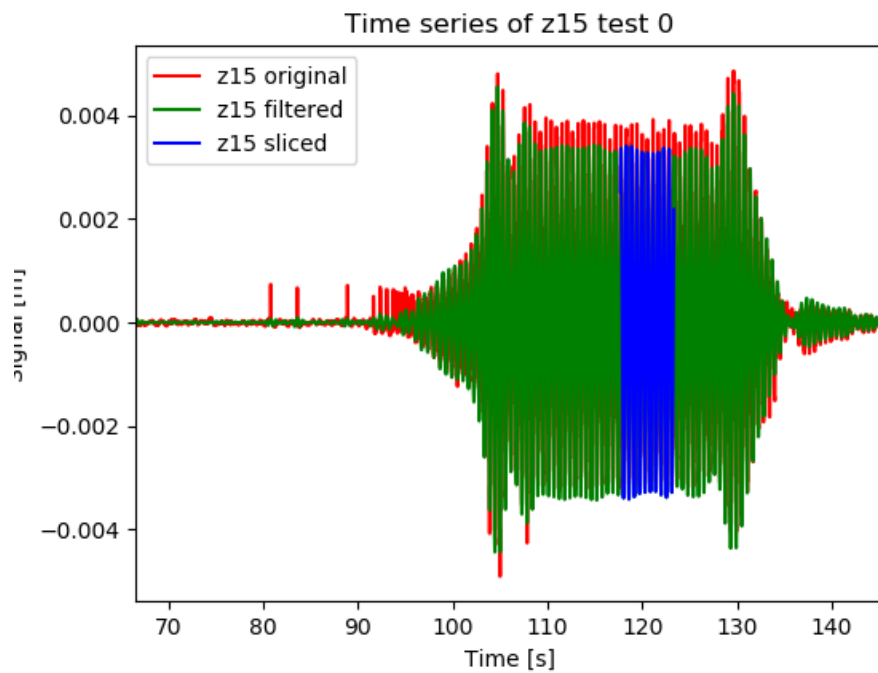
(b) Time window used when filtering

Figure 4.13: Wave no. 0, test no. 1030 of globe 15 in vertical direction. Globe 15 is positioned on the outer torus, at 0°(see figure 4.6). The red line (behind) is the original measurement. The green line presents the bandpass filtered signal at 0.7 and 1.3 times the wave period. That means the response of the first harmonic. The blue signal (sliced mid part) corresponds to the 10 wave periods of the signal which are saved and will be used in further analysis.

Chapter 5

Results and Discussion

In this chapter, the experimental and numerical results of the thesis will be presented and discussed. The discussion will comment on the experimental and numerical results, compare them with relevant studies and comment on the methods used. From the regular wave tests, vertical, horizontal and radial response amplitude operators from the outer torus, as well as overtopping and a sensitivity study of the wave amplitude are presented. Wave and response spectra and the vertical RAOs of the outer torus, are presented from the irregular wave tests. When it comes to the numerical study, results of the verification studies are briefly explained and more details can be found in Appendix E.1. Unfortunately, the numerical results with the coupled model are not physically correct, as the model has an unresolved bug in the code. Numerous attempts to find the bug have been carried out, without success. The bug is most likely related to the scripting and not the theoretical implementation steps.

From a post perspective, problems with the Qualisys motion capture system during the model tests added another challenge to the post-processing and made it more time-consuming than planned. It would have been favourable to use more time on the implementation and development of the numerical simulation model, due to the complexity of the theoretical models and the coupling between the two. Approximately 65% of the project time has been used on the experiments including preparation, accomplishing and post-processing, compared to 35% on the numerical implementation.

The model tests were conducted during February 2019 and are presented in detail in chapter 4. Some illustrative findings will be presented and discussed in the following, to give the reader an overview of the results and physical phenomenons investigated. More results from the experiment are found in Appendix F. Observation tests with the old multi-torus by [Windsvold, 2018] were conducted in November 2018 during the project thesis. More details and results from these tests can be found in Appendix C.1.
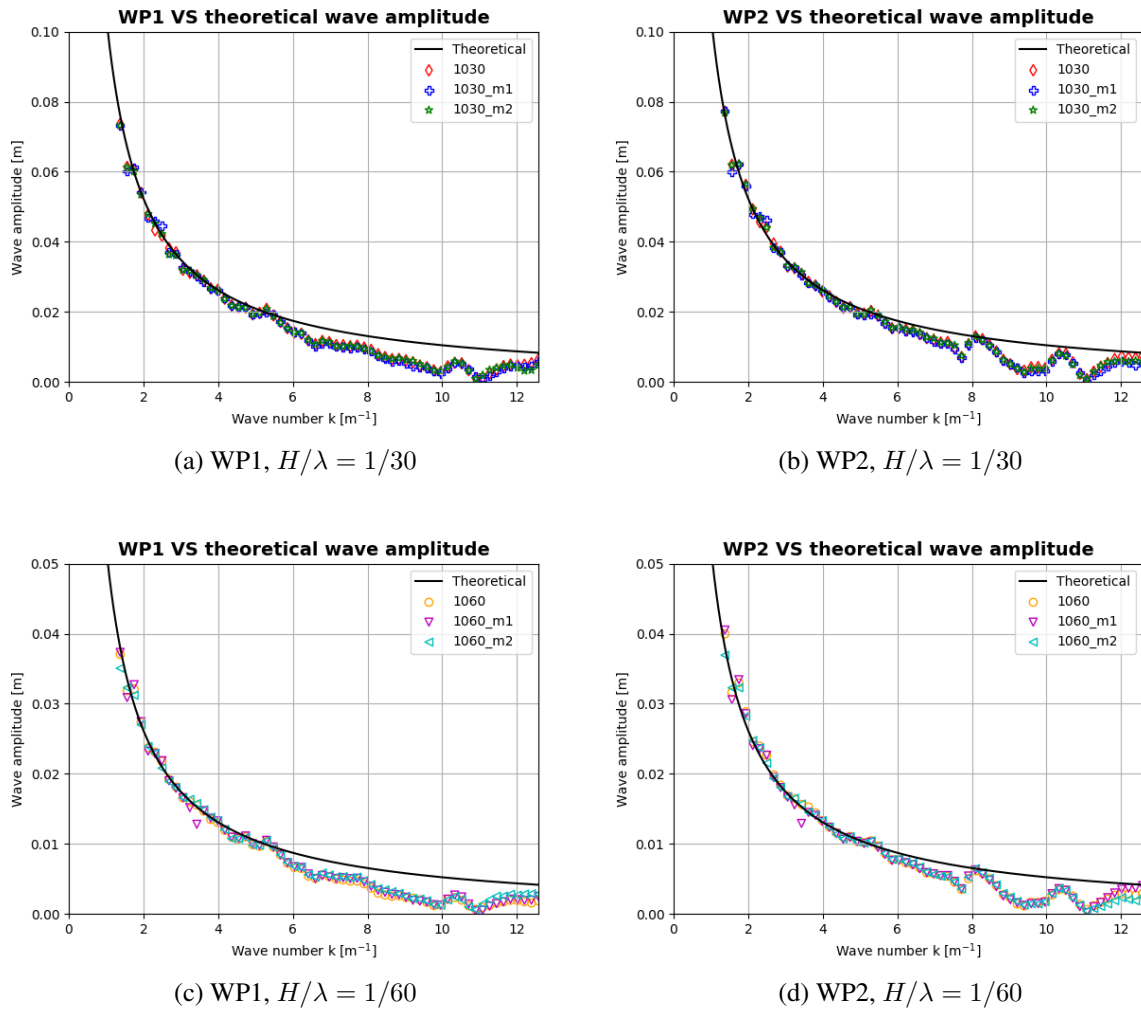
Figure 5.1: Measured wave amplitude at WP1 and WP2 VS theoretical input. m1 signifies the first membrane multi-torus model and m2 the second membrane set-up on the multi-torus. 1030 signifies wave steepness $H/\lambda = 1/30$, whereas 1060 signify wave steepness $H/\lambda = 1/60$.

5.1 Experimental results - regular waves

In this section, experimental results from regular wave series are presented and discussed. First, measured wave amplitudes are presented to verify that these are according to the input amplitudes. Further, time series and RAOs for the outer torus of the models with and without membrane are commented on. Then, the overtopping phenomenon observed is documented and discussed through snapshots from the different wave series. As the first membrane set-up (m1) collapsed after some days of testing, the model was reinstalled with a new membrane (m2). Due to this, there was not enough time to repeat the tests for all steepnesses. Therefore, results for wave steepnesses 1/60 and 1/30 are presented, as these are most complete.

5.1.1 Measured wave amplitudes

In figure 5.1, the measured wave amplitude from wave probes 1 and 2 are presented for steepnesses 1/30 and 1/60. The theoretically calculated wave amplitude using regular wave theory in finite water depth is plotted for comparison. WP1 and WP2 are the wave probes positioned 6m in front of the wavemaker, the furthest away from the model of all the wave probes. As wave series without the model in the basin were not conducted, the measurements from these wave probes were used to avoid radiation of waves and other disturbances on the waves from the model. Three different models have been exposed to the same test matrices and measurements from all three are plotted for both wave probes and steepnesses. m1 and m2 refer to the first and second membrane set-up. It is observed from the figures that the measurements from WP1 are slightly deviating from WP2 for both steepnesses, especially for the larger wave numbers.

The measurements show that the smallest wave amplitudes are deviating more from regular wave theory than the larger. For wave numbers smaller than k = 5.8, the wave amplitudes correspond well with theory. For larger wave numbers, the measured wave amplitudes are smaller than the theoretical and fluctuating. As the wave amplitudes are slowly decreasing for increasing wave number, it becomes evident that the small wave amplitudes have bigger uncertainty. This observation is reinforced by the fact that both wave probes for both steepnesses show the same trend. For kR $\geq$ 5.8, the wave probes show deviating results. The same trend line of amplitudes is shown for WP1 comparing steepnesses, not accounting for the doubling of the amplitudes. This is also true for WP2.

5.1.2 Time series of modal response

In figure 5.2, the time series resulting from the vertical modal analysis are presented for mode 0, 1 and 2 from the wave series with kR = 6.0 of four different test matrices. The figure shows that there are few differences between the modal responses with and without membrane for the same steepness and wave. This is only true for this exact wave period, as it will depend on how the different models respond to the different wave periods. When comparing the two steepnesses, it is seen that the wave height changes as the steepness does, but the quantity of response is equally distributed over the modes for the same wave number. It is seen that the response amplitude for mode 0, 1 and 2 is smaller than the wave amplitude inducing the response. Heave response is dominating, then pitch and finally the first flexible has a small contribution.

5.1.3 RAOs of outermost torus

Response amplitude operators for the outermost torus are obtained by using the method described in section 4.6.1. Vertical, horizontal and radial direction RAOs obtained from regular wave tests are presented in this section. As there were found measuring errors on the Qualisys measurements from all tests of the second membrane model, the results from these tests are excluded from the analysis. The outer torus had 16 Qualisys markers symmetrically distributed
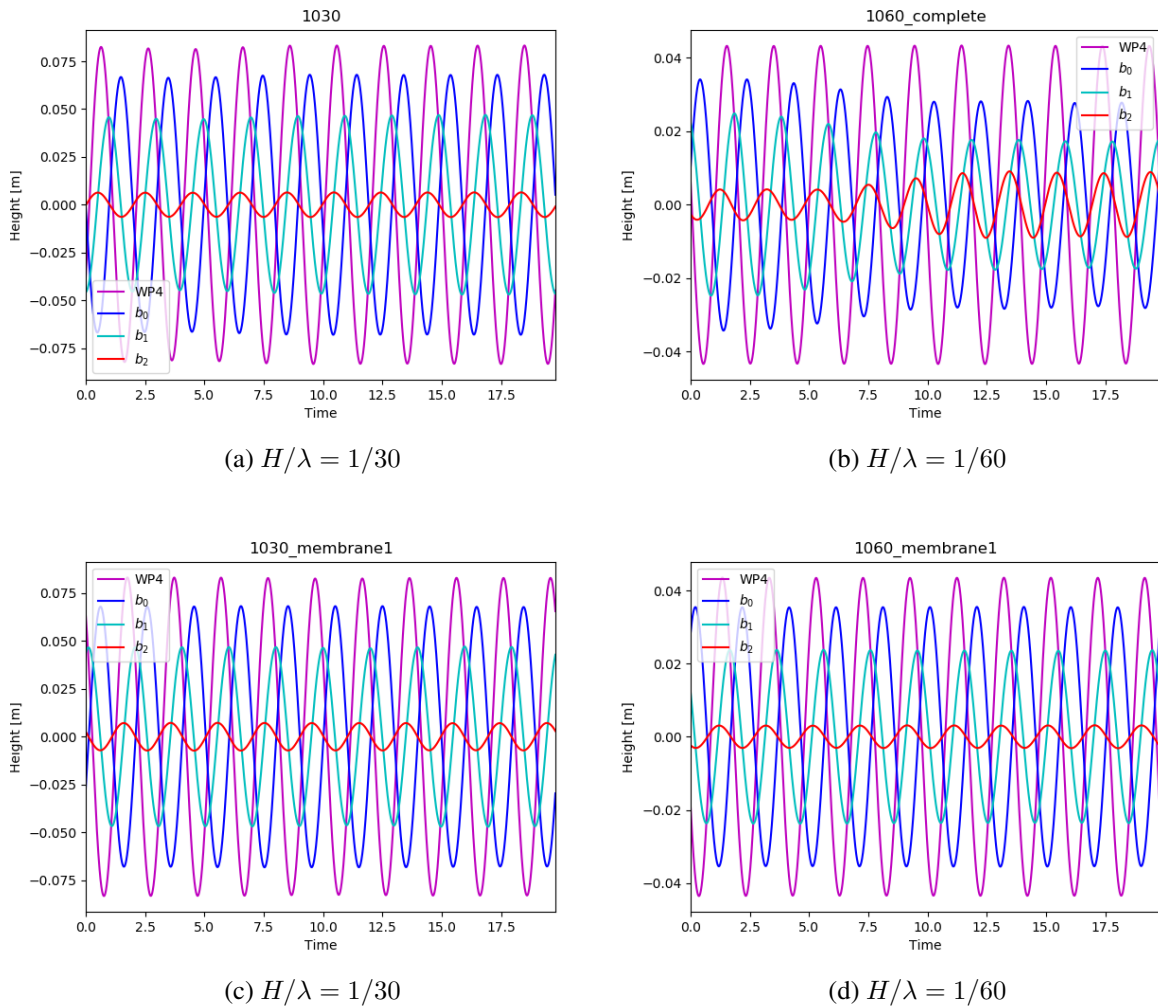
(a) $H/\lambda = 1/30$

(b) $H/\lambda = 1/60$

(c) $H/\lambda = 1/30$

(d) $H/\lambda = 1/60$

Figure 5.2: Resulting modal response time series of mode 0(heave), 1(pitch) and 2(1st flex) compared to the wave inducing the response. All time series are from test 61, for wave steepness 1/30 and 1/60 as well as the models with and without membrane. Membrane 1 signifies the first membrane set-up on the multi-torus. 1030 signifies wave steepness $H/\lambda = 1/30$, whereas 1060 signifies wave steepness $H/\lambda = 1/60$. 1060_complete is the name of a file where the correct measurement results of all wave series in 1060 have been saved and equals the measurements done from the model without membrane of wave steepness 1/60.

over the model. Effect of wave steepness, the effect of the membrane and effect of the wave period will be analysed and discussed.

It should be kept in mind that the results of the model with membrane (m1) are affected by the suppression of tests 47-52 from test matrix 1060, and tests 34-43 from test matrix 1060. The tests 31, 49 and 50 are deleted from the test matrix 1030 and test 60 is deleted from the test matrix 1060 for the model without membrane. This results in no documentation of the changing response in this interval. The tests results are missing as a consequence of the Qualisys system

falling out, which makes the measurements unrepresentative of the real motion of the model during these tests.

Vertical direction

The vertical response amplitude operators for the 7 first modes are calculated. Heave, pitch and the first flexible mode will be presented in this section. The four next modes' RAOs can be found in Appendix F.1.1.

Figure 5.3 shows the vertical RAO in heave for steepnesses $H/\lambda = 1/60$ and $H/\lambda = 1/30$, with and without membrane. The measured RAOs are compared to the RAO calculated using ZFT on the outer torus. All four measured response series in figure 5.3 follow the theoretical representation well from kR 0.69-2.4. The first cancellation period is present at kR = 2.4, which corresponds to a full-scale wave period of 6.47s. For wave numbers higher than kR = 2.4, an increasing phase shift between the theoretical and experimental results is observed. The shape of the response curve for wave numbers higher than kR = 2.4 is also different in the measured results than in ZFT. This is most likely due to the ZFT representing the RAO of a single torus, while the presence of multiple tori in the tested models will change the response. It is assumed that the tori are positioned close enough to affect each other. Presence of water in between the tori permits radiation of waves, which changes the relative motion. The tori are also connected through trusses at 8 symmetrical positions. These connections will contribute to the change in the relative motion of a multi-torus compared to a single-torus model. The effect increases for

(a) Steepness $H/\lambda = 1/60$ \hspace{2cm} (b) Steepness $H/\lambda = 1/30$
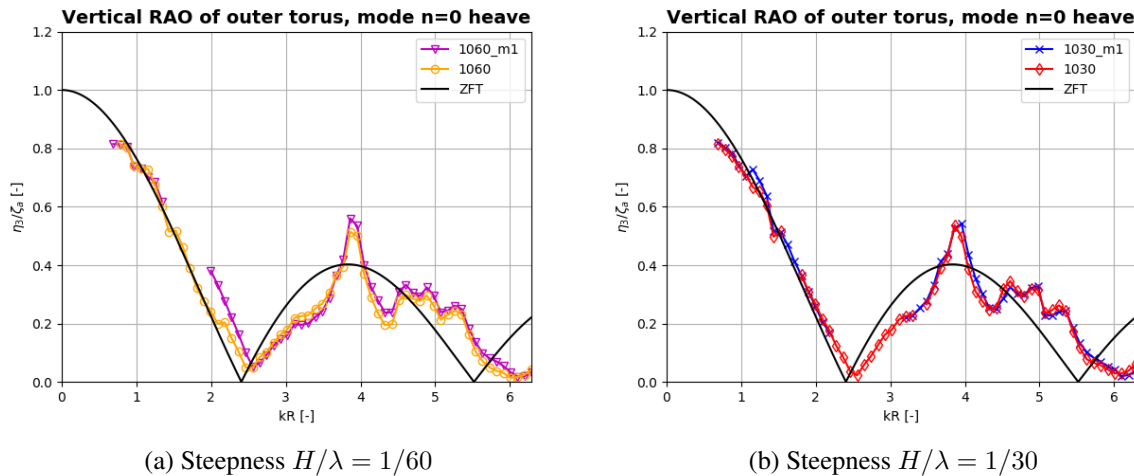
Figure 5.3: Response amplitude operator for the outermost torus in heave (vertical direction, mode 0). Comparing model with and without membrane. $m1$ signifies the first membrane multi-torus model. 1060 and 1030 signify wave steepnesses $H/\lambda = 1/60$ and $H/\lambda = 1/30$ respectively. ZFT for a single-torus is compared to the measurement results. Remark that tests with kR = 2.27-2.65 are deleted from the results of test 1030_m1.
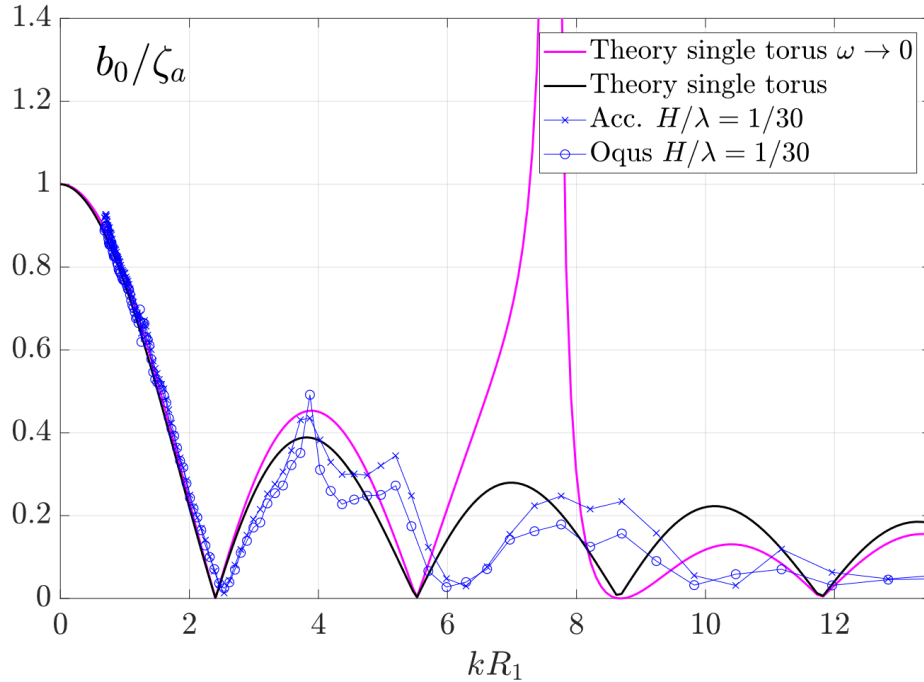
Figure 5.4: Illustration of difference between zero-frequency theory $\omega \to 0$ (ZFT) and low-frequency slender-body theory (LST) [Li, 2017] for heave RAO of the outer torus in the multi-torus. The pink curve corresponds to ZFT and the black curve LST. The blue crosses represent the experimental RAO calculated from accelerometer measurements and the blue circles represent the RAO calculated from Qualisys measurements from the model tests by [Windsvold, 2018]. Courtesy to T. Kristiansen, 2019.

increasing wave numbers as the effect on the relative motion between the tori is stronger for waves with less energy.

It is seen from figure 5.3 that the difference between the response of the model with and without membrane is minimal in heave. This is worth to remark, as the weight of the membrane is realistically scaled from full-scale solar panels. There are few differences between the response of two steepnesses presented as well. This means the model's response in heave is mainly dependent on the period of the wave inducing the motion. Comparing the heave response obtained in these tests with results from [Windsvold, 2018] in figure 5.4, the results show good correspondence. This means the changes that have been made to the multi-torus, including a decrease in mooring line spring stiffness and pre-tension as well as an increase of truss spring stiffness, did not affect the resulting responses in heave significantly. Windsvold used 8 Qualisys markers on the outer torus, which is only half as many as what is used here. It is therefore expected that at least the higher modes should be better represented in these tests.

Remark that the low-frequency slender body theory (LST), developed by [Li, 2017], presented in figure 5.4 will represent the response more precisely than the ZFT for increasing mode order

(a) Steepness $H/\lambda = 1/60$ (b) Steepness $H/\lambda = 1/30$
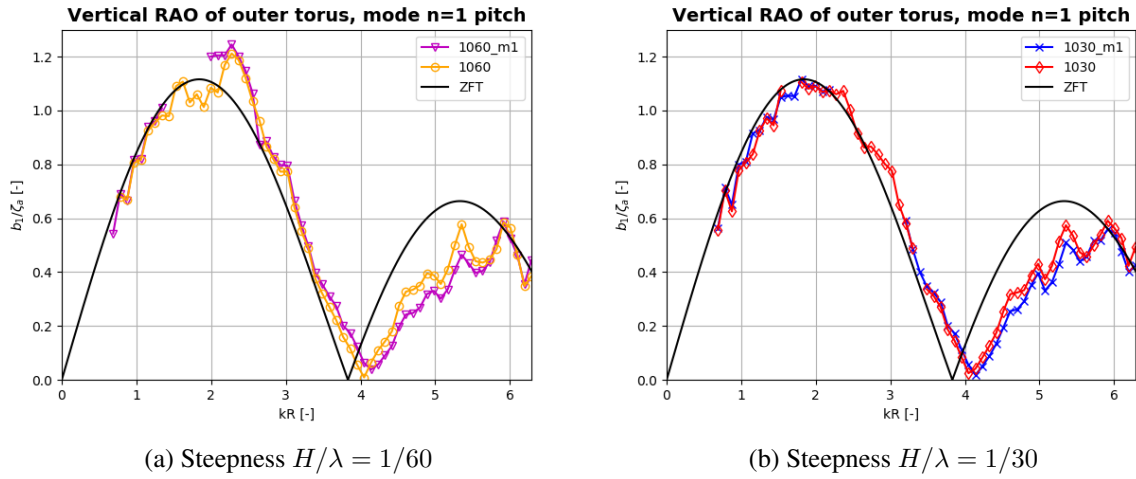
Figure 5.5: RAO for the outermost torus in pitch b_1 (non-dimensional, vertical direction, mode 1). Comparing model with and without membrane. $m1$ signifies the first membrane multi-torus model. 1060 and 1030 signify wave steepnesses $H/\lambda = 1/60$ and $H/\lambda = 1/30$ respectively. ZFT for a single-torus is compared to the measurement results.

and increasing wave frequencies. The reason is that the effect of damping and wave frequencies are accounted for in the LST model. A curiosity of the multi torus model is that for very elevated wave frequencies, it has an infinite number of resonance frequencies for each mode. This is due to the water in between the tori that are causing cancelling effects and negative added mass for very high wave frequencies.

In figure 5.5, the vertical response amplitude for mode 1, pitch, is plotted non-dimensionally. Remark that non-dimensional means the curve does not correspond to the pitch angle, but the non-dimensional RAO b_1/ζ_a representing pitch. The measurements for the models with and without membrane are compared for steepnesses $H/lambda =1/60$ and $H/lambda =1/30$. The RAO curve calculated from ZFT for a single torus is also included. The maximum response amplitude is lower for wave steepness $H/lambda =1/30$, than for $H/lambda = 1/60$. After the first cancellation period at kR = 4.0, the measured responses are not corresponding as well to the ZFT. This can be explained by two main reasons. Firstly, the ZFT only represents a single-torus. Secondly, compared to LST, ZFT represents the response less accurately as mentioned previously.

Also in pitch, the phase shift starts to become visible around the first cancellation period, at kR = 4.0. Again, the phase shift can be explained by that the ZFT is only representing the response of a single torus. It is expected that the cancelling periods will change as an effect of the differences between the multi-torus and the single-torus. Comparing the resulting pitch response with the responses found by [Windsvold, 2018], the results are corresponding well, but slightly deviating for increasing wave numbers. This can be explained by the difference in
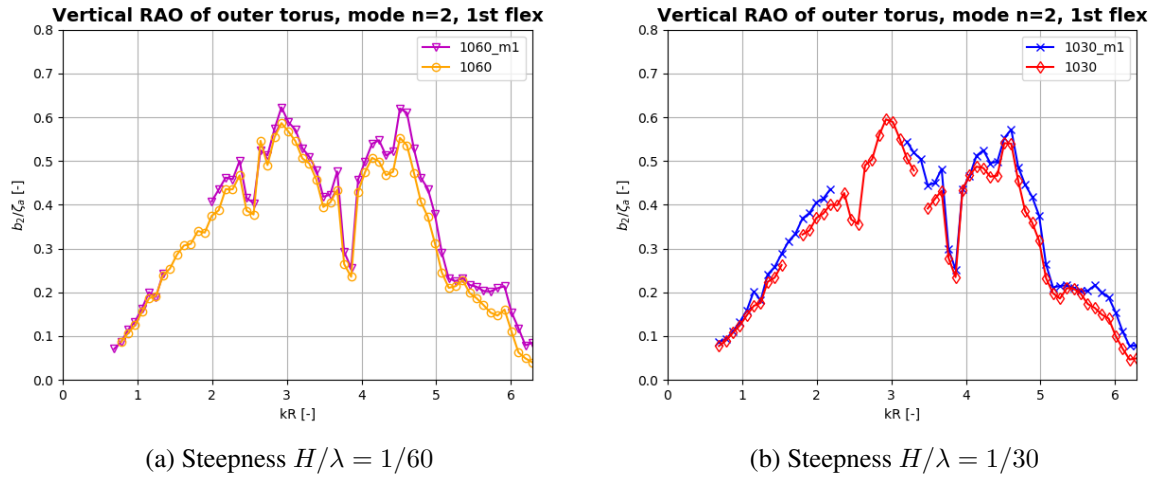
(a) Steepness $H/\lambda = 1/60$ (b) Steepness $H/\lambda = 1/30$

Figure 5.6: RAO for the outermost torus of 1st flexible (vertical direction, mode 2). Comparing model with and without membrane. $m1$ signifies the first membrane multi-torus model. 1060 and 1030 signify wave steepnesses $H/\lambda = 1/60$ and $H/\lambda = 1/30$ respectively.

the number of markers, as 16 markers were used in these tests compared to 8 in the experiment by Windsvold. It is expected that the increased number of markers should increase the accuracy of the higher mode responses calculated by modal analysis. The increased number of markers makes it possible to extend the system of equations and solve for an increased number of modes.

The RAO of the first flexible mode, representing a banana shape seen from the side wall of the basin, is presented in figure 5.6. The response amplitudes show low dependency to the wave steepness and which model is used. That means there is almost no differences between the responses with and without membrane. Compared to the results of the tests by [Windsvold, 2018], the results correspond well in shape and amplitude. However, already before the first cancellation period a phase shift is present. The difference can be explained by the before mentioned difference in the number of markers used to measure the local motion of the torus.

From this mode on, the measurements have not been compared to a theoretical approach. Henceforth, the higher vertical modes, in general, show small response amplitudes. This means the three first modes dominate in vertical response motions of the multi-torus and it is likely that it would suffice to sum up these three modes to find the convergence of the vertical motion.

Horizontal direction

$$T_{1n} = 2\pi\sqrt{\frac{M + a_{11}}{k_m}} \tag{5.1}$$

(a) Steepness $H/\lambda = 1/60$ (b) Steepness $H/\lambda = 1/30$
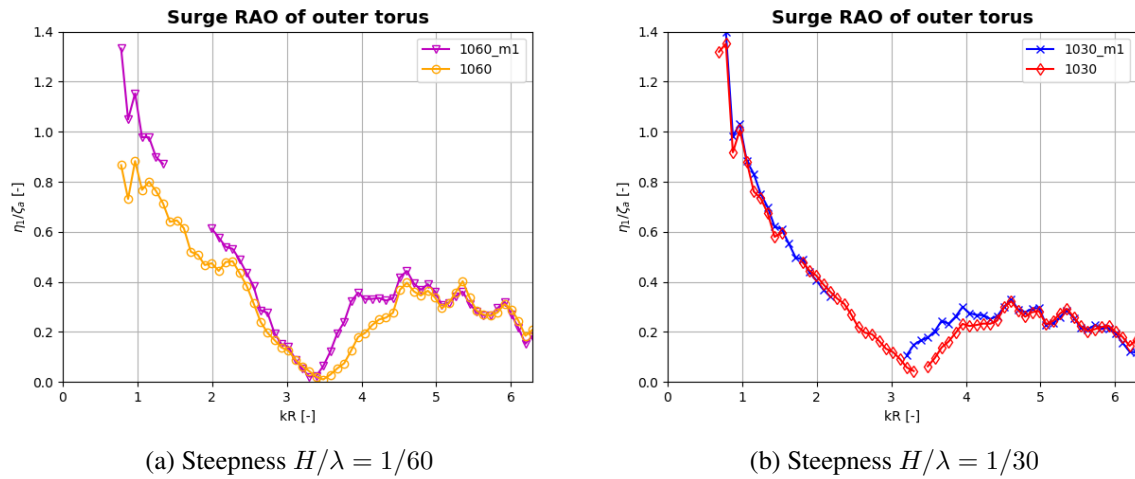
Figure 5.7: RAO for the outermost torus in surge (x-direction). Comparing model with and without membrane. $m1$ signifies the first membrane multi-torus model. 1060 and 1030 signify wave steepnesses $H/\lambda = 1/60$ and $H/\lambda = 1/30$ respectively.

The response amplitude operator in surge is shown in figure 5.7. A tendency of the curve approaching a resonance frequency as kR decreases is observed. An estimate of the natural period in surge is found from equation 5.1. M is the total mass of the model, a_{11} is the added mass in surge and k_m is the spring stiffness. The added mass in surge is estimated as half the mass of the model, whereas the spring stiffness in surge is approximated as the sum of the spring stiffness from two out of four mooring lines. The surge natural period in model scale is estimated to $T_{1n} = 2.39$s without membrane and $T_{1n} = 2.71$s with membrane. Using the deep water dispersion relation, natural periods calculated corresponds to kR = 0.70, and kR = 0.55 respectively. This confirms that the RAO in surge approaches resonant behaviour for the largest wave periods tested. The resonance behaviour around the same wave period is also found in the results of [Windsvold, 2018]. It is observed that the response of the model without membrane tested for waves with steepness $H/\lambda = 1/60$ does not increase as clearly towards a resonance peak that the other tests, but it is assumed that this is either caused by inaccuracies in the model tests or that the response in surge without membrane is dependent of the steepness of the waves. The first is the most likely cause. The first cancellation period is found for kR = 3.5 for the tests with wave steepness $H/\lambda = 1/60$ and for kR = 3.0-3.5 for the tests with wave steepness $H/\lambda = 1/30$.

Sway RAO of the outer torus is presented in figure 5.8. It shows that neither of the models moves significantly in the tangential direction of the waves and small responses are found in sway for the measured wave periods. This reinforces the assumption that sway is negligible in the numerical implementation model.
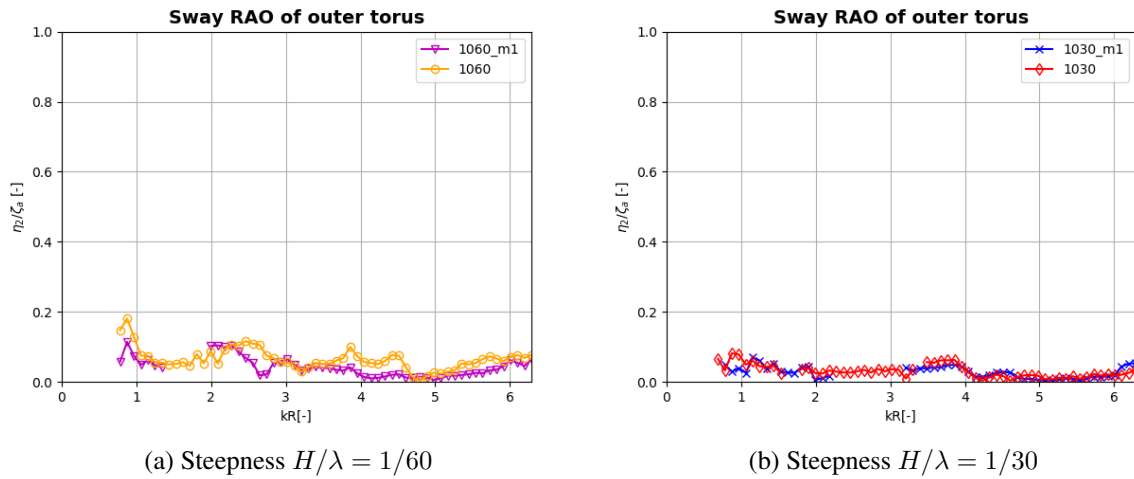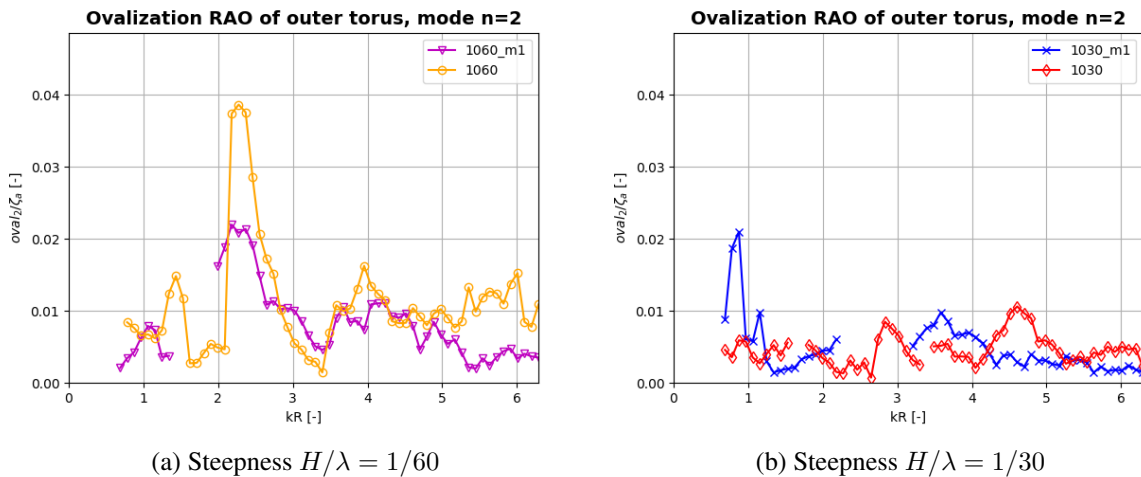
(a) Steepness $H/\lambda = 1/60$ (b) Steepness $H/\lambda = 1/30$

Figure 5.8: RAO for the outermost torus in sway (y-direction). Comparing model with and without membrane. $m1$ signifies the first membrane multi-torus model. 1060 and 1030 signify wave steepnesses $H/\lambda = 1/60$ and $H/\lambda = 1/30$ respectively.

Radial direction

In the radial direction, ovalization RAOs for 5 modes are calculated using the modal analysis described in 2.5.3. Remark that the mode 0 in the radial direction is unphysical, and therefore not included in the modal analysis steps. Mode 0 would represent that the tori displace radially, which is not possible as the tori are rigid and elasticity is limited in the radial direction. Mode 1 would represent surge and is therefore also excluded from the modal analysis. That means

(a) Steepness $H/\lambda = 1/60$ (b) Steepness $H/\lambda = 1/30$

Figure 5.9: RAO for the outermost torus in ovalization mode 1. Comparing model with and without membrane. $m1$ signifies the first membrane multi-torus model. 1060 and 1030 signify wave steepnesses $H/\lambda = 1/60$ and $H/\lambda = 1/30$ respectively.

(a) Snap shot　　　　　　　　　　　　　　(b) Snap shot
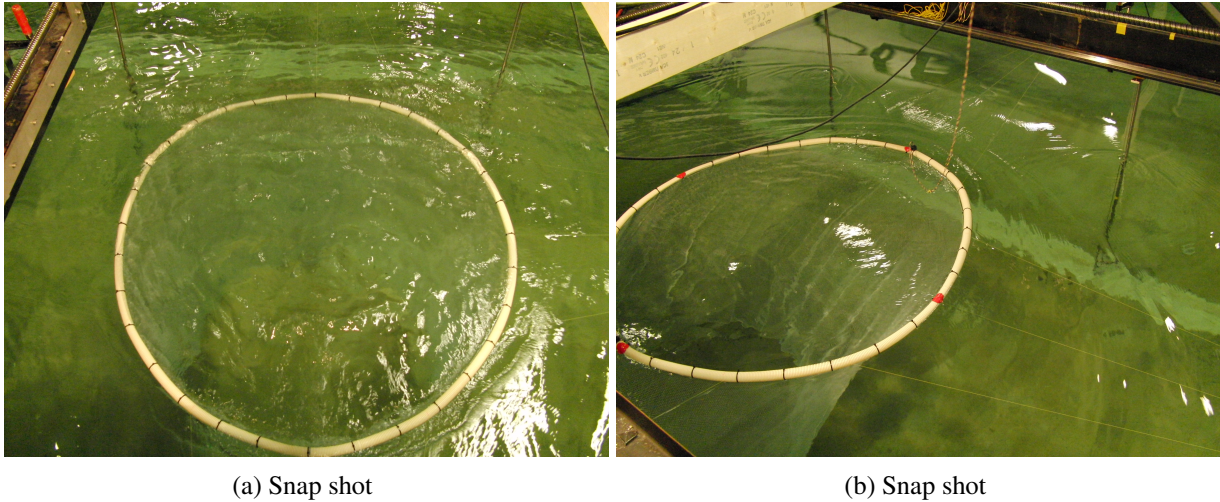
Figure 5.10: Fish farm collar of diameter 1.5 made of corrugated pipe with cross sectional diameter 32 mm. Tested in the MC laboratory in regular waves. Courtesy to [T. Kristiansen (unpublished), 2011]

n = 2 is the first ovalization mode. Figure 5.9 and F.5 show the RAO of the first and second ovalization mode for both wave steepnesses and both models tested.

The RAO of the first ovalization mode for wave steepness $H/\lambda = 1/60$ shows a possible resonance period for kR = 2.3. A smaller peak is present at the same wave period for the model with membrane, but the resonant behaviour is damped as an effect of the membrane. The same resonance peak is not present in either of the tests with wave steepness $H/\lambda = 1/30$. For the model with membrane, this can be explained by deleted tests around these wave periods, as a result of measuring errors in these tests. Since the difference of the response is so clear comparing the two steepnesses, the results should be further looked into, to make sure the resonance peak does not result from a set of false tests. This possibility has been investigated thoroughly, but no indication of a problem with these tests have been found.

It should also be mentioned that the eventual resonance peak present has low energy compared to the response in vertical modes. Neither the second ovalization mode or any of the higher ovalization modes have significant amounts of energy. This indicates that ovalization, in general, is very limited for both the model with and without membrane. Ovalizating behaviour has been indicated as a possible challenge for a floating solar island since the equipment installed would be affected by this. It is therefore beneficial for the equipment that the ovalization is limited. Figure 5.10 shows how large ovalizations can be problematic for single-torus models. The combination of multiple tori and interconnecting trusses is, therefore, a significant improvement of the model design when it comes to limiting ovalization.

5.1.4 Overtopping in regular waves

A systematic study by use of cameras recording the model exposed to a stationary part of all wave series has been conducted. This has resulted in a better understanding and documentation on where and when the overtopping occurs for the models tested. According to research by Prof. T. Kristiansen [personal communication, 2019], there is no indication of the overtopping phenomena being part of the linear behaviour of the model, which makes it impossible to describe by linear theory. It is therefore assumed that the overtopping phenomenons are induced by higher order motions induced by the waves.

No membrane

For the model tested without membrane, overtopping is only observed for wave steepness $H/\lambda = 1/40$ for full-scale wave periods higher than T_f =11.69s and wave steepness $H/\lambda = 1/30$ during wave periods higher than T_f =10.25s. The steepest waves tested had steepness $H/\lambda = 1/30$. This means the waves with steepness $H/\lambda = 1/60$ and $H/\lambda = 1/50$ did not lead to any overtopping behaviour. Observations of overtopping for wave steepness $H/\lambda = 1/30$, with wave periods T_f =10.89s and T_f =14.0s, are shown in figures 5.11 and 5.12.

This is an improvement from the tests conducted in November 2018, of which the results are further presented in Appendix C.2. In the November tests, overtopping aft on the model was observed already for waves with steepness $H/\lambda = 1/60$ and wave periods higher than T_f =9.25s full-scale. For steepness 1/30, overtopping was observed at the aft part of the model for full-scale wave periods higher than $T_f = 6.0$s. The mooring line set-up is the main change in the model test set-up. During November tests, the mooring line spring stiffness was 28.0 N/m, whereas the springs used in this case has a spring stiffness of 14.0 N/m. The mooring line pre-

(a) $H/\lambda = 1/30, T_f = 10.89s$ (b) $H/\lambda = 1/30 , T_f = 10.89s$

Figure 5.11: Snap shots from video of model without membrane exposed to waves with full-scale period T_f =10.89s. Wave steepness H/λ =1/30. Overtopping observed over the two outermost tori, at angular position 180°(aft). 0°being the point where the waves first hits the model.
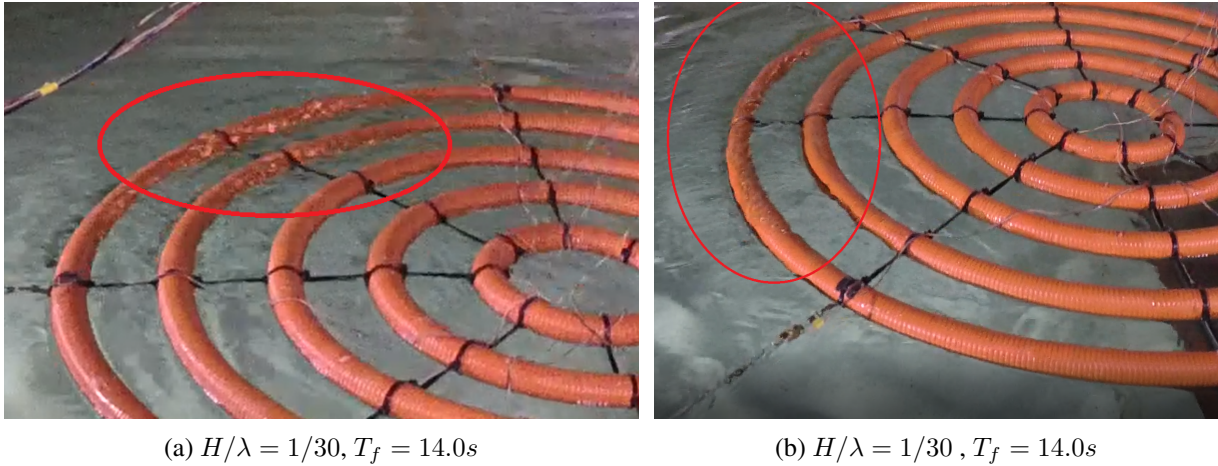
(a) $H/\lambda = 1/30$, $T_f = 14.0s$ (b) $H/\lambda = 1/30$, $T_f = 14.0s$

Figure 5.12: Snap shots from video of model without membrane exposed to waves with full-scale period T_f =14.0s. Wave steepness $H/\lambda = 1/30$. Overtopping observed over two outer tori, at angular position 180°(aft). 0°being the point where the waves first hits the model.

tension was also reduced from 5.0 N in November to 2.6 N in these tests. This indicates that the elastic behaviour of the model is strongly dependent on the mooring-line properties. It is also likely to believe that the reduction of the mooring line spring stiffness has given the model flexibility to better follow the waves.

In general, no overtopping was observed at the fore, where the waves first hit the model, for regular waves. It is observed that the overtopping occurrences are fewer for these tests than what was found during the tests of [Windsvold, 2018] with the old multi-torus model, where overtopping was documented for wave periods $T_f \geq$ 10.0s and wave steepnesses $H/\lambda \geq 1/40$ during these tests at the aft (180°) of the model.

Membrane set-up 1

In the first membrane set-up, the membrane was not as thoroughly tightened and stretched on the model as in case of the second membrane set-up. The membrane got wet and started sagging. That also means no longer pre-tensioned as desired. As the membrane was sagging, this made the air-gap smaller and overtopping occurred for shorter wave periods and lower wave steepnesses for this model than the second membrane set-up. Overtopping aft at the two outer tori occurred for full-scale wave periods higher than $T_f = 10.89s$ at wave steepness $H/\lambda = 1/40$ and for full-scale wave periods higher than $T_f = 7.96s$ at wave steepness $H/\lambda = 1/30$. The highest wave period tested was T_f =14.0 full-scale and aft is the opposite position of where the waves first hit the model. Snapshots showing overtopping behaviour can be found in figure 5.13 and 5.14. Further, a behaviour looking like slamming, induced by drag forces on the membrane, was also observed for the same wave periods. This has not been further investigated, but it would be interesting to measure the force working on the membrane during these occurrences.
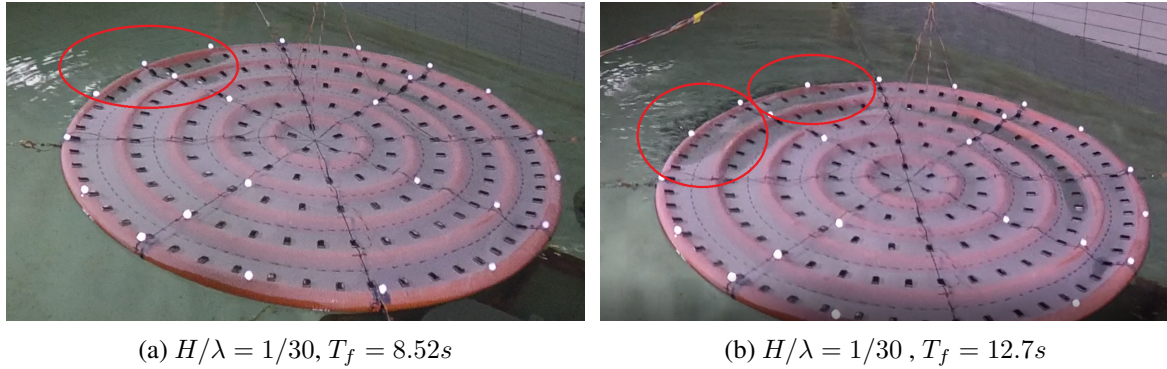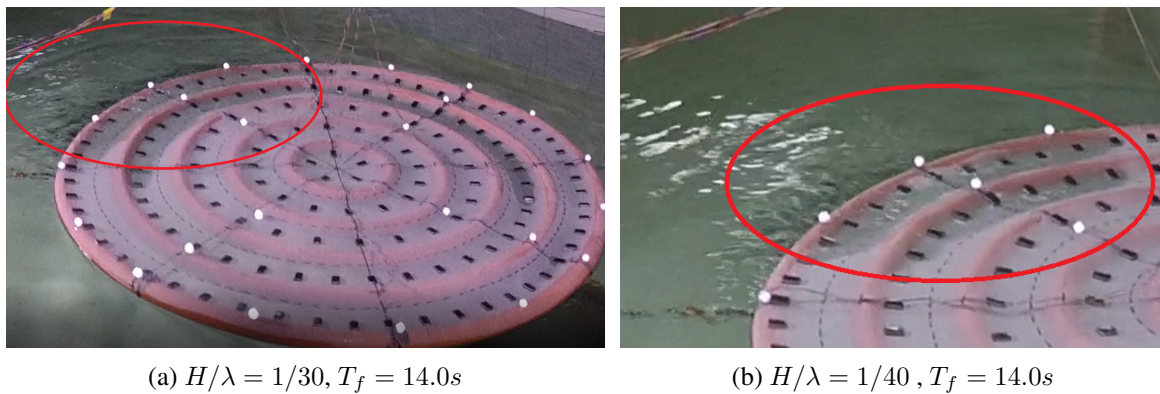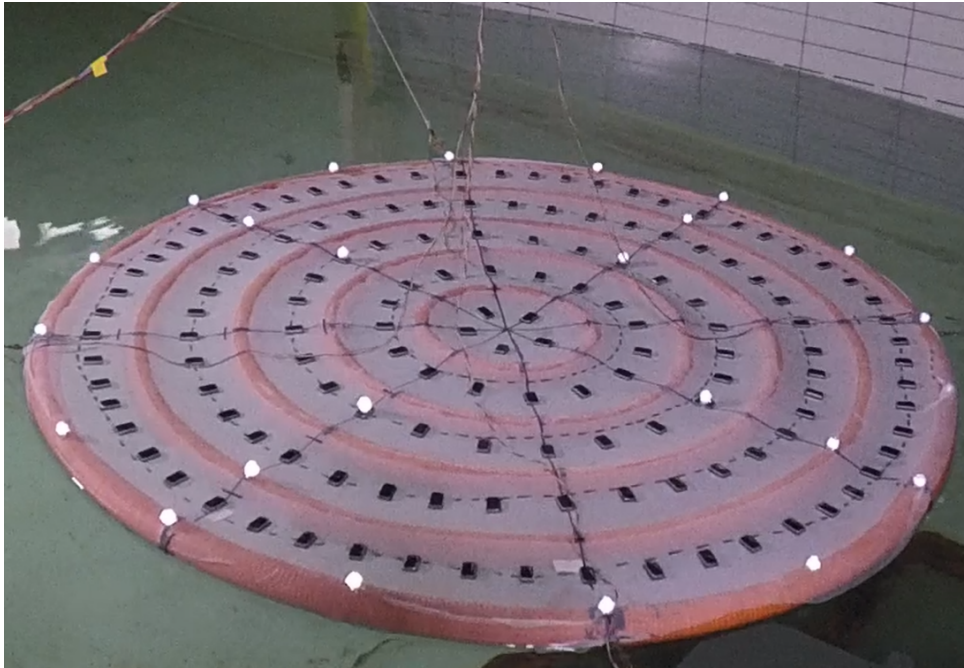
(a) $H/\lambda = 1/30, T_f = 8.52s$ (b) $H/\lambda = 1/30, T_f = 12.7s$

Figure 5.13: Snap shots from video of model with membrane exposed to waves with full-scale period T_f =8.52s and T_f =12.7s respectively. Wave steepness $H/\lambda = 1/30$. In figure (a), the membrane starts to get soaked and overtopping on outer torus is observed at 180°. In figure (b), overtopping on the two outer tori is observed at 180°(aft). This point is the angular position opposite of the point where the waves first hit the model.

(a) $H/\lambda = 1/30, T_f = 14.0s$ (b) $H/\lambda = 1/40, T_f = 14.0s$

Figure 5.14: Snapshots from video of model with membrane exposed to waves with full-scale period T_f =14.0s and wave steepnesses $H/\lambda = 1/30$ and $H/\lambda = 1/40$ respectively. Overtopping on the two outer tori is observed around angular position 180°(aft), which is opposite of the point where the waves first hit the model.

Membrane set-up 2

As the new membrane was installed, new wave tests of the regular wave series with wave steepness $H/\lambda = 1/60$ and $H/\lambda = 1/30$ were conducted. It can be seen in figure 5.15, where the model is exposed to regular waves with steepness $H/\lambda = 1/60$ and full-scale wave period $T_f = 7.72s$, that the membrane is more pre-tensioned when attached to the tori than in case of the first set-up. This had a positive effect on the overtopping occurrences. In this case, overtopping was only observed aft on the two outer tori for tests with steepness $H/\lambda = 1/30$ and all wave periods higher than $T_f = 7.96s$. That means almost no difference in overtopping behaviour between the model with and without membrane is documented.

Figure 5.15: Snap shots from video of model with membrane exposed to waves with full-scale period $T_f = 7.72s$ and wave steepness $H/\lambda = 1/60$. No overtopping observed for any of the waves tested with steepness $H/\lambda = 1/60$.

(a) $H/\lambda = 1/30, T_f = 12.7s$

(b) $H/\lambda = 1/30 , T_f = 12.7s$

Figure 5.16: Snap shots from video of model with membrane exposed to waves with full scale period $T_f = 12.7$s and wave steepness $H/\lambda = 1/30$. Overtopping is observed on the two outer tori at angular position 180°(aft), when 0°is the position where the wave hits first. It is also observed for wave periods $T_f = 10.89$-14.0s for the same wave steepness.

5.2 Experimental results - irregular waves

In this section, experimental results from tests with irregular waves will be presented and commented. The significant wave height and the spectral peak period have been used as varying input parameters to represent different sea states. First, some examples of measured wave and response spectra are illustrated. Then, the vertical RAOs of the outermost torus will be presented. Further results can be found in Appendix F.2. It should be noted that the first membrane (m1) collapsed during the irregular wave tests. This started already on the fourth sea state of test matrix 2006 and became worse throughout tests 2008, 2010 and 2012. A new membrane (m2) was set up on the model in order to make new measurements of irregular waves with membrane, but unfortunately, the Qualisys measurements from these tests suffered from measurement errors and are therefore not presented. The largest sea state of all test matrices with membrane 1, that were run during the collapse, were also lost due to measuring errors as a cause of the Qualisys system falling out.

5.2.1 Measured wave spectra

The measurements done by WP1, the wave probe that is expected to be least affected by wave radiation and disturbances from the model, is used to make the wave spectra presented in this section. Wave spectra with the same spectral peak period T_p are presented together. It is expected that the area under the curve increases for increasing significant wave height H_s. As the spectral peak period rests the same for varying significant wave height, it is expected that the maximum amplitude peak of the spectrum rests at the same wave frequency.

(a) No membrane
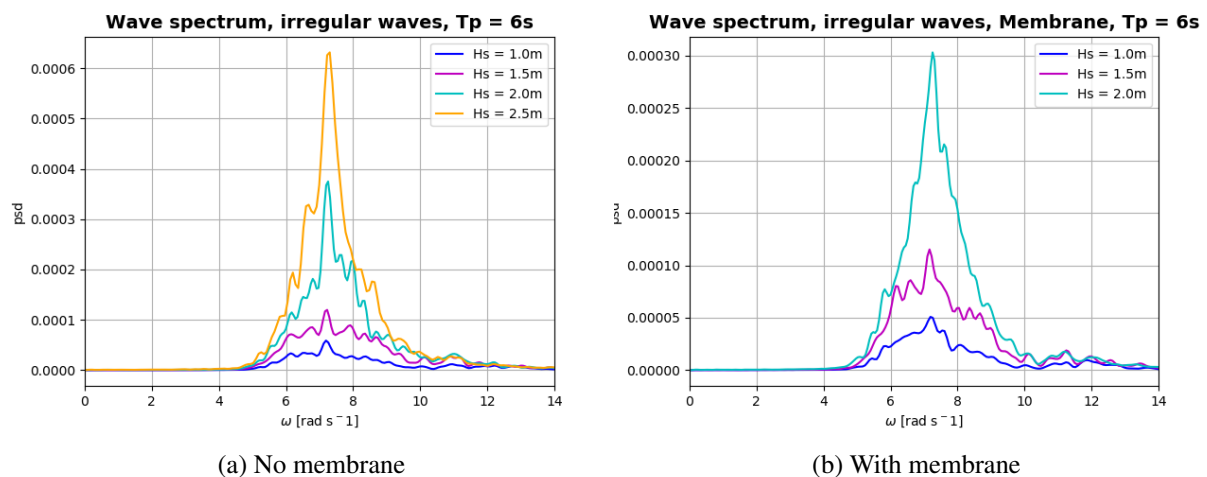
(b) With membrane

Figure 5.17: The wave spectra from the tests with $T_p = 6$s and $H_s = 1.0$m, 1.5m, 2.0m and 2.5m are presented for the models with and without membrane. The largest H_s test with membrane suffered from measuring errors due to the Qualisys system falling out, and is therefore excluded from the results. Remark that the two vertical axis do not keep the same scale.
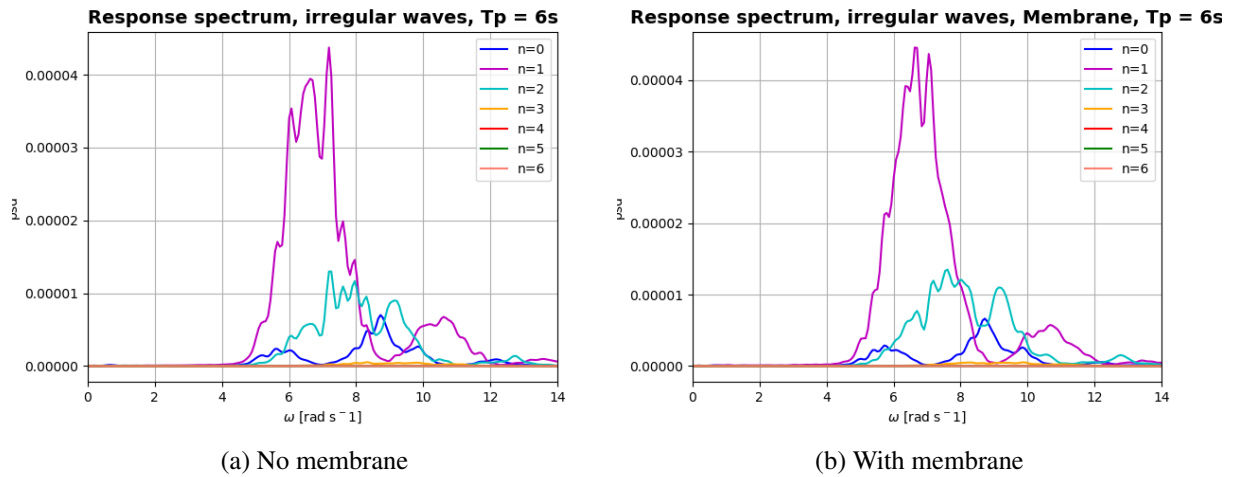
(a) No membrane

(b) With membrane

Figure 5.18: Modal response spectra for mode 0-6 from irregular wave tests with T_p = 6s and H_s = 1.0m are presented in the figure for the model with and without membrane. It is seen that the pitch response is dominating, while the first flexible and heave response are the two other main contributors. The other modes have small responses compared to these three.

Figure 5.17 shows the wave spectra for T_p = 6s and H_s = 1.0m, 1.5m, 2.0m and 2.5m for the model with and without membrane. As the Qualisys system fell out during the highest H_s for the model with membrane, these results are excluded from the graph. Both graphs show increasing max amplitude for increasing significant wave height and the maximum amplitude keeps at the same wave frequency for all plots. The spectra could have been plotted against the JONSWAP spectrum for the corresponding input parameters for better verification of the results. Further wave spectra are presented in Appendix F.2.1.

5.2.2 Response spectra

The response spectra for mode 0-6 from tests with T_p = 6s and H_s = 1.0m and 2.0m are presented in figure 5.18 and 5.19 respectively. These have been obtained through spectral analysis of the modal responses, found through modal analysis of the time series of the 16 markers positioned on the outer torus. Both figures show that the pitch response is dominating for the sea states presented. Heave and 1st flexible curves also show that the model is affected by these motions, while the higher mode responses are small compared to these. The response spectra for the remaining tests can be found in Appendix F.2.2

5.2.3 Vertical RAOs of outermost torus

The vertical response amplitude operators of the outermost torus from irregular waves are presented in this section. They are obtained by the method described in section 4.6.2. The vertical RAOs for irregular waves will be compared to the results from regular waves. The results are presented by plots where the transfer function is plotted against the wave numbers
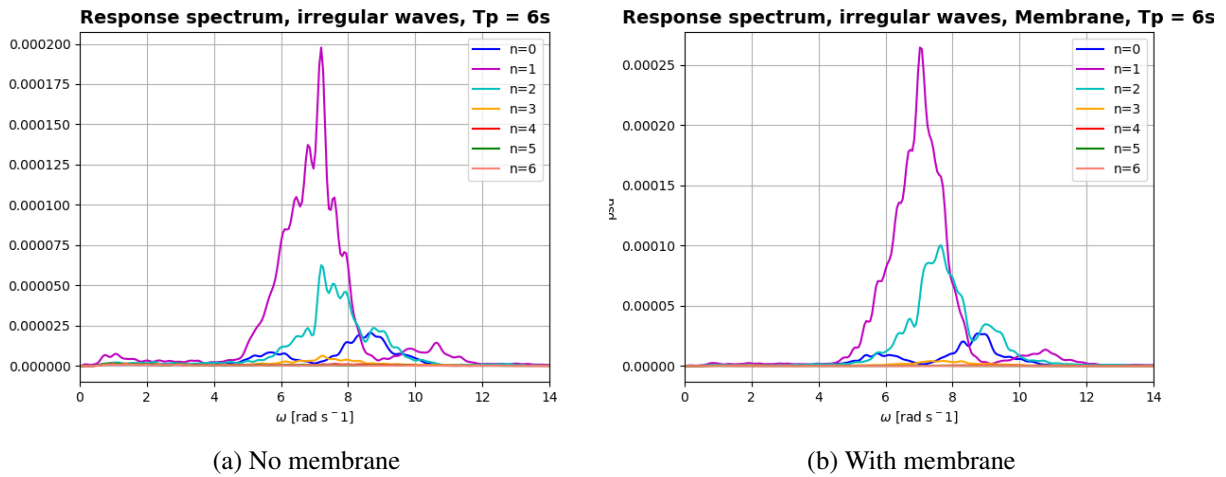
(a) No membrane

(b) With membrane

Figure 5.19: Modal response spectra for mode 0-6 from irregular wave tests with $T_p = 6$s and $H_s = 2.0$m are presented in the figure for the model with and without membrane. It is seen that the pitch response is dominating, while the first flexible and heave response are the two other main contributors. The other modes have small responses compared to these three. Remark that the two vertical axis do not keep the same scale.

times the radius of the outer torus, kR. Some illustrative findings are presented below, while the remaining results are presented in Appendix F.2.3 - F.2.6.

Heave

The response amplitude operators in heave of $T_p = 6.0$s and $H_s = 1.0$m, 1.5m, 2.0m and 2.5m are plotted in figure 5.20, for the model tested with and without membrane. Theoretical RAO from zero-frequency theory for a single torus is also plotted for comparison. As for regular waves, the measured response follows well the theoretical curve until kR = 2.4. The measured response also continues to follow the ZFT well until about kR = 3.5. For increasing kR, the phase shift also commented in the regular wave results becomes more present. For $\omega \geq 10.0$ rad/s, there is no energy present in the wave spectra corresponding to this RAO. These wave frequencies correspond to kR ≥ 5.1. This indicates that the response in the RAO present for wave numbers higher than kR = 5.1 is coming from higher order effects, and should therefore not be present in an RAO ideally. Since it is complicated to filter out higher order effects in irregular waves, these are left in the RAO, but the results for kR ≥ 5.1 cannot be compared to the regular wave RAOs. The increase in response for kR = 4.0-6.0 in the tests with membrane indicates that the higher order effects are increased as an effect of the membrane. But this should be further investigated, as noise from the measurements and the post-processing can also be part of this. It should also be kept in mind that RAO and spectra are largely dependent on the smoothing parameters used in the post-processing. The same effects as mentioned for spectral peak period $T_p = 6.0$s are found for the higher peak periods tested.
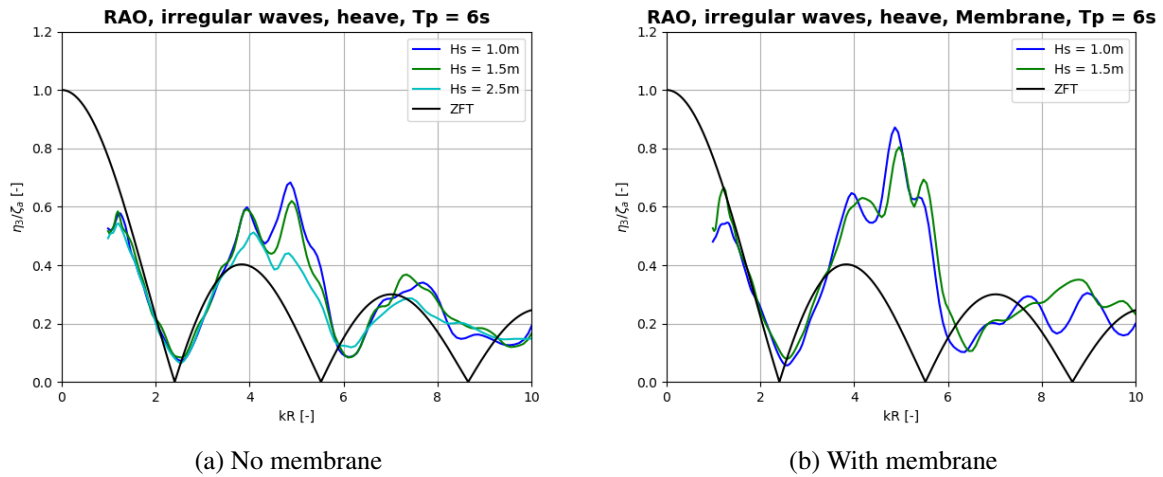
(a) No membrane

(b) With membrane

Figure 5.20: The heave irregular RAO for tests with T_p = 6s and H_s = 1.0m, 1.5m, 2.0m and 2.5m are presented in this figure, both for the model with and without membrane. The largest H_s test with membrane suffered from measuring errors due to the Qualisys system falling out, and is therefore excluded from the results.

In general, the regular and irregular wave RAOs in heave show the same trends. Both RAOs show that the first and second cancelling periods are present at kR = 2.4 and kR = 6.0 respectively. In addition to this, the curves correspond well for kR = 1.0-2.4. For higher kR, the two RAOs show the same trends, but the irregular wave RAOs suffer from larger amounts of energy, which is probably caused by higher order effects as mentioned.

Pitch

In figure 5.21, the pitch RAO for tests with T_p = 6.0s and H_s = 1.0m, 1.5m, 2.0m and 2.5m are presented. The measured pitch RAO for all wave heights follows the ZFT well at kR = 1.0-3.0. Further, the same earlier mentioned phase shift is also present in this case. As for the heave RAO, there is a max amplitude peak around kR = 5.5 that is higher in the measurements than in theory. The shape also changes for kR > 4.0, equally as in the measured RAO in regular waves. Comparing the regular pitch RAOs with the irregular, it does not show the same increase in response for kR $\geq$ 4.0, which indicates that this increase is caused by higher order effects. The results show the same trend and both follow the ZFT well for kR $\leq$ 4.0.

1$^{\text{st}}$ and 2$^{\text{nd}}$ flexible

In the case of the first flexible RAO, the response is significantly higher for the model with membrane, especially around the maximum response amplitude at kR = 5.0. Even though, the trend of the curve in both cases show the same variations depending on wave period. The trend also coincides with the trend of the regular wave RAOs. When it comes to the second flexible vertical RAO, the same statements as mentioned for the first flexible are true. The maximum
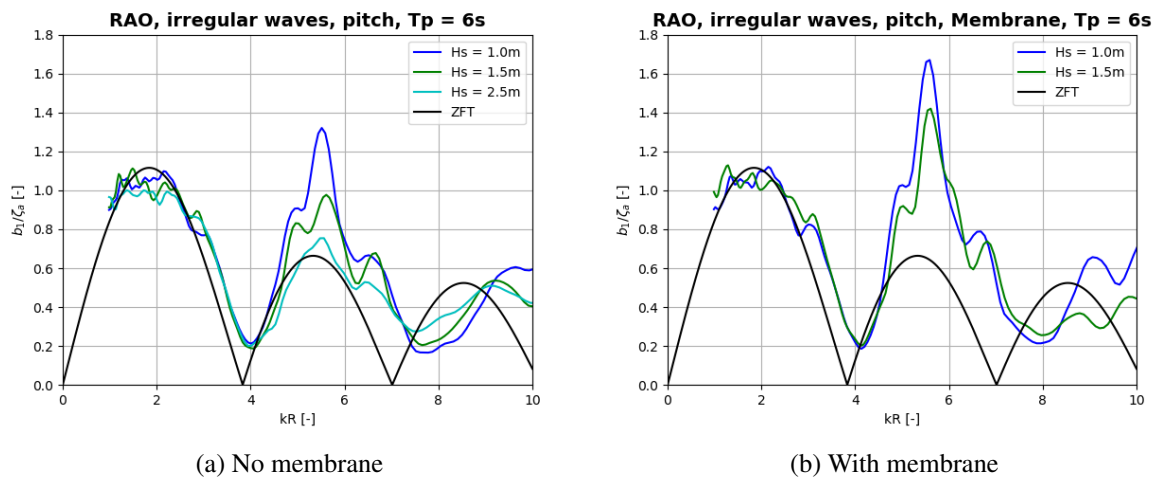
(a) No membrane

(b) With membrane

Figure 5.21: The pitch irregular RAO for tests with T_p = 6s and H_s = 1.0m, 1.5m, 2.0m and 2.5m are presented in this figure, both for the model with and without membrane. The largest H_s test with membrane suffered from measuring errors due to the Qualisys system falling out, and is therefore excluded from the results.

response amplitude occurs around the same wave period. The regular and irregular RAOs for the first flexible are corresponding well. When it comes to the second flexible, the irregular wave RAOs have higher response amplitudes than for regular waves. This can be caused by noise in the signal. Plots corresponding to the first and second flexible RAOs are found in Appendix F.2.5.

5.3 Discussion on challenges with Qualisys

There were two main reasons for the unusable data collected during the model tests. First, an error of sampling frequency in the input wave files. The sampling frequency used to make the tests files did not match the one of the wavemaker. This was corrected early and new input files were made. Secondly, a repeating error with the Qualisys system made OQUS camera 2 to lose connection with the measurement system. This problem was not solved all along the test period and complicated the post-processing. All time series had to be checked thoroughly for missing or deceptive data. With 24 markers tracking the motions of the model in 3 directions, this was quite time-consuming. Most probably, an error in the Qualisys program package or an error in the installation of the system was the reason for one of the OQUS cameras loosing connection. Some of the test matrices had to be repeated their completeness, under constant surveillance, to make sure the Qualisys system did not lose connection. Qualisys is a very precise and good tool to track the motions of a system, but the problems discussed here have been time-consuming and increased the complexity of the post-processing. The results may also include false responses as a consequence of measurement errors which have not been caught up and suppressed.

From time to time the cameras lost track of some of the markers. The position of the cameras led to some of the markers getting lost during exposure to large waves. This could have been improved by installing the cameras higher up towards the ceiling and more concentrated towards the part of the towing tank where it is interesting to use the system. As the wave probes were installed into the basin attached to metal beams lying on top of the side walls of the basin, these also contributed to giving the cameras less visibility. This almost set camera 1 and 4 out of play completely due to poor visibility. See figure 4.4 for the set-up of the model tests, including the positions of the cameras.

As the cameras started to lose track of a marker, it was observed that the system had problems recapturing the position and this disturbed the system such that the number of markers with lost track increased rapidly. This made it necessary to restart the system manually. When a restart was completed, tests with the same magnitude of waves could be run without trouble. It was, therefore, difficult to find the reason why the problem occurred in the first place and this made it necessary to keep the system under surveillance to avoid these types of errors. A lot of time was lost while trying to find solutions to the problems with the system. Results from wave steepnesses $H/\lambda = 1/50$ and $H/\lambda = 1/40$ were not given priority to post-process, as a lot of data is missing from these tests and there was not enough time to repeat all wave matrices with both the model with and without membrane.

5.4 Discussion on multi-torus model

The multi-torus model is built from taped corrugated tubes, hair elastics, polyester material and 5g weights. It can be discussed whether all components give a realistic picture of a full-scale solar island with deck. Scaling the parameters of the model up to full-scale gives an indication of whether the properties of the materials used are realistic. Symmetric design is an important factor and the model is not made with enough precision to assure that the trusses and mooring lines are attached at the exact correct angular positions. Neither are the weights on the membrane. Installation of the membrane on the multi-torus was done by hand and some inaccuracy and dissymmetry, therefore, have to be accounted for.

It can also be discussed whether the weighted membrane set-up made a realistic representation of the deck with solar panels. The weights were scaled in order to correctly represent a realistic weight of a solar panel deck in model scale. A polyester net with small meshes and equal elasticity in two transverse directions was used. Testing to find the stiffness coefficients of the material would have made it possible to scale and compare with possibilities of full-scale materials suitable to be used as a deck.

5.5 Discussion on error sources in experiments

Error sources in experiments are usually divided into bias errors and precision errors [Steen, 2014]. The first are systematic errors, that can not be limited by repeated tests. Precision errors are random errors that can be found and decreased through repeated testing. The test

matrix named 3000 was made in order to repeat the tests 5 times and make an uncertainty analysis of the model tests. This has not been completed due to lack of time. Repetition tests could have quantified the uncertainties regarding precision errors on the model tests. Since these have not been analysed, it is important to keep in mind that the results are not exact and the uncertainty is unknown. That said, since the results have been compared to the multi-torus model tests by [Windsvold, 2018], this gives an indication of the relevance of the test results.

There is some uncertainty concerning the accuracy of the force rings, as drifting was a problem during the model tests. The force rings were calibrated before the set-up was installed and zero settings were conducted before each test matrix was started, to limit the problem. During a test matrix of 4 hours, the mooring force time series show drifting of the mean. By running shorter test matrices, the drifting was limited. Using a high-pass filter on the complete time series in the post-processing also filtered out the low frequencies caused by the drifting.

Concerning the multi-torus model, it is not perfectly circular and symmetric. In the post-processing, angular positions of the mooring lines and Qualisys marker's have been used, but these are deviating from the exact position in the model. This potentially produces a small bias error source but is difficult to quantify. Approaches used to find the mooring line spring stiffness, truss spring stiffness and bending stiffness of the torus are simplistic and resulting in approximated values. The precision of the Qualisys system can also be discussed. The system is assumed to be rather accurate, but there are indications of precision being dependent on the positions and distances of the cameras. As mentioned before, the first membrane set-up (m1) collapsed after a few days of use. The reason was the material was not enough or symmetrically stretched, which caused the membrane to get soaked. As it got soaked, it expanded and lost its pre-tension. This is not desired as the pre-tension prevents snap loads. The glue used to fix the weights onto the membrane and the membrane onto the torus also contributed to the collapse, as it was not optimal for use in water.

Measured wave amplitudes show that the inaccuracy of the waves induced by the wave maker increases for lower wave periods. The waves made by the wavemaker are thus deviating from the input parameters. There is also a leakage in the wavemaker, that makes water leak out to the area behind the wave maker. A pump is installed to transport the leaking water into the basin again. This means the water level in the basin is not constant or exactly equal to 0.7m. The waiting time between wave series is set to 180s for regular waves and 240s for irregular waves. This gives time for the water surface to calm down, but it will not be completely calm before the next wave series start. Since larger waves make more movement in the water, the water surface will be less calm for increasing wave periods as the wave steepness stays constant in a test matrix.

5.6 Numerical results

In this section, the results of the numerical simulations will be presented and commented. The implementation is presented in detail in chapter 3 First, the verification studies conducted on the truss model will be verified towards relevant theory. Then, the results of the implementation of the coupled truss and floater model will be presented. As mentioned before, there is a bug in the code making these results unphysical and therefore not representable for the model. This also makes it impossible to compare the results with the experiment.

5.6.1 Verification studies

As mentioned before, several simple verification studies have been conducted in order to make sure of the functioning of the truss model. Among these a suspended wire, a simple pendulum, a double pendulum and a compound pendulum. All pendulum models have been tested both with and without elasticity. Details about the verification studies can be found in Appendix D.1. Numerical examples and analytical solutions of the cases are presented in the same Appendix. Further numerical results from the verification studies are included in Appendix E.1.

The resulting behaviour of the suspended wire is a vibrating string, as shown in figure E.1, in Appendix E.1. As only gravity forces are included in the model, the internal tensions are working against the gravity forces and making an unstable system which constantly vibrates. When it comes to the simple rigid pendulum, the vertical tip displacement is equal to the analytical solution presented symmetrically oscillating around the vertical axis for initial angles less than 90°. For the case of a larger initial angle, the vertical motion is no longer symmetric, but the motion of the pendulum mass is still symmetric. This is seen in figure E.2 in the Appendix. The solution is converging for the smallest time step tested, which is 10^{-4} s. This is seen by plotting the change in length of the truss, which is supposed to be constant.

Both the double rigid pendulum and the double compound pendulum has a characteristic increasing chaotic behaviour as the initial position angle increases. This is complicated to represent analytically, but a numerical example of this is presented in Appendix D.1. The resulting behaviour of the double compound pendulum is presented in figure E.3 in the Appendix. This shows conformity to the expected behaviour.

Compound flexible pendulum

Finally, the compound flexible pendulum solution has been compared to the results of a numerical case by [Marino et al., 2019]. The numerical solution by [Marino et al., 2019] is presented in figure 3.3. The results are corresponding well, taking into account that there is no bending stiffness in the truss model. Since the lumped mass principle is applied, there is half as much mass in the end node as the others and this makes it easily rotate around its own centre of rotation, in addition to the lack of bending stiffness. Figure 5.22 shows the position of the pendulum in the first second of the simulation. It is seen that increasing the number of
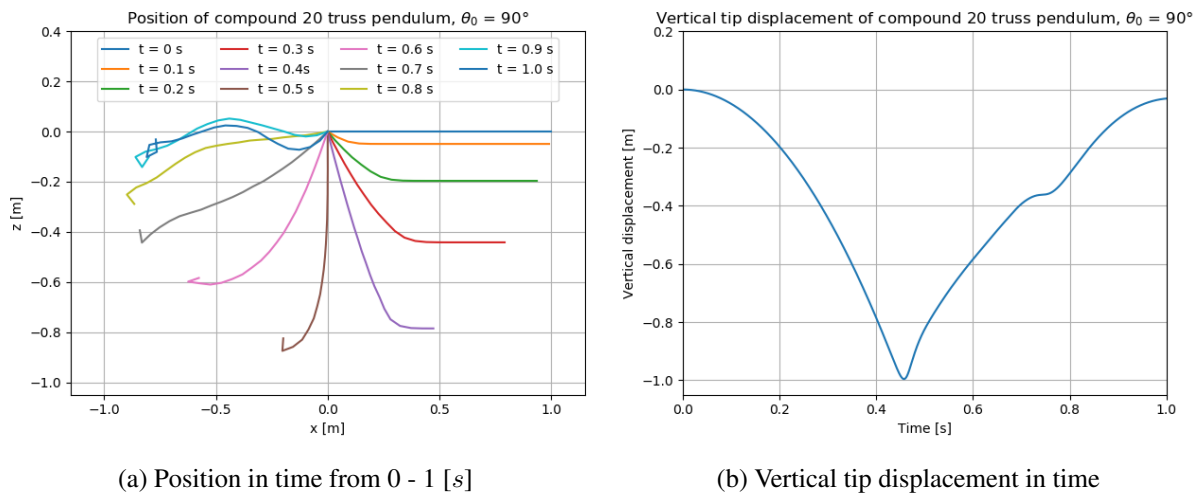
(a) Position in time from 0 - 1 [s]

(b) Vertical tip displacement in time

Figure 5.22: Compound flexible pendulum with uniformly distributed mass during first second of simulation. Initial position $\theta_0 = 90°$. Simulation using 20 truss elements.

trusses in the simulation makes the deformation more realistic during the first increments, but it rapidly becomes a problem that there is no bending stiffness included. Comparing the plots of the vertical tip displacement in figure 5.22 to the model by [Marino et al., 2019] in figure 3.3, the results corresponds until approximately 0.8 [s], where the rotative movement of the end node affects the vertical position. This problem is less present as the number of trusses is reduced, as shown in figure E.4 in the Appendix, but the general motion of the complete model is less well represented in this case. The model reminds of a hanging rope, which is correct realistic behaviour of a compound flexible pendulum with lack of bending stiffness.

5.6.2 Single torus coupled with mooring line trusses

The results of the numerical model that includes a single torus coupled with mooring line trusses are presented in this section. Details about the implementation of the model can be found in section 3.7 and Appendix D.2. As mentioned above, there is a bug in the Python script which makes the results non-physical and incorrect. At the initial time step, the models' position is equal to the position of the experimental multi-torus model. As the simulation of the model starts, the horizontal coordinates of the model start expanding, making it look like the model "explodes". This explosion of the coordinates is shown in figure 5.23. It should be remarked that only vertical forces are accounted for in the model, but this is not assumed to cause problems. This means the code will not show a complete picture of how the model behaves in reality. Sway is assumed to be negligible, but surge should be accounted for to get a more realistic behaviour.

As the horizontal coordinates explode and the solution is unstable, a hypothesis of an error in the implementation of the change in coordinates was made. The model was changed in order for the horizontal coordinates to be kept at their initial position and only the vertical coordinates were allowed to change. This avoided an explosion but is obviously not a correct solution and
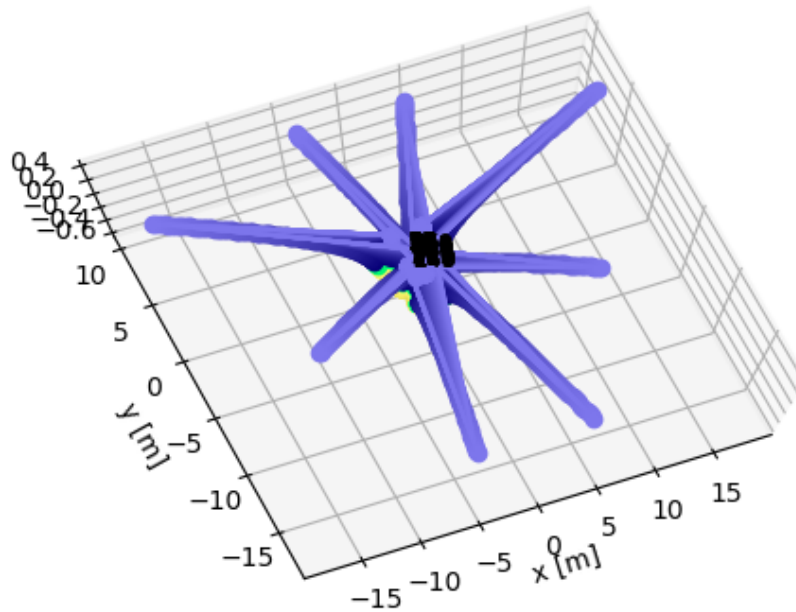
Figure 5.23: Illustration of explosion for coupled floater-truss model when including change in horizontal coordinates. Unphysical solution with horizontal coordinates multiplied 10 times.

several other problems were noted. Using the changed model, a new simulation was carried out. A wave with the same scale as in the experiments is included to induce wave response. As the simulation is initialized, the model starts to move slowly. First, the z-position of the floater nodes increases slowly. From this, negative tension forces start to occur in the nodes positioned at the middle of the mooring lines. This means the mooring lines are not tensioned any more, which makes the lack of bending stiffness obvious. Already here, the solution is suspicious as it is expected that the pre-tension in the mooring lines is large enough for the mooring lines to keep a positive tension throughout the simulation. Then, the model starts sinking and it sinks to unrealistic vertical values which in reality means the model would be submerged. Further, the solution stabilizes and starts oscillating around approximately -0.7m depth. This complete simulation is illustrated by figure 5.24.

Numerous trials have been done to try to find the error in the code, but none have been fruitful so far. Among many, the complete implementation of the floater model to the floater trusses has been examined from errors in terms of signs or missing expressions, the time step has been reduced several times to look at whether the stability of the solution could be a problem, etc.

5.6.3 Two tori connected with trusses

The implementation of the two-tori model, interconnected with trusses and attached by mooring lines has been geometrically adapted for in the code to make it possible to simulate. This made it necessary to adapt for different kind of trusses in the script, that could have floaters connected at both ends. The pre-tension of these trusses is not as simple to correctly represent as the mooring-line pre-tensions, but a constant was assumed based on the stiffness calculated in the experiment.

As the single torus model attached with mooring-lines did not work, a great effort to develop the code for all changes that are necessary to account for the double-floater trusses have not been made. The theory is exactly the same as the one developed for the single torus, just including a case where trusses can have floater nodes in both ends is necessary.

5.7 Discussion of error sources in numerical implementation

There are several possible error sources in the implementation. It is suspected that the error is a bug in the code, from either a wrong sign in the implementation of forces, an error of coding etc. There are some indications of error sources among the simulation results. As the truss model has been tested through numerous verification studies, it is likely to believe that the error lies in the implementation and coupling with the floater model.

First of all, the mooring lines are expected to keep positive tension throughout the simulation. As the tension forces at some point are negative, this indicates that there might be an error in sign in the implementation of the forces. Further, the sinking of the model could also be an indication of some error in signs of the forces included. As mentioned during the description of the implementation, tension forces are allowed to be negative, as this is theoretically correct for trusses. In reality, trusses will not take compression and instead act like a hanging rope attached between two points.

Further, the explosion can indicate some kind of instability in the solution. A too large time step could make the solution unstable, but this possibility has already been investigated to a certain extent. The unrealistic behaviour in the vertical direction of the floater nodes mentioned can also be an indication of an error in the solution of the equation of motion for the floater of some kind. This possibility has not been investigated enough.

5.8   Discussion of numerical methods used

It is expected that the coupled model would better represent the response of the model than what the simple single-torus ZFT does, as the presence of mooring lines and eventually another torus would have affected the solution. Especially the effect of the other torus, positioned inside the single torus and connected with trusses, probably would have made it possible to better explain the deviation in behaviour for $kR \geq 4.0$. The reason is that it is assumed that the tori are positioned close enough to radiate waves that will affect the others. This assumption is based on comparing the floaters to the two connected floating fish farm collars discussed in [Faltinsen, 2010]. As the distance between the collars is less than a given value dependent of the diameter and the cross-sectional diameter of the tori, it is assumed that the presence of more than one torus will affect the others. In addition to this, the tori will in this study have interacting forces as they are interconnected with pre-tensioned trusses.

In a complicated numerical model like this, the implementation is full of pitfalls and it is therefore not surprising that unresolved errors like this might take time to resolve. From a post perspective, bugs on the measurement devices during the model tests in addition to the complexity of the post-processing have taken more time than planned. It would have been favourable to use more time on the development of the numerical simulation model, due to the advance in theoretical complexity compared to previous studies. As mentioned before, approximately 35 % of the time available during the thesis has been used on the implementation of the numerical model. This has unfortunately not been sufficient, and the final goal of comparing the numerical solution with the experimental results have not been reached.
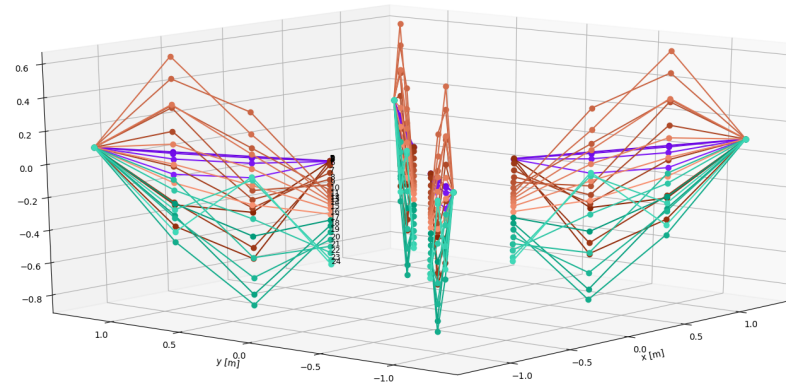
(a) Mooring truss nodes moving in time during the first second of the simulation, only accounting for changes in the vertical direction. It is observed that the mooring line is not positively tensioned anymore as time passes and more elastic than what is realistic. Vertical motions are also unrealistically large. The increasing numbers show how the floater sinks as the simulation goes on.
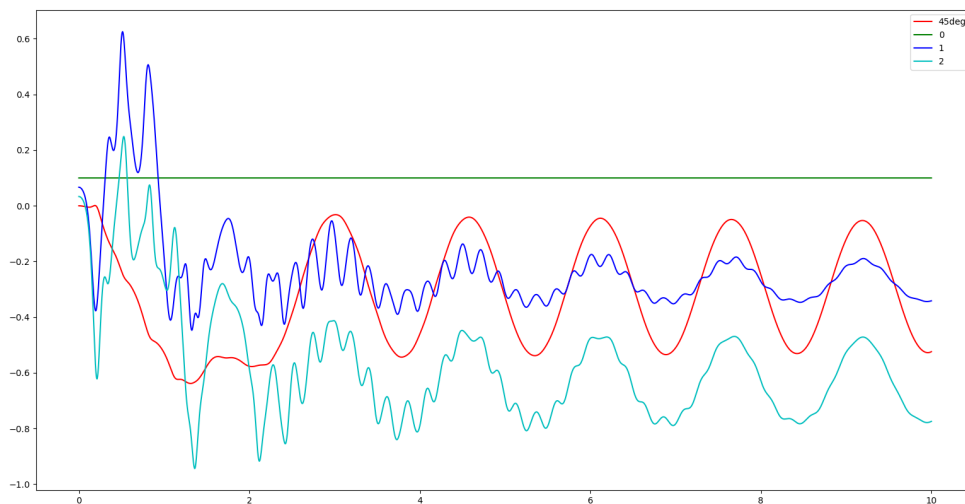
(b) Mooring truss nodes at 45° moving in time. 45°(red) is the floater truss at 45°, 0 (green) is the fixed node, 1 (blue) is the node the closest to the fixed node, 2 (cyan) is the node the closest to the floater node (45°). It is seen that the nodes' motions are stabilizing according to regular wave motions, but the moorings are not tensioned and the oscillations are unrealistically elevated compared to the wave applied with wave height 0.08m.

Figure 5.24: Mooring truss nodes movements in time for a simulation of 10s, when only z-coordinates are updated.

Chapter 6

Concluding Remarks and Further Work

Small scale model tests with a multi-torus with and without membrane are conducted to investigate the hydro-elastic responses of the model in regular and irregular waves. A coupled truss and floater model is numerically implemented in Python by using numerical time integration schemes to simulate the response in time. Design of a floating solar island should be such that it is suited for wave conditions relevant for adequate open water locations. The behaviour of the multi-torus in the wave conditions tested looks promising. The model follows the waves well and the tests with membrane do not change the responses in any significant matter. Ovalization response of the multi torus is limited, which is beneficial for the equipment on the solar panel deck. This is an improvement when comparing with a single torus model exposed to the same wave conditions.

Qualisys motion capture system is a good and precise tool and an unlimited number of markers can be installed on the model. Unfortunately, the system complicated the model tests, causing missing data for several wave conditions and need for repeating complete test matrices. More optimal positions of the OQUS cameras, as well as troubleshooting to find the cause of camera 2 losing connection is necessary to ease the use of the system.

The documentation of model behaviour through videos show that overtopping aft of the two outer tori is the main observed effect. Amount of overtopping has significantly reduced by reduction of mooring line spring stiffness and mooring line pre-tension, comparing the results to the observation tests conducted in November 2018. This indicates that the overtopping aft of the model is strongly dependent on the mooring line properties. Further studies concerning these parameters would be interesting, as the forces acting on the floater and membrane during overtopping are unknown. Overtopping aft increases slightly as an effect of the membrane. This means the overtopping occurs for slightly lower wave periods and wave steepnesses with membrane. Slamming-like wave motion on the membrane is observed in combination with overtopping for the largest waves tested. This is most probably caused by drag forces on the membrane as the water passes through the meshes and should be further looked into as slamming can be a major issue for the equipment on deck.

The numerical implementation of the truss model is shown to be successful, through the verification studies. Unfortunately, the coupling of the floater model with the already implemented truss model resulted in a bug in the Python script which has not been resolved. The bug causes the results to be non-physical and the model coordinates to extend drastically and unrealistically. As the coupling of the models both combines complex theoretical models and numerical integration schemes, the implementation is complicated. It is unfortunate that it has been impossible to simulate the model numerically and compare the numerical and experimental results. Finally, as only one set of dimensional parameters have been tested, it would have been interesting to see the effect of changing the dimensions like air-gap, the cross-sectional diameter of the tori and radius of the circular tori. This study is easier to conduct numerically. It is likely to believe that an optimization of the model parameters can improve the design. Thus, the model shows great potential both with and without membrane.

6.1 Further work

In the work with developing the multi-torus concept to a full scale floating solar island, further research of certain subjects is necessary. The mooring line parameter dependencies to overtopping behaviour aft on the two outer tori should be further investigated. As the effect of the membrane is studied for the first time in this thesis, the dimensional and elastic parameters could be optimized through further studies. This also counts for the other dimensional parameters of the models. An ocean prototype of larger scale is also of interest to test in further research.

Elastic properties of the deck and realistic scaling of these is essential. The equipment and solar panels mounted on the deck will need to keep stable, having possibilities for fixing the solar panels and be a safe workspace. However, it is important that the membrane is kept elastic so that the model can keep its properties making it able to follow the waves smoothly. Concerning overtopping, a study where the forces on the tori and membrane are measured when overtopping occurs would be interesting. Overtopping behaviour in irregular waves should be more closely documented, as overtopping earlier has been observed on several angular locations around the tori for irregular sea states. The eigenfrequencies and vibrations induced on the membrane are also subjects of interest.

Concerning the numerical implementation, it is left to following studies to investigate whether the theoretical models used can describe the behaviour of a complex structure like the multi-torus well. Further numerical studies, coupling the truss and floater models with a membrane model describing the behaviour of the deck in addition to developing the geometry to equal the multi-torus model will complete the numerical implementation and make it possible to compare the numerical simulation results with experiments. Finally, the low-frequency slender body theory is more complicated to implement but could replace the zero-frequency theory for better accuracy of the floater motions and forces.

References

[Atkinson, 1978] Atkinson, K. E. (1978). *An introduction to numerical analysis*. Wiley, New York, second edition.

[Calvão and Penna, 2015] Calvão, A. C. and Penna, T. J. P. (2015). The double pendulum: a numerical study. *European Journal of Physics*, 36(4).

[Dean and Dalrymple, 1984] Dean, R. G. and Dalrymple, R. A. (1984). *Water wave mechanics for Engineers and Scientists*. Prentice-Hall Inc.

[DNV-GL, 2017] DNV-GL (2017). Renewables, power and energy use forecast to 2050. *Energy Transition Outlook*.

[Faltinsen, 1993] Faltinsen, O. (1993). *Sea loads on ships and offshore structures*, volume 1. Cambridge university press.

[Faltinsen, 2010] Faltinsen, O. M. (2010). Current and wave loads on floating fish farms. CeSOS.

[Faltinsen, 2011] Faltinsen, O. M. (2011). Hydrodynamic aspects of a floating fish farm with circular collar. In *International Workshop on Water Waves and Floating Bodies*, volume 26.

[Goeppert et al., 2014] Goeppert, A., Czaun, M., Jones, J.-P., Prakah, S. G., and George, O. A. (2014). Recycling of carbon dioxide to methanol and derived products – closing the loop. *Chemical Society Reviews*, Rev. 2014,43, 7995-8048.

[Greco, 2001] Greco, M. (2001). *A Two-Dimensional Study of Green-Water Loading*. PhD thesis, NTNU.

[Greco, 2012] Greco, M. (2012). *TMR4215: Sea Loads, Lecture Notes*. Department of Marine Hydrodynamics, NTNU.

[Irgens, 2003] Irgens, F. (2003). Formelsamling-mekanikk, 3. utgave.

[Kirkby, 2011] Kirkby, L. (2011). *Physics: A Student Companion.* Scion Publishing.

[Kristiansen, 2010] Kristiansen, D. (2010). *Wave induced effects on floaters of aquaculture plants*. PhD thesis, NTNU.

[Kristiansen, 2012] Kristiansen, T. (2012). Linearized hydroelastic theory of circular floater in
"fishfarm" fortran code. Post Doc.

[Kristiansen and Borvik, 2018] Kristiansen, T. and Borvik, P. (2018). Powerpoint presentation:
Investigation of an air-cushion supported solar island. In *Proceedings of ASME 2018 37th
International Conference on Ocean, Offshore and Arctic Engineering, OMAE2018-78533*.

[Kristiansen and Brovik, 2018] Kristiansen, T. and Brovik, P. (2018). Investigation of an air-
cushion supported solar island. In *Proceedings of ASME 2018 37th International Conference
on Ocean, Offshore and Arctic Engineering, OMAE2018-78533*.

[Kristiansen et al., 2017] Kristiansen, T., Lugni, C., Søreide, T., Alsos, H. S., and Birknes-
Berg, J. (2017). Floating marine structures for harvesting solar energy to power synthetic
carbon-neutral fuel production from recycled co2. Unpublished preproposal to MarTERA.

[Lewis and Nocera, 2006] Lewis, N. S. and Nocera, D. G. (2006). Powering the planet:
Chemical challenges in solar energy utilization. *Proceedings of the National Academy of
Sciences*, 103(43):15729–15735.

[Li, 2017] Li, P. (2017). *A Theoretical and Experimental Study of Wave-induced Hydroelastic
Response of a Circular Floating Collar*. PhD thesis, NTNU.

[Li and Faltinsen, 2012] Li, P. and Faltinsen, O. M. (2012). Wave-induced vertical response
of an elastic circular collar of a floating fish farm. In *The 10th International Conference on
Hydrodynamics*, volume 2.

[Li et al., 2014] Li, P., Faltinsen, O. M., and Greco, M. (2014). Wave-induced accelerations
of a fish farm elastic floater: experimental and numerical studies. In *Proceedings of the
ASME 2014 33rd International Conference on Ocean, Offshore and Arctic Engineering*,
OMAE2014-23302.

[Marichal, 2003] Marichal, D. (2003). Cod-end numerical study. In *Third International
Conference on Hydroelasticity in Marine Technology*.

[Marino et al., 2019] Marino, E., Kiendl, J., and De Lorenzis, L. (2019). Explicit isogeometric
collocation for the dynamics of three-dimensional beams undergoing finite motions.
Computer Methods in Applied Mechanics and Engineering, 343:530–549.

[MossMaritime, 2018] MossMaritime (2018). Floating solar park.

[Newman, 1977] Newman, J. N. (1977). The motions of a floating slender torus. *Journal of
Fluid Mechanics*, 83(4):721–735.

[Patterson et al., 2015] Patterson, B., Holzner, R., Kurum, A., Rossel, C., Willauer, H. D.,
and van Bokhoven, J. A. (2015). Proposed liquid fuel production on artificial islands. In
Conference on Energy, Science and Technology 2015, Book of Abstracts.

[Steen, 2014] Steen, S. (2014). Tmr7 experimental methods in marine hydrodynamics, lecture notes.

[UNDP, 2015] UNDP (2015). Sustainable development goals. *United Nations Development Program.*

[Vistnes, 2018] Vistnes, A. I. (2018). *Numerical Methods*, pages 59–91. Springer International Publishing, Cham.

[Windsvold, 2018] Windsvold, J. (2018).   An experimental study on the wave-induced hydroelastic response of a floating solar island. Master's thesis, NTNU.

Appendix A

Additional theory

A.1 Froude scaling

To obtain valid results in an experiment, similarity in forces between model and full scale is required. According to [Steen, 2014], there are three similarity conditions which need to be fulfilled. There has to be geometric similarity between the structures, which means the shape of the structures are independent of the scale. This is true if there exists a constant scale ratio between the two. A kinematic similarity needs to be fulfilled, which means the non-dimensional velocity has to be the same in model scale and full scale. A dynamic similarity is achieved if the force contributions and elastic relative deformations have the same ratio in all scales. If all similarities are obtained, the model assures a valid representation of the full scale problem.

It will not be possible to satisfy all scaling laws in a practical test condition, since the the density of water and air are limiting parameters and independent of scale. Similarity in Froude number can assure similarity in gravity and inertia forces. As the model tested pierces the surface with a small draft relative to the diameter, it is assumed that gravity forces are governing. This implies that equality in Froude number is important. The Froude number is defined by equation (A.1), where U is velocity $[m/s]$, g is the gravitational acceleration $[m/s^2]$ and L is the characteristic length $[m]$ of the model. Geometrical similarity is also achieved, as the model was made with a constant scale ratio Λ equal to 50. Froude scaling parameters used in the model testing are defined in table A.1. The eventual difference in water density between full scale and model scale, ρ_F/ρ_M, should be included in the scaling factor.

$$Fn = \frac{U}{\sqrt{gL}} \tag{A.1}$$

Kinematic similarity could be obtained by equality in Reynolds number (*Re*). This will affect the representation of viscous forces. The Reynolds number is defined by equation (A.2), and as observed it is dependent of kinematic viscosity (ν). As this is independent of scale, kinematic

similarity will be impossible to achieve since the velocity is a limiting parameter in the testing facility.

$$Re = \frac{UL}{\nu} \tag{A.2}$$

Table A.1: Froude scaling parameters, all represented by the scale ratio $\lambda_S = L_F/L_M$ [-].

Physical parameter	Scaling factor
Length	λ_S
Pressure	λ_S
Surface	λ_S^2
Volume	λ_S^3
Mass	λ_S^3
Force	λ_S^3
Moment	λ_S^4
Density	1
Acceleration	1
Velocity	$\sqrt{\lambda_S}$
Time	$\sqrt{\lambda_S}$
Kinematic viscosity	$\lambda_S^{3/2}$
Dynamic viscosity	$\lambda_S^{3/2}$

A.2 Regular wave theory

Regular wave theory in finite water depth is used to calculate the properties of the waves used in model testing. Equation (A.3) describes the finite water depth dispersion relation in regular wave theory, in addition to the relation between the wave number and the wave length, as well as the wave frequency and the wave period. An iterative process using equations (A.3) need to be applied to find the wave numbers k from the corresponding wave periods T. Wave steepness H/λ and wave period T will be used as known parameters, to classify the waves. When k is known, the corresponding wave length λ and wave height H can be found. The wave height $H = 2\zeta_a$, where ζ_a is the wave amplitude. The different parameters are defined in figure A.1.

$$\frac{\omega^2}{g} = k \tanh kh \qquad k = \frac{2\pi}{\lambda} \qquad \omega = \frac{2\pi}{T} \tag{A.3}$$
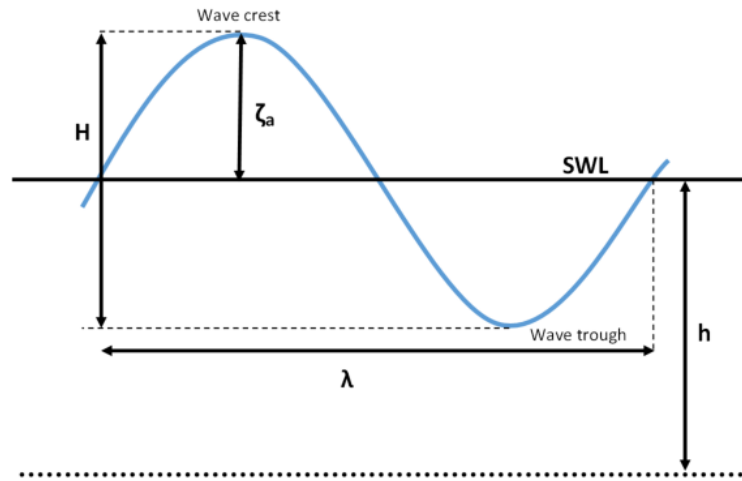
Figure A.1: Regular sinusoïdal wave. H is wave height, ζ_a = H/2 is wave amplitude, λ is wave length and SWL is still water level.

Appendix B

Additional figures and tables

B.1   Main parameters of the tori used in the model tests

Table B.1: Diameter and weight properties of the tori in full scale and model scale. Torus 1 is largest ring and the diameter is decreasing as the torus number increases. Data from [Windsvold, 2018].

Torus number	Model scale		Full scale	
	Diameter [m]	Weight [kg]	Diameter [m]	Weight [10^3kg]
1	1.020	0.83	50	103.8
2	0.825	0.70	40	87.5
3	0.620	0.55	30	68.8
4	0.423	0.40	20	50.0
5	0.228	0.23	10	28.8

B.2   Channel descriptions

Table B.2 presents the channel descriptions of all 88 channels.

B.3   Wave test parameters

Table B.3 presents the the wave number, model and full scale wave period of all 61 tests in the test matrices.

Channel	Description	Channel	Description
0	Time 1 - default sample rate	44	y15
1	x01	45	z15
2	y01	46	x16
3	z01	47	y16
4	x02	48	z16
5	y02	49	x17
6	z02	50	y17
7	x03	51	z17
8	y03	52	x18
9	z03	53	y18
10	x04	54	z18
11	y04	55	x19
12	z04	56	y19
13	x05	57	z19
14	y05	58	x20
15	z05	59	y20
16	x06	60	z20
17	y06	61	x21
18	z06	62	y21
19	x07	63	z21
20	y07	64	x22
21	z07	65	y22
22	x08	66	z22
23	y08	67	x23
24	z08	68	y23
25	x09	69	z23
26	y09	70	x24
27	z09	71	y24
28	x10	72	z24
29	y10	73	Time 2 - default sample rate
30	z10	74	F5990_045
31	x11	75	F5994_135
32	y11	76	F8033_225
33	z11	77	F8038_315
34	x12	78	FlapPosition
35	y12	79	Time 3 - default sample rate
36	z12	80	WP1
37	x13	81	WP2
38	y13	82	WP3
39	z13	83	WP4
40	x14	84	WP5
41	y14	85	WP6
42	z14	86	Total_Force_Front
43	x15	87	Total_Force_Back

Table B.2: Channel descriptions of all 88 channels measured.

Test no	k $[m^{-1}]$	T_{model} $[s]$	$T_{full}[s]$	Test no	k $[m^{-1}]$	T_{model} $[s]$	$T_{full}[s]$
0	12.5800	0.5656	3.9994	31	6.7915	0.7698	5.4435
1	12.3933	0.5698	4.0294	32	6.6047	0.7807	5.5201
2	12.2065	0.5742	4.0601	33	6.4180	0.7920	5.6000
3	12.0198	0.5786	4.0915	34	6.2313	0.8038	5.6834
4	11.8331	0.5832	4.1236	35	6.0446	0.8161	5.7708
5	11.6464	0.5878	4.1566	36	5.8578	0.8291	5.8625
6	11.4596	0.5926	4.1903	37	5.6711	0.8427	5.9587
7	11.2729	0.5975	4.2249	38	5.4844	0.8570	6.0599
8	11.0862	0.6025	4.2603	39	5.2977	0.8721	6.1667
9	10.8995	0.6076	4.2966	40	5.1109	0.8880	6.2794
10	10.7127	0.6129	4.3339	41	4.9242	0.9049	6.3989
11	10.5260	0.6183	4.3722	42	4.7375	0.9229	6.5257
12	10.3393	0.6239	4.4115	43	4.5508	0.9420	6.6609
13	10.1526	0.6296	4.4519	44	4.3640	0.9624	6.8054
14	9.9658	0.6355	4.4934	45	4.1773	0.9844	6.9604
15	9.7791	0.6415	4.5361	46	3.9906	1.0080	7.1275
16	9.5924	0.6477	4.5800	47	3.8038	1.0336	7.3086
17	9.4056	0.6541	4.6253	48	3.6171	1.0615	7.5057
18	9.2189	0.6607	4.6719	49	3.4304	1.0920	7.7219
19	9.0322	0.6675	4.7199	50	3.2437	1.1258	7.9605
20	8.8455	0.6745	4.7695	51	3.0569	1.1634	8.2262
21	8.6587	0.6817	4.8206	52	2.8702	1.2056	8.5248
22	8.4720	0.6892	4.8735	53	2.6835	1.2535	8.8639
23	8.2853	0.6969	4.9281	54	2.4968	1.3087	9.2538
24	8.0986	0.7049	4.9846	55	2.3100	1.3730	9.7082
25	7.9118	0.7132	5.0431	56	2.1233	1.4490	10.2463
26	7.7251	0.7218	5.1037	57	1.9366	1.5407	10.8947
27	7.5384	0.7307	5.1666	58	1.7499	1.6536	11.6925
28	7.3517	0.7399	5.2318	59	1.5631	1.7957	12.6976
29	7.1649	0.7495	5.2996	60	1.3764	1.9800	14.0004
30	6.9782	0.7594	5.3701				

Table B.3: The wave number, model and full scale wave period of all 61 tests in the test matrices.

Appendix C

Specifications and observations from November model tests

C.1 Specifications of model and set-up

The multi-torus model built by [Windsvold, 2018] was tested in *Lilletanken* during the work with the project thesis. The connecting trusses between the tori have been replaced before the new model tests carried out during the master thesis project. In addition to this, set-up is somewhat different and both the mooring lines spring stiffness and pre-tension are lower than originally. Below, further differences are presented in detail.

The model is moored to an initial position with four mooring lines attached to the outer torus at $\beta = 45°$, $\beta = 135°$, $\beta = 225°$ and $\beta = 315°$. Each mooring line consists of a force ring, a spring and a rope as illustrated in figure C.2. The stiffness properties of the mooring-line spring can be found in table 4.1. Since the force rings were attached to the mooring lines between the model and the spring, and that the deflection of the ropes are small compared to the forces applied, it is assumed that the elasticity of the ropes is infinite and that the eventual elasticity does not affect the mooring line forces. The mooring lines were pre-tensioned with a force $T_p = 5 \ [N]$ with accuracy $\pm \ 0.1 \ [N]$. The pre-tension is used to avoid slack and submergence of the mooring

Table C.1: Main parameters of multi-torus in model scale and full scale [Windsvold, 2018].

Description	Parameter	Model scale	Full scale
Cross-sectional diameter of tori	d_t	$32 \ mm$	$1.6 \ m$
Torus mass per unit length	m	$0.257 \ kg/m$	$642.5 \ kg/m$
Torus bending stiffness	EI	$0.8467 \ Nm^2$	$2.65*10^8 Nm^2$
Mooring-line spring stiffness	k_s	$28.0 \ N/m$	$70.0 \ kN/m$
Truss spring stiffness	k_t	$45 \ N/m$	$112.5 \ kN/m$
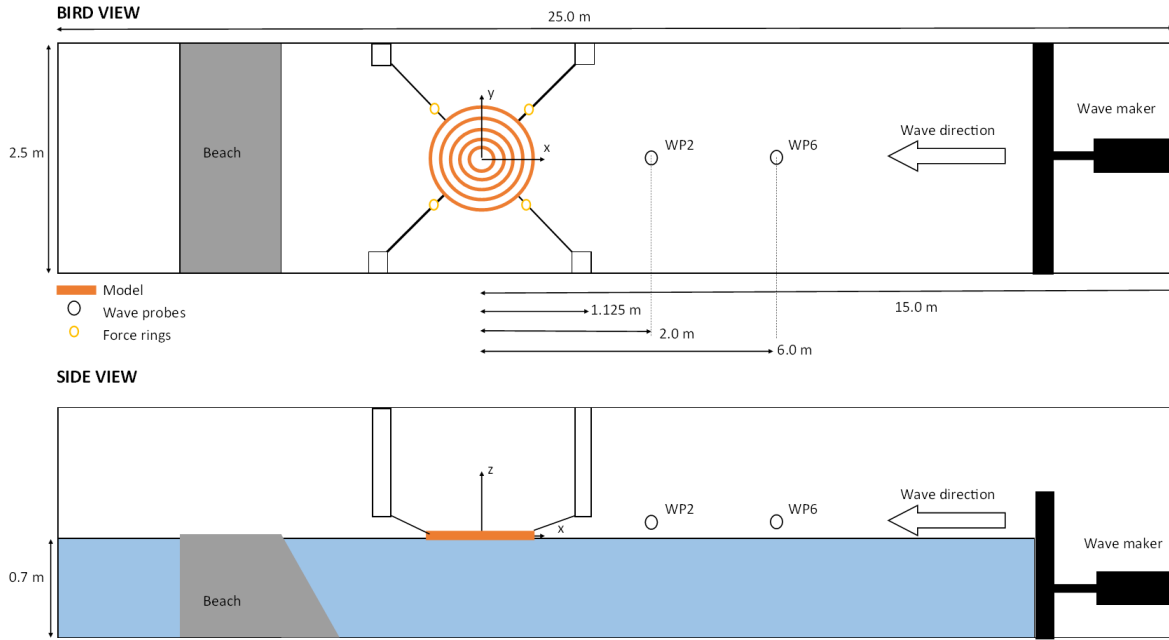
Figure C.1: Illustration of model test set-up in basin. Scale between components is not exact, but dimensions are described in figure. This corresponds to the set-up of the model tests carried out during November 2018.

lines during motion in large waves.

The wave generation file that the wave maker uses to make the desired waves is made by professor Trygve Kristiansen. The input for the test matrix is presented in table C.2. The input put into a Matlab script that generates a binary *.dat* file which the wave maker reads. The input is a combination of full scale and model scale parameters. Test series 1000 is generating waves with wave periods from 5.0 to 12.0 [s], increasing the period by 0.25 [s] for each run. Be aware that the wave periods are presented in full scale. The first interval of wave periods are run with steepness, $H/\lambda = 1/60$, while the next interval of wave periods have steepness 1/30. The water depth is set to 35 [m] full scale, which corresponds to 0.7 [m] in model scale. Each wave series has 60 wave periods, where the 5 first and 5 last are used to ramp up the wave amplitude to get a smooth increase and decrease of the waves' amplitudes. That means 10 waves are needed before desired wave properties get stationary. Between each run there was a pause of 180 [s] in order for the water surface to become calm.

Table C.2: Input to test matrix generation script

Test series	T_{min} [s]	T_{max} [s]	ΔT [s]	$(H/\lambda)_{min}$ [-]	$(H/\lambda)_{max}$ [-]	$\Delta(H/\lambda)$ [-]	h [m]	N_T [-]	N_{ramp} [-]	t_{zero} [s]
1000	5.0	12	0.25	60	30	30	35	60	5	180
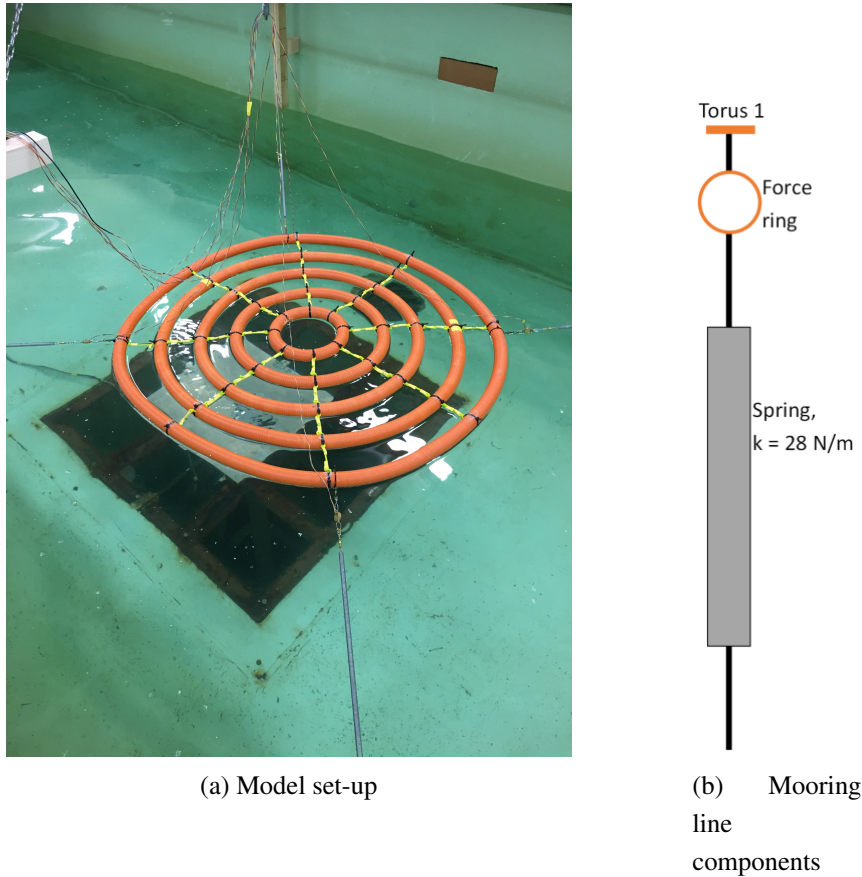
(a) Model set-up

(b) Mooring line components

Figure C.2: Model set-up with mooring lines and force rings attached to side walls of basin. The right-hand side figure illustrates the components of the mooring lines, consisting of an attachment to the torus, a force ring, a spring and a nylon rope.

During the experiments, each run was filmed by use of a Garmin VIRB camera, in order to visualize the problems, challenges and phenomenons occurring during the interaction of waves with the model. The filming was done from different positions, to get as good visual overview of the interesting areas as possible. High-speed videos and pictures were also taken using a phone. Each tape is numbered according to wave period and steepness, but as the angle and position of the cameras were different for all runs, not all are of sufficiently good quality.

C.2 Observations done during November model tests

In general, the model shows good sea keeping abilities, looks stable and follows the water surface smoothly in most cases when exposed to waves. Expected physical phenomena like overtopping and surge motions were observed. Overtopping aft on the model is observed for steep waves with long wave periods, while one event is observed fore on the outer torus for wave steepness $H/\lambda = 1/30$ and wave period T = 7.0 [s]. Large surge motions are observed for long waves causing ovalization due to large mooring line forces. A resonant type of yaw motion is observed for the smallest wave periods tested. The overtopping events are exaggerated compared to [Windsvold, 2018] due to larger pre-tension in the mooring lines, and disturbances in the water surface due to submerged mooring line springs for elevated wave amplitudes. The latter problem is caused due to horizontally attached mooring lines.
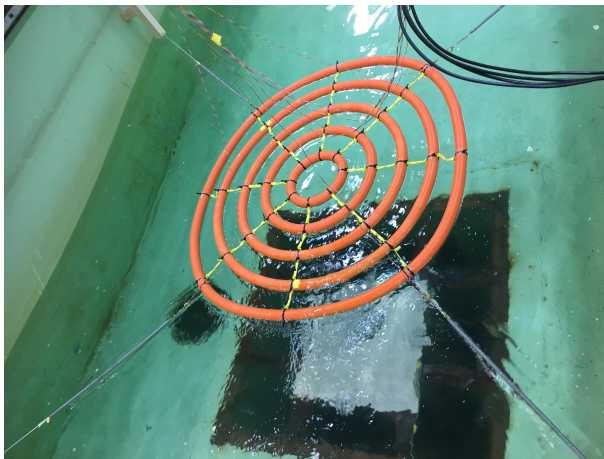
(a) Overview of overtopping on 3 outer tori

(b) Overtopping follows surface of tori, but disturbs water surface
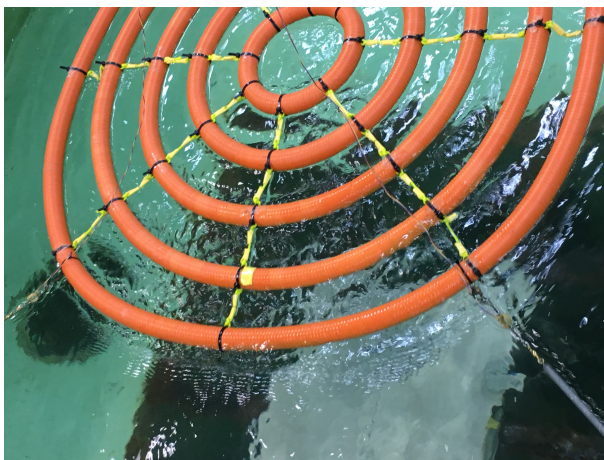
(c) Overtopping, towards wave crest

(d) Overtopping, towards wave trough

Figure C.3: Snap shots of overtopping occurring aft on the model, $H/\lambda = 1/60$, T = 11.75 [s]

Overtopping being the most obvious challenge when facing the design concept, the force of the impact loads caused should be looked further into. Most overtopping occurrences are only small amounts of water sliding over the top of the structure like a dam breaking event as described earlier. These events look rather harmless in model scale at least.

C.2.1 Overtopping

The main goal of the experiment conducted was visual observation of the model behaviour in different wave conditions and wave interaction for different steepnesses and wave periods. Overtopping at the aft part of the model was observed for wave periods higher than T $\geq$ 9.25 [s] for waves with steepness H/λ = 1/60 and for wave periods higher than T $\geq$ 6 [s] for waves with steepness H/λ = 1/30. It is observed that the phenomenon occurs at lower wave periods for increasing wave steepness. At the aft part of the model, overtopping starts at the outermost tori and is transmitted to the inner tori as the wave period increases. At the fore part of the model, overtopping was only observed for wave period T = 7 [s] and steepness H/λ = 1/30, and only on the outer tori. This is shown in figure C.6.

Overtopping is never observed at the two inner tori for steepness H/λ = 1/60. For this wave steepness, both the 2 outer tori are exposed to overtopping already for T = 9.5 [s]. The overtopping occurs only at the aft part between β = 135°and β = 180°. This means there must be asymmetry in the model set-up, since the model behaviour is supposed to be symmetric. This tendency continues for all observations of overtopping with this wave steepness. At wave period T = 10.25 [s], the overtopping phenomena does not only happen when the model is moving in the negative x-direction as it follows the wave crest, but also when the model moves in the positive x-direction into the wave trough. From wave period T = 11 [s], the 3 outer tori are exposed to overtopping. For wave periods higher than T $\geq$ 11.25 [s], the complete area between β = 135°and β = 180°is exposed to overtopping, and there is also some exposure below these angular positions as the wave period increases. As the wave period gets higher than T $\geq$ 11.75 [s], there is observed more water flowing over the tori as the model moves into the wave trough, than when it moves up on the wave crest. For the complete test with wave steepness $H\lambda$ = 1/60, there is only small amounts of water flowing over the rings. All of the water flowing over follows the shape of the circular ring, and no signs of sloshing are observed.

For wave steepness H/λ = 1/30, overtopping is first observed at the two outer tori between β = 135°and β = 180°already at wave period T = 6 [s]. Already at T = 7 [s], the 3 outer tori are exposed to overtopping. For wave periods higher than T $\geq$ 7.25, overtopping also occurs at larger angles than β = 180°, and the exposure for some reason seems to get more symmetric from here and during the next tests for an unknown reason. Already at T = 8.75 [s], there is more water flowing over the tori than for wave steepness H/λ = 1/60, and it is observed that the water is also more disturbed as is flows over. There is no longer a smooth water surface flowing over the tori. At this point, there is also more water flowing over the tori when the model moves

into a wave trough than when it moves up to the wave crest. For wave periods higher than T $\geq$ 10[s], the complete 90 °aft on the model is exposed to overtopping. That means between β = 135°and β = 225°, and as the wave period increases also below these angular positions. At wave periods higher than T $\geq$ 10.75 [s], there is also observed overtopping at β = 90°and β = 270 °. This is illustrated by figure C.5.

C.2.2 Surge motion

There is observed surge motion on the model due to the longitudinal waves. It is expected that the model will follow the waves and being led in the direction of the waves as there is a wave crest, while moving back towards it's initial position as it meets a wave trough. The surge motion increases as the wave period increases. For the lowest wave periods tested, there is almost no surge motion, as the yaw motion dominates.

C.2.3 Yaw motion

For the lowest wave periods tested, there is a clear tendency of yaw rotation. For wave steepness H/λ = 1/60, the rotation is mainly observed for wave periods T = 5.5 - 6.75 [s], with the biggest rotation at wave period T = 5.75 [s]. When it comes to wave steepness H/λ = 1/30, the yaw rotation is observed for the same wave periods, with the largest rotation at T = 6 [s]. The observations signalize resonance in yaw around this period. The yaw motion is triggered by asymmetry in the model. It is observed that the model gets an oval shape when the mooring lines are pre-tensioned. This means the pre-tension in the set-up is to large compared to the elasticity of the model. The rotation can be observed in figure C.4.

(a) Yaw rotation   (b) Yaw rotation
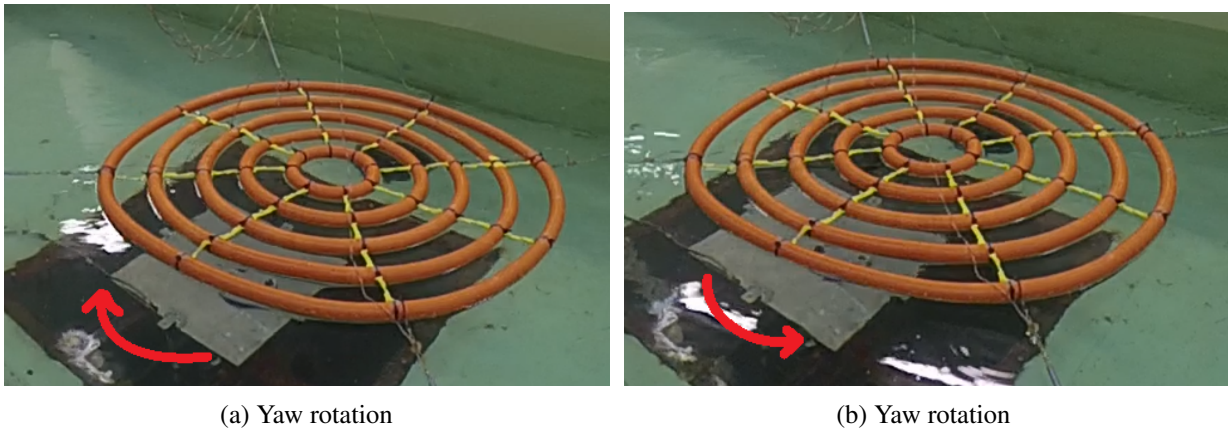
Figure C.4: Snap shots of yaw motion at H/λ = 1/60, T = 5.75 [s]. The yaw motion can be seen from the asymmetry in the mooring force attachment points on the model.
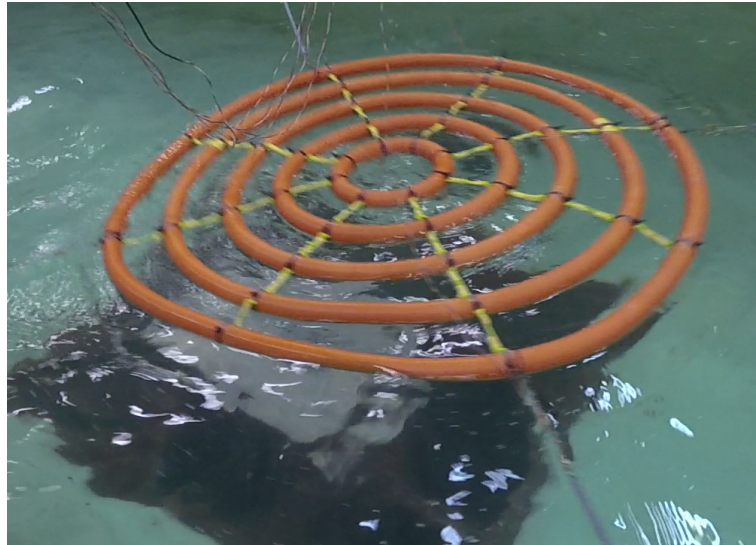
(a) Overtopping at front of $\beta = 90°$

(b) Zoomed view

Figure C.5: Snap shot of overtopping occurring at $\beta = 90$ °, from video of T = 11.25 [s], H/λ = 1/30. Overtopping occurs at the side, and a run-up from a wave is seen in the zoomed view.
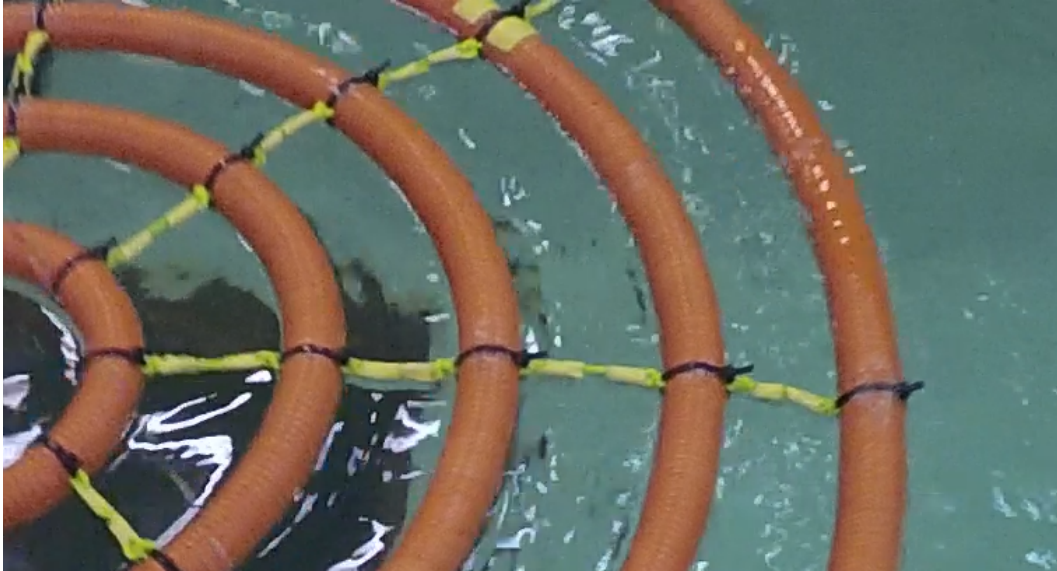
(a) Zoomed view of overtopping fore
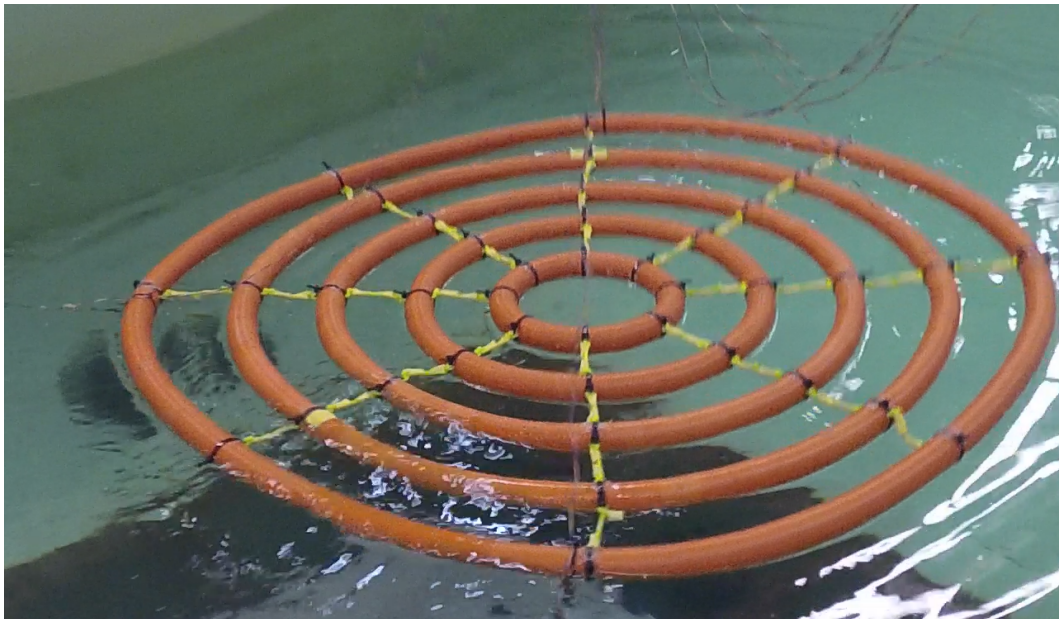
(b) Overview of overtopping aft

Figure C.6: Snap shots of overtopping occurring tat H/λ = 1/30, T = 7.0 [s]. Overtopping occurring at the fore outer torus and at the aft.
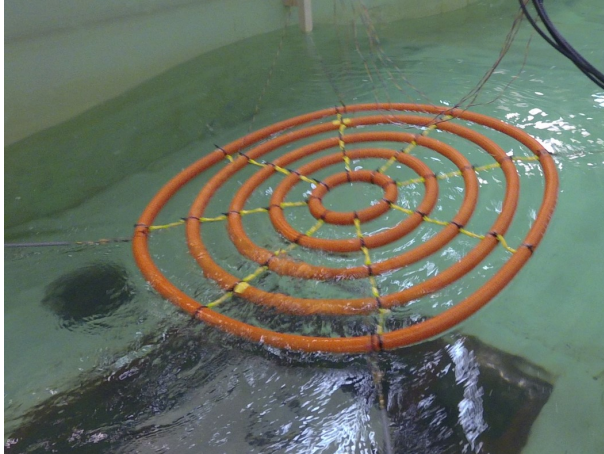
(a) Overtopping on 4 outer tori, moving towards wave crest
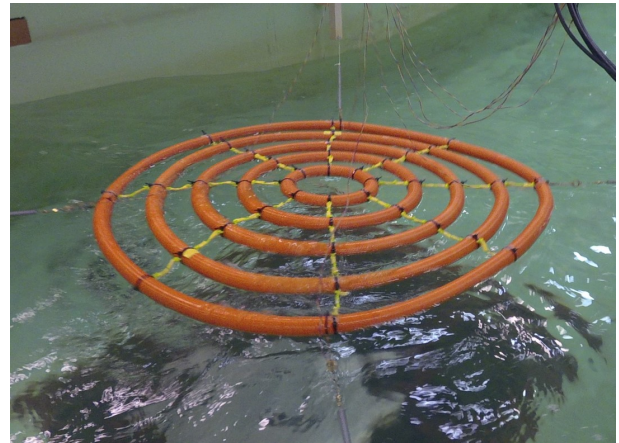
(b) Model moving towards wave trough, overtopping on tori 2 & 3

(c) Model moving towards new wave crest, overtopping on 4 tori aft

(d) Model moving towards new wave trough, overtopping on 3 outer tori
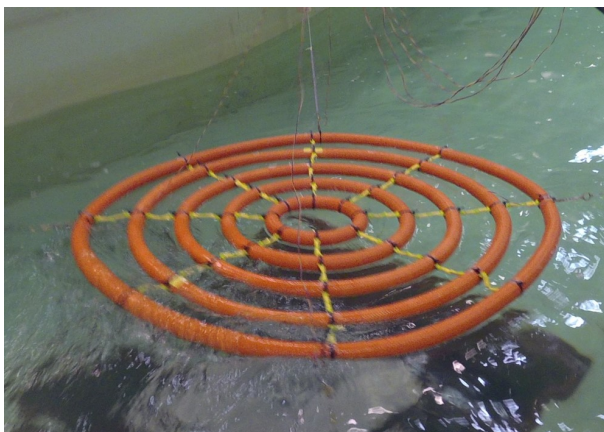
(e) Model moving towards new wave trough, overtopping on 4 tori aft
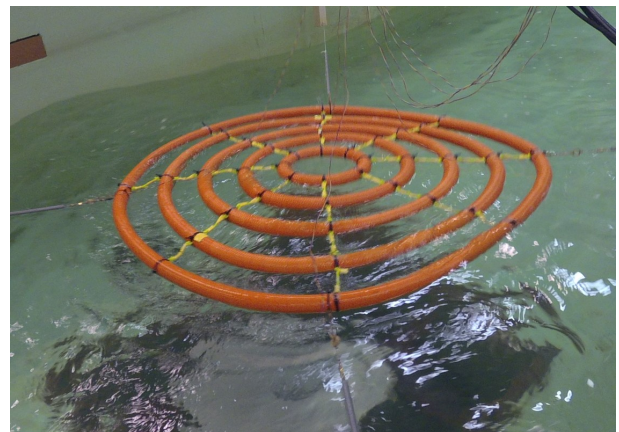
(f) Overtopping at $\beta = 90°$ when model is on wave crest

Figure C.7: Snap shots of overtopping occurring at $H/\lambda = 1/30$, T = 10.75 [s], aft on the model.

Appendix D

Additional details on numerical simulation

D.1 Verification studies

D.1.1 Suspended wire

The suspended wire is modelled by the numerical parameters described in table D.1, and its geometry can be seen in figure D.1. Node 1 and 6 are fixed. This is done numerically by keeping the nodal position constant, as well as the velocity and acceleration equal to zero in all time steps. Physical properties are presented in table 3.1, and the only external forces applied are gravity forces. Using the material density and cross-sectional area, the mass is calculated for each truss and lumped to the nodes. Normal behaviour would be that the wire vibrates in the vertical direction as time goes, since the internal tension will change in time and gravity forces will aim to equalize them. A stable equilibrium position will never be obtained, as there is no damping forces applied to the system.

From equation 2.47, the system of equations $\mathbf{A}T = b$ of the suspended wire can be derived. For simplification, $w_i = 2\Delta t/m_i$, $w_{ji} = w_j + w_i$ and $\vec{x}_{ji} = \vec{x}_j - \vec{x}_i$ where node i signifies end 1 and j signifies end 2 of truss k. Remark that $\hat{s}_k$ and l_{0k} signifies tangential unit vector and initial length of truss k respectively. Each row in the system of equations corresponds to one truss element.

Table D.1: Numerical properties of suspended

Variable	Parameter	Unit	Value
Number of trusses	N_{truss}	[-]	5
Time step length	Δ t	$[s]$	10^{-4}
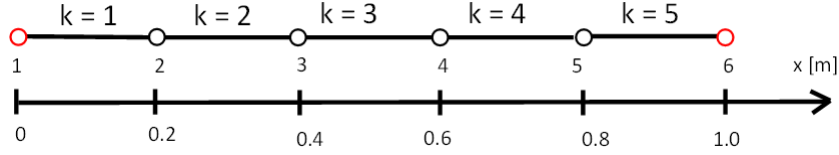
Figure D.1: Connectivity formulation of the suspended wire, with node 1 & 6 fixed. Each truss has initial length of 0.2 $[m]$, and flexibility properties according to table 3.1.

$$\mathbf{A} = \begin{bmatrix} -w_{21}\hat{s}_1 \cdot \vec{x}_{21} - \frac{l_{01}^2}{\Delta t}\chi & w_2\hat{s}_2 \cdot \vec{x}_{21} & 0 & 0 & 0 \\ w_2\hat{s}_1 \cdot \vec{x}_{32} & -w_{32}\hat{s}_2 \cdot \vec{x}_{32} - \frac{l_{02}^2}{\Delta t}\chi & w_3\hat{s}_3 \cdot \vec{x}_{32} & 0 & 0 \\ 0 & w_3\hat{s}_2 \cdot \vec{x}_{43} & -w_{43}\hat{s}_3 \cdot \vec{x}_{43} - \frac{l_{03}^2}{\Delta t}\chi & w_4\hat{s}_4 \cdot \vec{x}_{43} & 0 \\ 0 & 0 & w_4\hat{s}_3 \cdot \vec{x}_{54} & w_{54}\hat{s}_4 \cdot \vec{x}_{54} - \frac{l_{04}^2}{\Delta t}\chi & w_5\hat{s}_5 \cdot \vec{x}_{54} \\ 0 & 0 & 0 & w_5\hat{s}_4 \cdot \vec{x}_{65} & -w_{65}\hat{s}_5 \cdot \vec{x}_{65} - \frac{l_{05}^2}{\Delta t}\chi \end{bmatrix}$$
(D.1)

The $\mathbf{A}$-matrix of the system is presented in (D.1) and the equation system with the corresponding b-vector is presented in equation (D.2). In the b-vector, the gravity force terms $\frac{2\Delta t}{m_j}m_j\vec{g} - \frac{2\Delta t}{m_i}m_i\vec{g}$ cancel.

$$\mathbf{A}T = b \Leftrightarrow \mathbf{A}\begin{bmatrix} T_1 \\ T_2 \\ T_3 \\ T_4 \\ T_5 \end{bmatrix} = \begin{bmatrix} \frac{l_{01}^2}{\Delta t} - \left\{\frac{\vec{x}_{21}}{2\Delta t} + \vec{u}_{21}\right\} \cdot \vec{x}_{21} \\ \frac{l_{02}^2}{\Delta t} - \left\{\frac{\vec{x}_{32}}{2\Delta t} + \vec{u}_{32}\right\} \cdot \vec{x}_{32} \\ \frac{l_{03}^2}{\Delta t} - \left\{\frac{\vec{x}_{43}}{2\Delta t} + \vec{u}_{43}\right\} \cdot \vec{x}_{43} \\ \frac{l_{04}^2}{\Delta t} - \left\{\frac{\vec{x}_{54}}{2\Delta t} + \vec{u}_{54}\right\} \cdot \vec{x}_{54} \\ \frac{l_{05}^2}{\Delta t} - \left\{\frac{\vec{x}_{65}}{2\Delta t} + \vec{u}_{65}\right\} \cdot \vec{x}_{65} \end{bmatrix}$$
(D.2)

By using the equation system defined above, the system can be integrated in time to solve for the unknown tension forces T at each time step n. Knowing these, the corresponding unknown nodal positions of the next time step can be found from the Implicit-Explicit Euler method.

D.1.2 Simple rigid pendulum

Table D.2: Simulation properties of simple pendulum simulation. A simple sensitivity study of the time step is conducted, searching for a stable solution. More testing would be necessary to be sure the solution stays stable.

Variable	Parameter	Unit	Value
Number of truss	N_{truss}	[-]	1
Time step length	Δt	$[s]$	$10^{-3}, 10^{-4}$
Initial positions	θ_0	[°]	45, 90, 135
Point mass	M_{point}	$[kg]$	1

(a) Simple pendulum geometry

(b) Vertical point mass displacement in time.
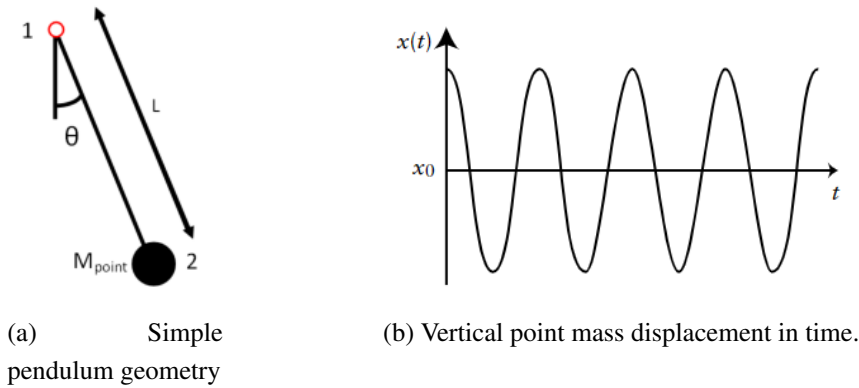
Figure D.2: Simple pendulum geometry and analytic solution of vertical point mass displacement in time starting from an initial position of angle θ_0 and oscillating symmetrically around $\theta = 0$. Right figure: courtesy to [Kirkby, 2011].

The simple pendulum has a geometry as defined in figure D.2 a) and numerical properties according to table D.2. It is modelled by one rigid truss element, which is massless and fixed in end 1. A point mass is placed in node 2. Initial position is defined by the angle θ_0. According to theory, as the truss is rigid and there is no damping forces included, the pendulum should move symmetrically around $\theta = 0°$, with maximum angular displacement equal to $\pm\theta_0$, which corresponds to the initial position. This can be illustrated by figure D.2 b). Oscillation period T_0 is approximated by equation (3.9), which defines a power series developed from the ODE of the simple pendulum $\frac{d^2\theta}{dt^2} + \frac{g}{L}\sin\theta$ [Kirkby, 2011]. Thus, the pendulum in this case study has oscillation periods according to table 3.2. It can be observed from the ODE or the power series that the model motion is independent of mass, which means the model will act equally no matter what point mass is used. This is due to the rigid massless truss, which makes the system only dependent of the gravity force and the length L. For small initial angle θ_0, the oscillation period can be approximated as $T_0 = 2\pi\sqrt{\frac{L}{g}}$.

D.1.3 Simple flexible pendulum

To model the simple flexible pendulum, the rigid simple pendulum configuration is modified to include elasticity in the truss. The elasticity coefficient is calculated by use of the properties in table 3.1, but the cross-sectional area is not used to calculate the mass of the truss, as the truss is still massless. Since there is no bending stiffness EI implemented in the truss element model, it is expected that the truss will act as a flexible cable. The simple flexible pendulum model is tested with use of the same numerical parameters as the simple rigid pendulum (ref. table D.2). The behaviour is expected to be a combination of a rigid pendulum motion and a spring - mass system where the spring creates vibration as it stretches and compresses. This means the oscillation pattern will be changed due to the additional vibrations of the chord. The distance to the rotational center is changing with time, which over time will cause the oscillation motion to

be cancelled by the vibrations. A disturbed and more chaotic behaviour is therefore expected.

D.1.4 Double rigid pendulum
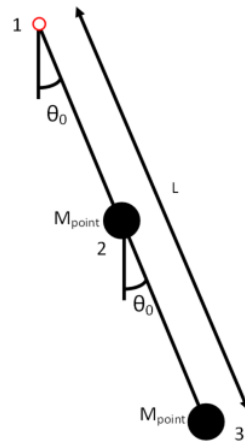
Figure D.3: Double rigid pendulum geometry. θ_0 is initial position, L is length and M_{point} is point mass. Node 1 in red is fixed (pivot).

Table D.3: Properties of double pendulum

Variable	Parameter	Unit	Value
Number of truss	N_{truss}	[-]	2
Time step length	Δt	$[s]$	10^{-4}
Initial positions	θ_0	[°]	45, 90, 135
Point masses	M_{point}	$[kg]$	1

The double rigid pendulum has geometry according to figure D.3 and numerical properties according to table D.3. The two point masses are of equal size. Even though it is possible to define the initial angular position of the two trusses differently, these are kept equal during all test cases. This simple model is a famous example of chaotic behaviour in dynamics. Even though the equations of motion of the system can be obtain using Newton's laws, it is complicated to predict the position of the second point mass without use of a proper numerical time evolution tool. As the trusses are rigid, the motion of the first truss will be similar to the behaviour of the single rigid pendulum, always circulating with the pivot as center of rotation. The difference is that the motion is no longer symmetric around the axis where $\theta = 0$, as the behaviour is disturbed by the second mass. Interaction between the two masses creates a chaotic behaviour.

The second mass is root to the chaotic behaviour. The system is strongly dependent of the initial conditions and initial angle θ_0. The second mass is rotating with the first mass as center of rotation, and the initial oscillation behaviour creates cancelling and amplification of the rotative movement of the second mass. In figure D.4, the position of the second mass during a simulation

in time is described from different initial positions. The fourth-order Adams-Bashfouth method is used with time step $dt = 10^{-5}$. Especially the plots to the right are interesting as the initial positions of the two masses have equal angle, as in this case study. θ_1 and θ_2 refers to the initial position of the first and second mass respectively. The first and second mass as well as the truss lengths are of equal size. λ_{max} is the Lyapunov exponent which in the article by [Calvão and Penna, 2015] is used as a measure of chaos in the system. If the exponent is larger than 0, there is chaos in the system, and the larger the exponent gets, the more chaos. These results are used for comparison with the results obtained from the numerical simulation.

Unlike the simple pendulum, the system's behaviour is also dependent of the size of the point masses.

D.1.5 Double compound pendulum

The double compound pendulum has the same geometry and total mass as the double rigid pendulum, but the mass is equally distributed over the rigid trusses. This means that by using the lumped mass principle, there will only be half as much mass in node 3 as in node 2. The numerical properties in table D.3 are used, and the model is tested from the same initial positions as the double pendulum. Due to the difference in mass distribution, it is expected that the second point mass will have an even more chaotic behaviour in this case. Since there is less mass in
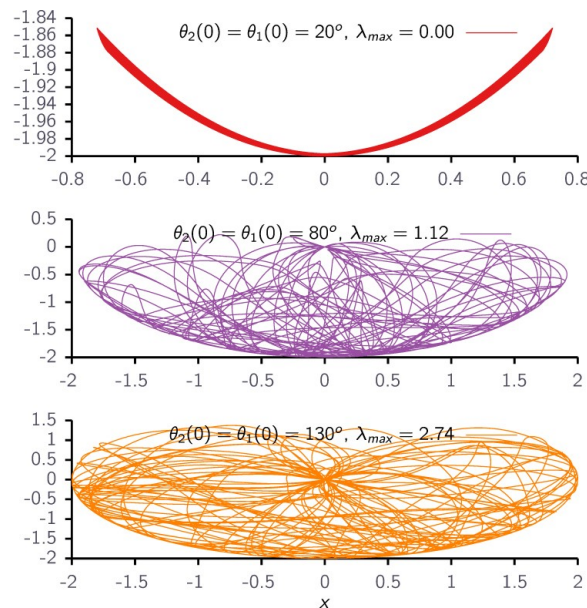
Figure D.4: Position of the second mass of a double pendulum with different initial positions from dynamic analysis with the fourth-order Adams-Bashforth method ($dt = 10^{-5}$). Initial positions of the two masses (m_1 and m_2) are of equal angle. θ_1 and θ_2 refers to the initial position of m_1 and m_2 respectively. m_1 and m_2 and the truss lengths are equal. λ_{max} is the Lyapunov exponent which is a measure of chaos in the behaviour of the system. This increases with initial position. Snap shot from article [Calvão and Penna, 2015].

the end, smaller forces will be needed to induce rotation of the end truss around its centre of rotation. However, when the mass is lower, the velocity induced by the gravity forces will be smaller.

D.1.6 Double flexible pendulum

To obtain a double flexible pendulum, the double pendulum is given flexible properties according to table 3.1. The geometry and mass distribution are kept as in the double rigid pendulum, with point masses of 1 $[kg]$ in node 2 and 3. When it comes to the numerical properties, they are according to table D.3, as for the double rigid pendulum. The behaviour will in this case depend on the mass-stiffness relationship of the model. If the flexibility is high, the spring vibratory motions of the truss will be reason for cancelling of oscillatory movement. It will also amplify chaos as both masses will be affected by the flexibility in the trusses. That means the first mass will no longer have a circular movement around the pivot, as the distance to the rotational centre will change with the elongation of the truss. The more flexibility and mass, the more chaos. As the flexibility is decreased, the behaviour will be more like the rigid double pendulum. Remark that the system depends of a realistic relationship between the mass and stiffness. As in the simple flexible pendulum case, there is no bending stiffness included in the model, so the trusses will act more as chords than beams.

D.2 12 truss coupled floater and truss model

From the truss equation 2.47 and the floater truss equation 2.48, the system of equations $\mathbf{A}T = b$ can be derived. As the model is described by 12 trusses, the system will also be described by 12 equations each referring to one truss. As mentioned above, there are three possible truss types. If a truss is connected to another truss in both ends and not affected by boundary conditions, it will be referred to as a standard truss. As one line in the equation system refers to one truss, the entries of one line are dependent of which other trusses are connected to it. Equation (D.3) describes the entries in the $\mathbf{A}$ matrix for a standard truss k. $k-1$ and $k+1$ refers to the trusses which are connected to truss k's end 1 and 2 respectively. For simplification, $w_i = 2\Delta t/m_i$, $w_{ji} = w_j + w_i$ and $\vec{x}_{ji} = \vec{x}_j - \vec{x}_i$ where node i signifies end 1 and j signifies end 2 of truss k. Remark that $\hat{s}_k$ and l_{0k} signifies tangential unit vector and initial length of truss k respectively.

$$
a_{k,(k-1)} = w_i \hat{s}_{k-1} \cdot \vec{x}_{ji}
$$
$$
a_{k,k} = -w_{ji} \hat{s}_k \cdot \vec{x}_{ji} - \frac{l_{0k}^2}{\Delta t} \chi \tag{D.3}
$$
$$
a_{k,(k+1)} = w_j \hat{s}_{k+1} \cdot \vec{x}_{ji}
$$

In this model, the fixed nodes are consequently positioned at end 1 $(k-1)$ of a truss. The only change on the entries of the $\mathbf{A}$ matrix in this case will be that $a_{k,(k-1)} = 0$, since there is no truss connected to end 1of these trusses. On the other hand, floater trusses will have a rather

more complicated change. From equation 2.48, it is observed that all trusses connected to the same truss will affect the entries of each floater truss. Since the floater trusses in this case are number 2, 5, 8 and 11, the entries of all corresponding positions will have additional terms. The additional terms are described in equation (D.4). $a_{k,(k+1)}$ will be equal to zero since there is no truss connected to node 2 for the floater trusses. The diagonal term has lost a mass term, since the mass term of the floater node is cancelled by the buoyancy of the floater.

$$a_{k,k} = -\Delta t[h_{\theta_p,\beta_j}\hat{s}_k \cdot \vec{x}_{ji}] - w_i\hat{s}_k \cdot \vec{x}_{ji} - \frac{l_{0k}^2}{\Delta t}\chi$$

$$a_{k,(k+1)} = 0$$

$$a_{k,2} + = -\Delta t[h_{1j}\hat{s}_2 \cdot \vec{x}_{ji}]$$

$$a_{k,5} + = -\Delta t[h_{2j}\hat{s}_5 \cdot \vec{x}_{ji}] \tag{D.4}$$

$$a_{k,8} + = -\Delta t[h_{3j}\hat{s}_8 \cdot \vec{x}_{ji}]$$

$$a_{k,11} + = -\Delta t[h_{4j}\hat{s}_{11} \cdot \vec{x}_{ji}]$$

The resulting matrix is presented in (D.5), showing the positions of the non-zero terms. The matrix is symmetric, but no longer banded due to the floater terms. The matrix is saved as a sparse matrix in Python, due to the numerous entries that are equal to zero.

$$\mathbf{A} = \begin{bmatrix} a_{00} & a_{01} & 0 & 0 & 0 & 0 & 0 & 0 & 0 & 0 & 0 & 0 \\ a_{10} & a_{11} & a_{12} & 0 & 0 & 0 & 0 & 0 & 0 & 0 & 0 & 0 \\ 0 & a_{21} & a_{22} & 0 & 0 & a_{25} & 0 & 0 & a_{28} & 0 & 0 & a_{2/11} \\ 0 & 0 & 0 & a_{33} & a_{34} & 0 & 0 & 0 & 0 & 0 & 0 & 0 \\ 0 & 0 & 0 & a_{43} & a_{44} & a_{45} & 0 & 0 & 0 & 0 & 0 & 0 \\ 0 & 0 & a_{52} & 0 & a_{54} & a_{55} & 0 & 0 & a_{58} & 0 & 0 & a_{5/11} \\ 0 & 0 & 0 & 0 & 0 & 0 & a_{66} & a_{67} & 0 & 0 & 0 & 0 \\ 0 & 0 & 0 & 0 & 0 & 0 & a_{76} & a_{77} & a_{78} & 0 & 0 & 0 \\ 0 & 0 & a_{82} & 0 & 0 & a_{85} & 0 & a_{87} & a_{88} & 0 & 0 & a_{8/11} \\ 0 & 0 & 0 & 0 & 0 & 0 & 0 & 0 & 0 & a_{99} & a_{9/10} & 0 \\ 0 & 0 & 0 & 0 & 0 & 0 & 0 & 0 & 0 & a_{10/9} & a_{10/10} & a_{10/11} \\ 0 & 0 & a_{11/2} & 0 & 0 & a_{11/5} & 0 & 0 & a_{11/8} & 0 & a_{11/10} & a_{11/11} \end{bmatrix} \tag{D.5}$$

The force vector corresponding to the model is presented in (D.6). Gravity force terms $\frac{2\Delta t}{m_j}m_j\vec{g} - \frac{2\Delta t}{m_i}m_i\vec{g}$ cancel in the standard trusses. Fixed nodes do not affect the terms in the b-vector of the corresponding truss. Two additional terms are added to the expression of the floater trusses, due to the right-hand side of equation (2.48). The gravity term from node 1 is kept in this case, since the gravity term of node 2 is cancelled from buoyancy forces.

$$b = \begin{bmatrix} \frac{l_{00}^2}{\Delta t} - \left\{ \frac{\vec{x}_{10}}{2\Delta t} + \vec{u}_{10} \right\} \cdot \vec{x}_{10} \\ \frac{l_{01}^2}{\Delta t} - \left\{ \frac{\vec{x}_{21}}{2\Delta t} + \vec{u}_{21} \right\} \cdot \vec{x}_{21} \\ \frac{l_{02}^2}{\Delta t} - \left\{ \frac{\vec{x}_{32}}{2\Delta t} + \vec{u}_{32} + \Delta t \sum_{n=0}^{10} \left\{ \frac{[F_{3n}^{exc} - C_{3n} a_n] \cos n\beta_1}{m + a_{33}^n} \right\} - 2\Delta t \vec{g} \right\} \cdot \vec{x}_{32} \\ \frac{l_{03}^2}{\Delta t} - \left\{ \frac{\vec{x}_{54}}{2\Delta t} + \vec{u}_{54} \right\} \cdot \vec{x}_{54} \\ \frac{l_{04}^2}{\Delta t} - \left\{ \frac{\vec{x}_{65}}{2\Delta t} + \vec{u}_{65} \right\} \cdot \vec{x}_{65} \\ \frac{l_{05}^2}{\Delta t} - \left\{ \frac{\vec{x}_{76}}{2\Delta t} + \vec{u}_{76} + \Delta t \sum_{n=0}^{10} \left\{ \frac{[F_{3n}^{exc} - C_{3n} a_n] \cos n\beta_2}{m + a_{33}^n} \right\} - 2\Delta t \vec{g} \right\} \cdot \vec{x}_{76} \\ \frac{l_{06}^2}{\Delta t} - \left\{ \frac{\vec{x}_{98}}{2\Delta t} + \vec{u}_{98} \right\} \cdot \vec{x}_{98} \\ \frac{l_{07}^2}{\Delta t} - \left\{ \frac{\vec{x}_{10/9}}{2\Delta t} + \vec{u}_{10/9} \right\} \cdot \vec{x}_{10/9} \\ \frac{l_{08}^2}{\Delta t} - \left\{ \frac{\vec{x}_{11/10}}{2\Delta t} + \vec{u}_{11/10} + \Delta t \sum_{n=0}^{10} \left\{ \frac{[F_{3n}^{exc} - C_{3n} a_n] \cos n\beta_3}{m + a_{33}^n} \right\} - 2\Delta t \vec{g} \right\} \cdot \vec{x}_{11/10} \\ \frac{l_{09}^2}{\Delta t} - \left\{ \frac{\vec{x}_{13/12}}{2\Delta t} + \vec{u}_{13/12} \right\} \cdot \vec{x}_{13/12} \\ \frac{l_{010}^2}{\Delta t} - \left\{ \frac{\vec{x}_{14/13}}{2\Delta t} + \vec{u}_{14/13} \right\} \cdot \vec{x}_{14/13} \\ \frac{l_{011}^2}{\Delta t} - \left\{ \frac{\vec{x}_{15/14}}{2\Delta t} + \vec{u}_{15/14} + \Delta t \sum_{n=0}^{10} \left\{ \frac{[F_{3n}^{exc} - C_{3n} a_n] \cos n\beta_4}{m + a_{33}^n} \right\} - 2\Delta t \vec{g} \right\} \cdot \vec{x}_{15/14} \end{bmatrix} \quad (D.6)$$

By using the equation system defined above, the system can be evaluated in time to solve for the unknown tension forces T at each time step. Knowing these, the corresponding unknown nodal positions of the next time step can be found.

Appendix E

Additional numerical results

E.1 Verification studies

E.1.1 Suspended wire
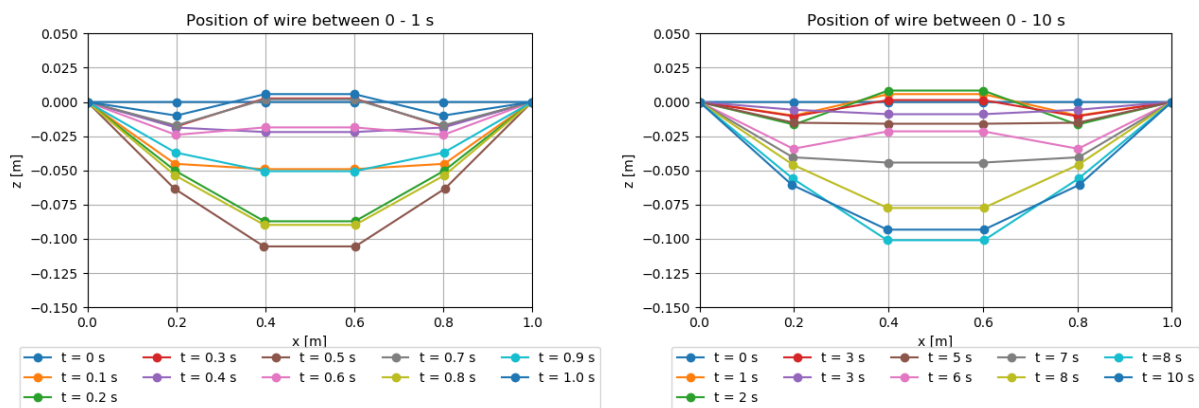
(a) Positions at time 0 - 1 s

(b) Positions at time 0 - 10 s

Figure E.1: Truss model of suspended wire modelled by 5 trusses, with dt $= 10^{-4}$ s.

E.1.2 Case study: Simple rigid pendulum

Figure E.2: **Left-hand side:** Change in vertical tip displacement of simple rigid pendulum during 10 seconds simulation, with changing initial position. **Right-hand side:** Position in time from 0 - 1 [s] of simple rigid pendulum with point mass 1 [kg] and changing initial position. The change in position indicates the oscillation period, as the time at the top position multiplied by two. Simulations with time step $dt = 10^{-4}$ [s].

E.1.3   Case study: Double compound pendulum

(a) Initial position $\theta_0 = 45°$
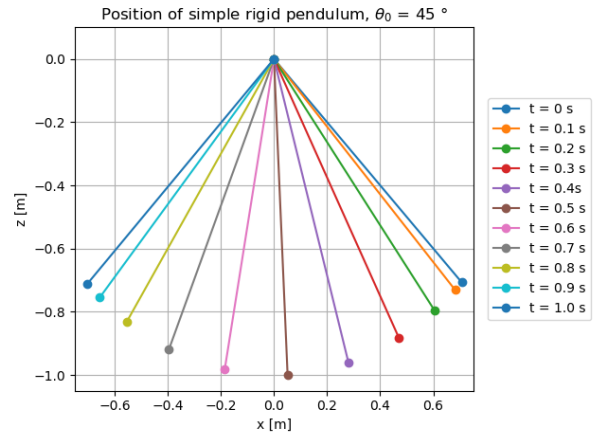
(b) Initial position $\theta_0 = 45°$
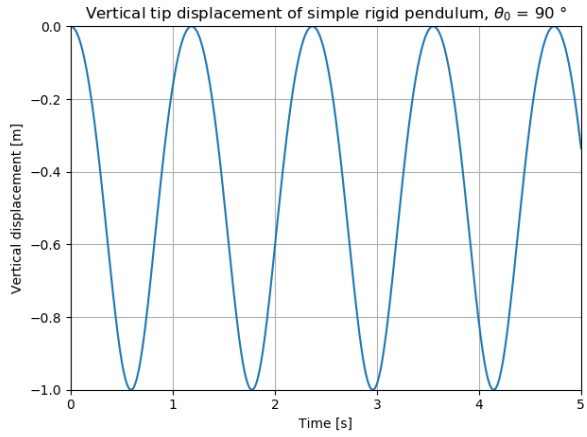
(c) Initial position $\theta_0 = 90°$
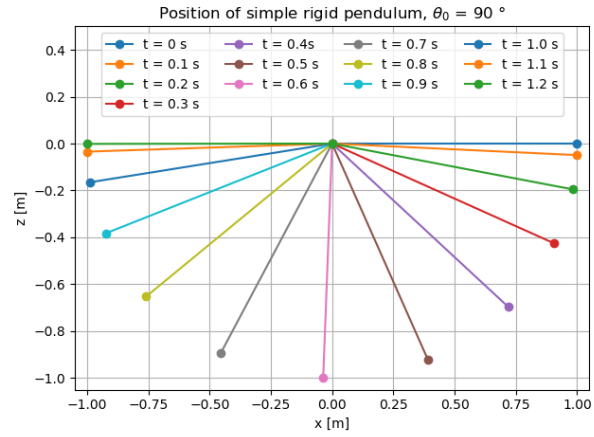
(d) Initial position $\theta_0 = 90°$
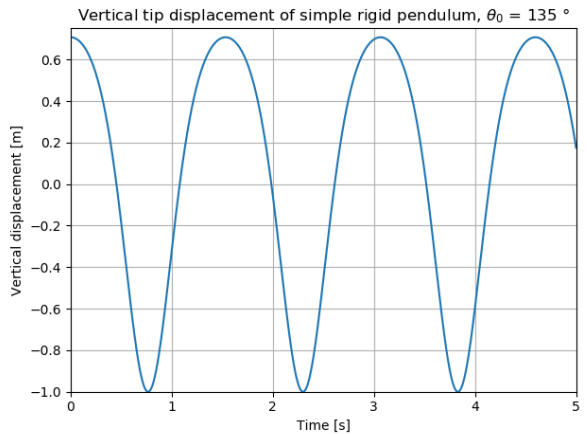
(e) Initial position $\theta_0 = 135°$
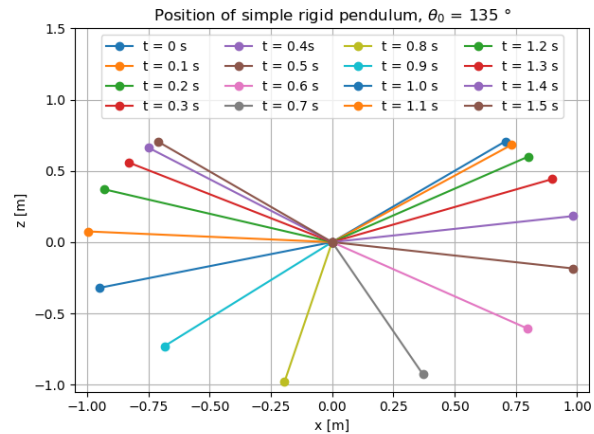
(f) Initial position $\theta_0 = 135°$
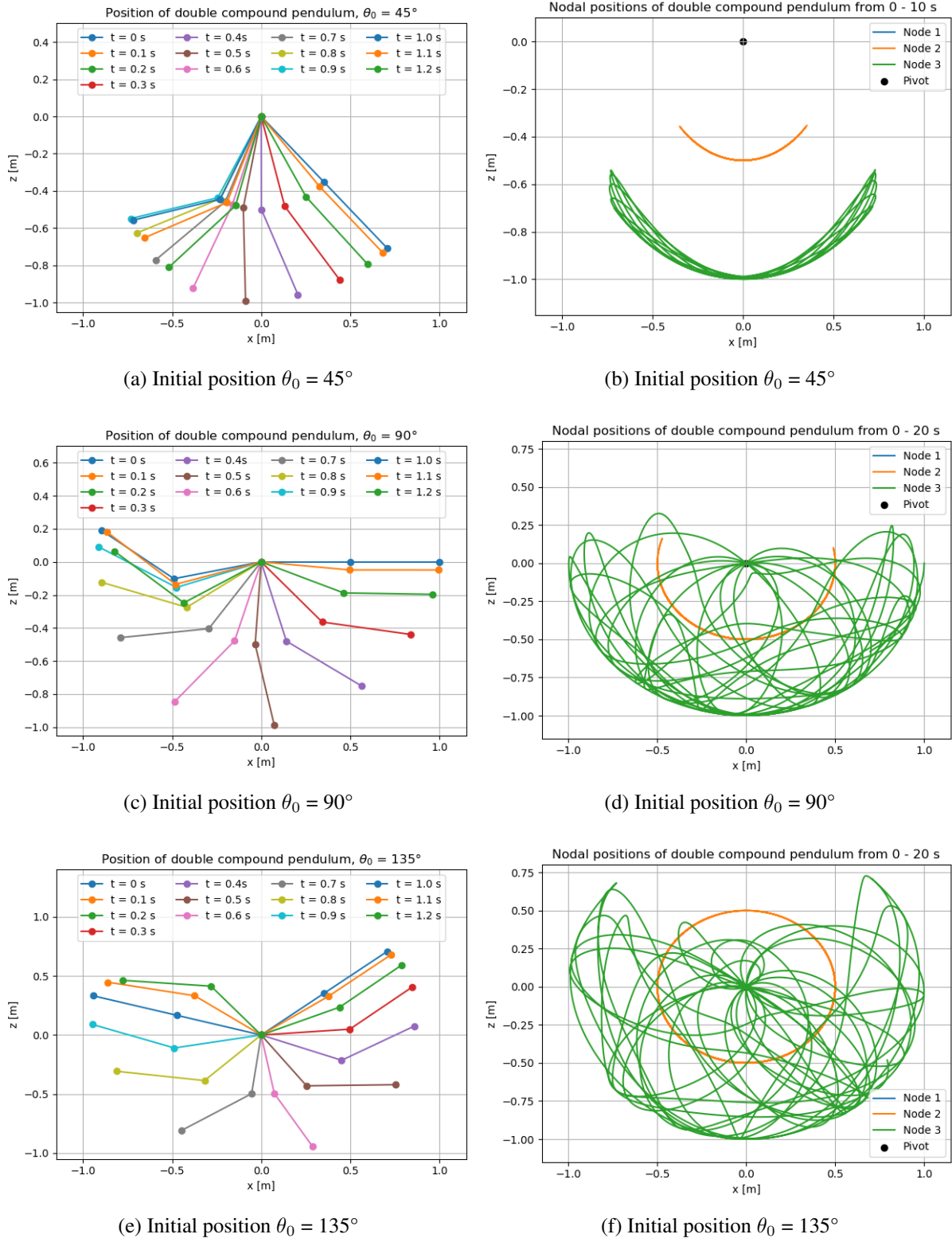
Figure E.3: **Left-hand side:** Position in time during first second of simulation with increments 0.1 $[s]$. **Right-hand side:** Nodal position in time for complete simulation of 0 - 20 $[s]$. Double rigid compound pendulum with point masses of 1 $[kg]$ and changing initial position. Simulation with time step $dt = 10^{-4}$ $[s]$.

E.1.4 Compound flexible pendulum

(a) Position in time from 0-1 [s]

(b) Vertical tip displacement
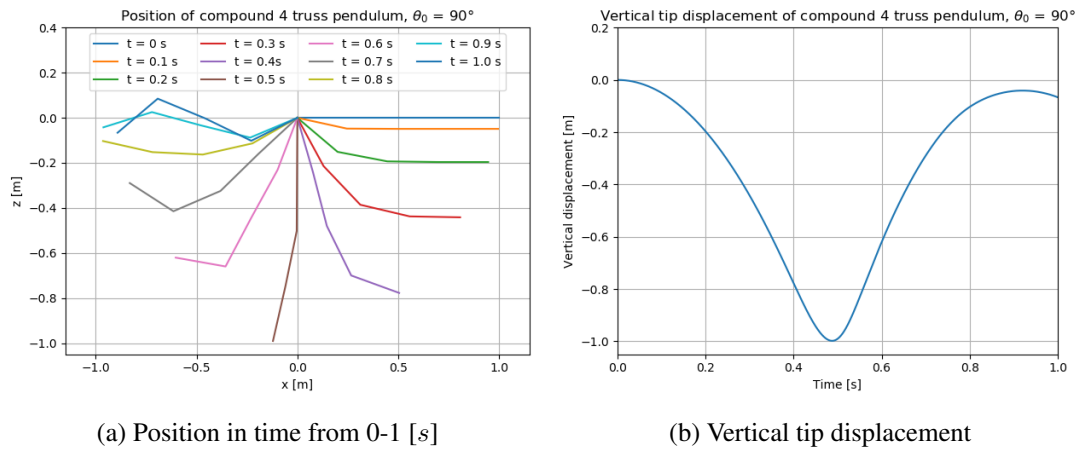
Figure E.4: Position in time from 0 - 1 [s] and vertical tip displacement of compound flexible pendulum with uniformly distributed mass. Modelled with 4 trusses. Initial position $\theta_0 = 90°$. It is seen that the tip bending is less of a problem with fewer truss elements, but the general behaviour is not as well modelled as for 20 trusses.

Appendix F

Additional experimental results

F.1 Regular wave results

F.1.1 Vertical RAOs
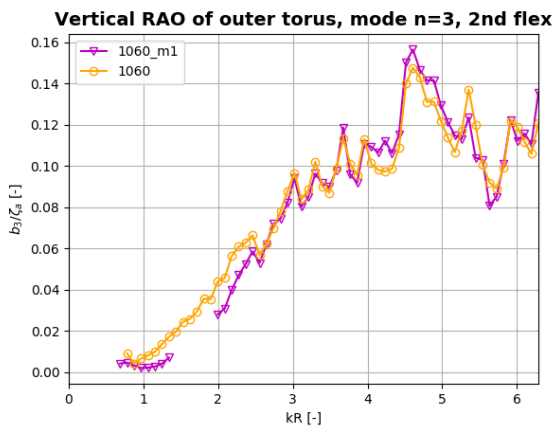
(a) Steepness $H/\lambda = 1/60$
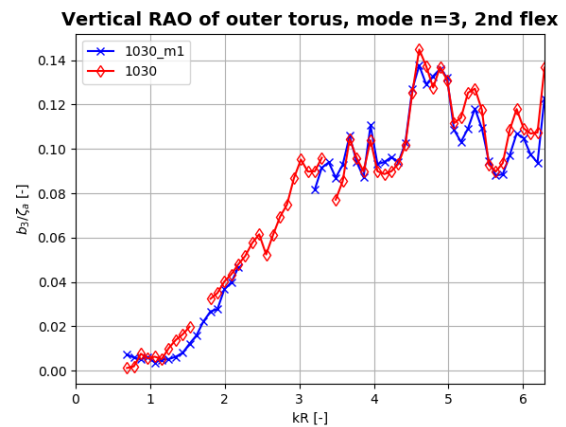
(b) Steepness $H/\lambda = 1/30$

Figure F.1: RAO for the outermost torus of 2$^{\text{nd}}$ flexible (vertical direction, mode 3). Comparing model with and without membrane. $m1$ signifies the first membrane multi-torus model. 1060 and 1030 signify wave steepnesses $H/\lambda = 1/60$ and $H/\lambda = 1/30$ respectively.
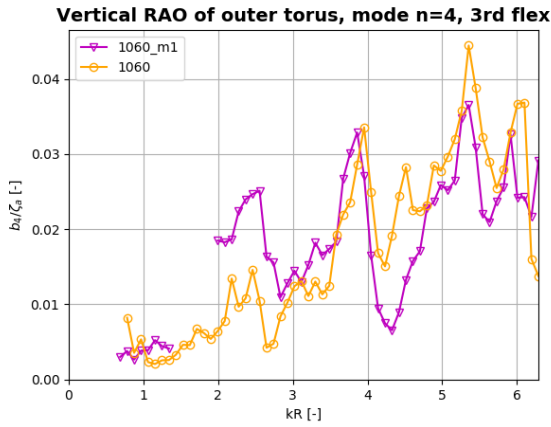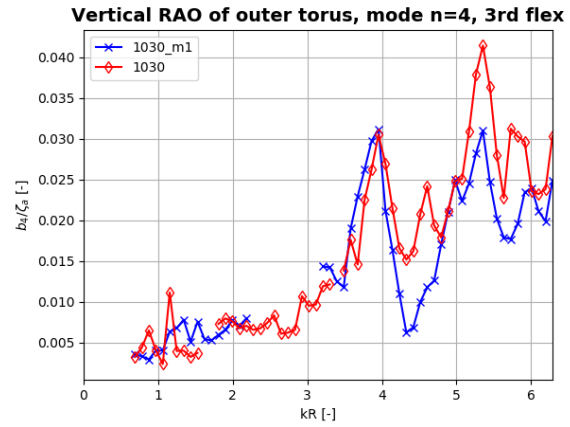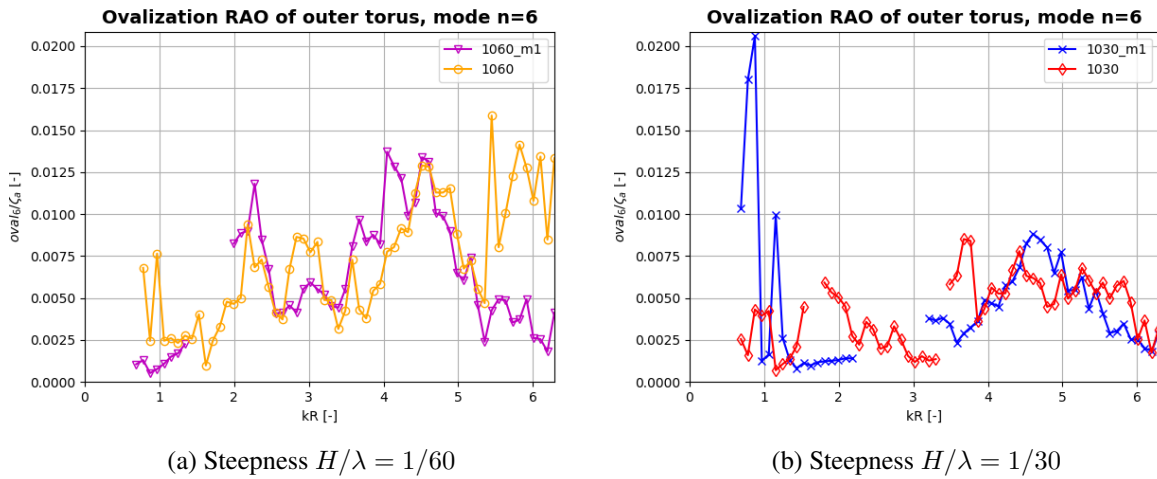
(a) Steepness $H/\lambda = 1/60$ (b) Steepness $H/\lambda = 1/30$

Figure F.2: RAO for the outermost torus of 3rd flexible (vertical direction, mode 4). Comparing model with and without membrane. $m1$ signifies the first membrane multi-torus model. 1060 and 1030 signify wave steepnesses $H/\lambda = 1/60$ and $H/\lambda = 1/30$ respectively.
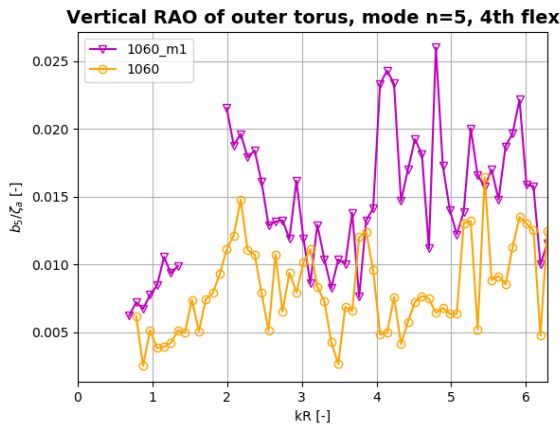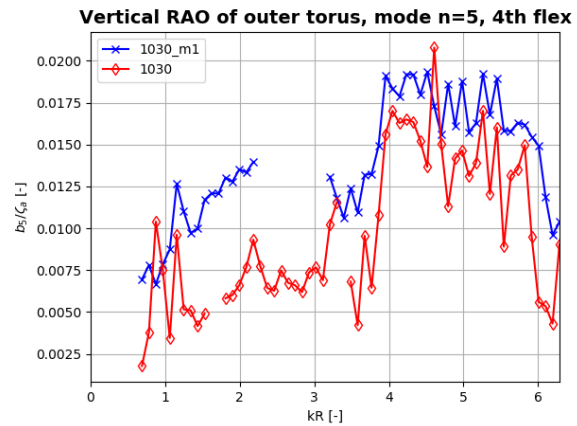
(a) Steepness $H/\lambda = 1/60$ (b) Steepness $H/\lambda = 1/30$

Figure F.3: RAO for the outermost torus of 4th flexible (vertical direction, mode 5). Comparing model with and without membrane. $m1$ signifies the first membrane multi-torus model. 1060 and 1030 signify wave steepnesses $H/\lambda = 1/60$ and $H/\lambda = 1/30$ respectively.

(a) Steepness $H/\lambda = 1/60$
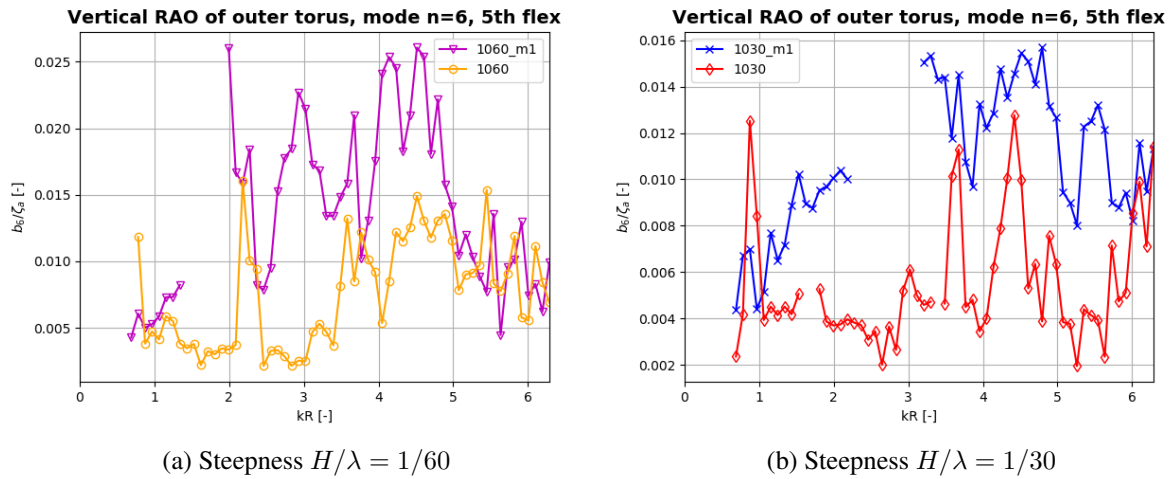
(b) Steepness $H/\lambda = 1/30$

Figure F.4: RAO for the outermost torus of 5th flexible (vertical direction, mode 6). Comparing model with and without membrane. $m1$ signifies the first membrane multi-torus model. 1060 and 1030 signify wave steepnesses $H/\lambda = 1/60$ and $H/\lambda = 1/30$ respectively.

F.1.2 Ovalization RAOs

(a) Steepness $H/\lambda = 1/60$
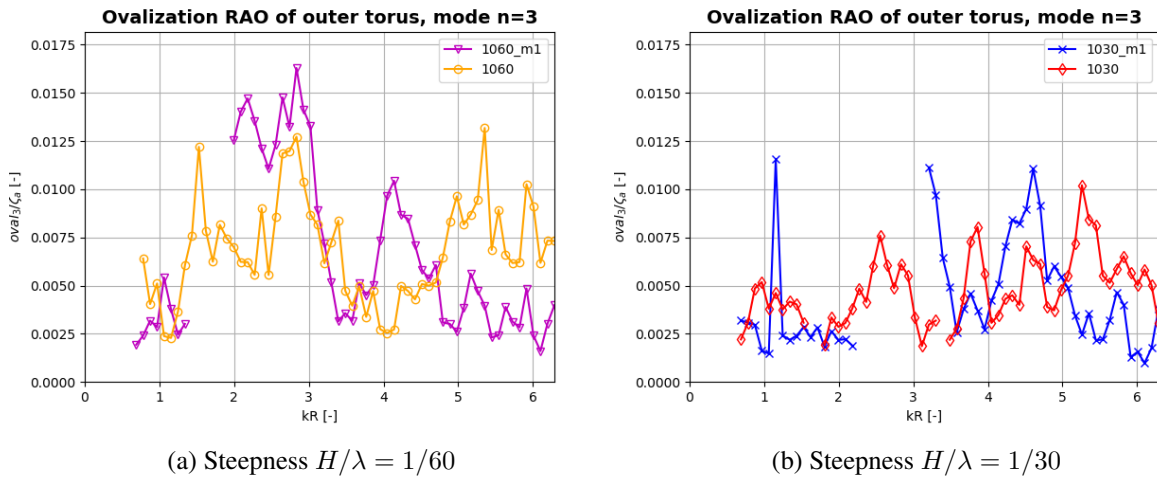
(b) Steepness $H/\lambda = 1/30$

Figure F.5: RAO for the outermost torus in ovalization mode 2, n = 3. Comparing model with and without membrane. $m1$ signifies the first membrane multi-torus model. 1060 and 1030 signify wave steepnesses $H/\lambda = 1/60$ and $H/\lambda = 1/30$ respectively.

(a) Steepness $H/\lambda = 1/60$
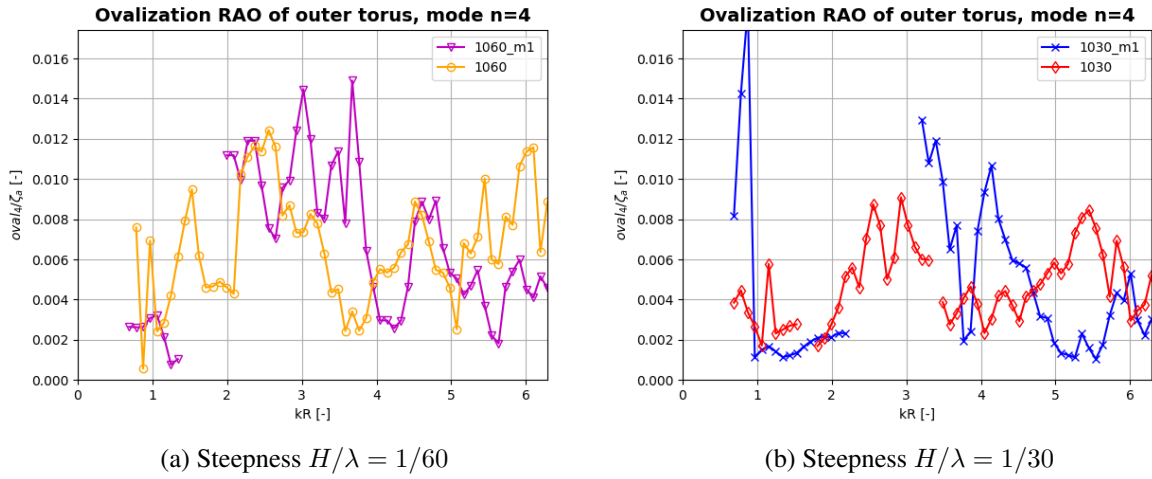
(b) Steepness $H/\lambda = 1/30$

Figure F.6: RAO for the outermost torus in ovalization mode 3, n = 4. Comparing model with and without membrane. $m1$ signifies the first membrane multi-torus model. 1060 and 1030 signify wave steepnesses $H/\lambda = 1/60$ and $H/\lambda = 1/30$ respectively.

(a) Steepness $H/\lambda = 1/60$
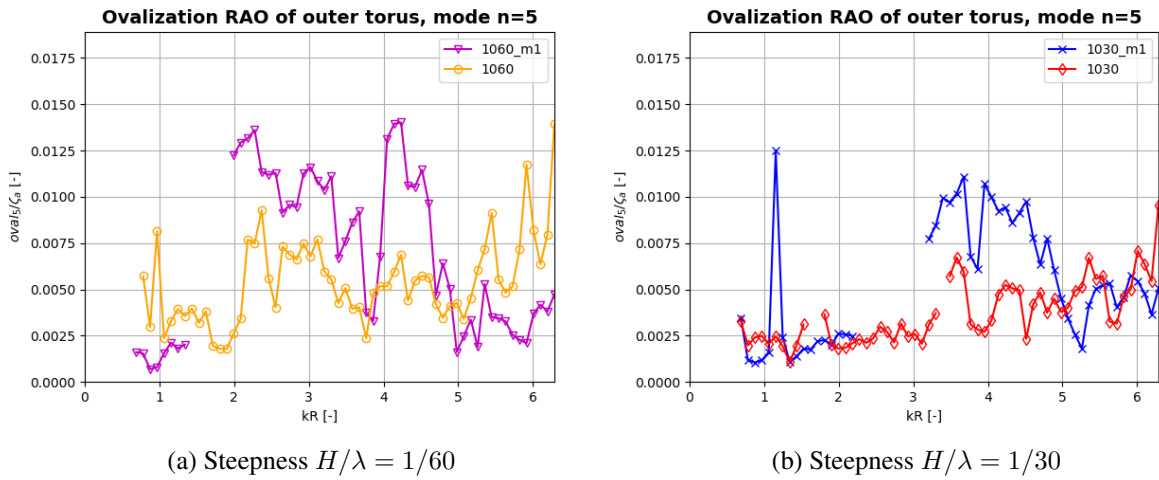
(b) Steepness $H/\lambda = 1/30$

Figure F.7: RAO for the outermost torus in ovalization mode 4, n = 5. Comparing model with and without membrane. $m1$ signifies the first membrane multi-torus model. 1060 and 1030 signify wave steepnesses $H/\lambda = 1/60$ and $H/\lambda = 1/30$ respectively.

(a) Steepness $H/\lambda = 1/60$ (b) Steepness $H/\lambda = 1/30$

Figure F.8: RAO for the outermost torus in ovalization mode 5, n = 6. Comparing model with and without membrane. $m1$ signifies the first membrane multi-torus model. 1060 and 1030 signify wave steepnesses $H/\lambda = 1/60$ and $H/\lambda = 1/30$ respectively.

F.2 Irregular wave results

F.2.1 Wave spectra

(a) No membrane   (b) With membrane
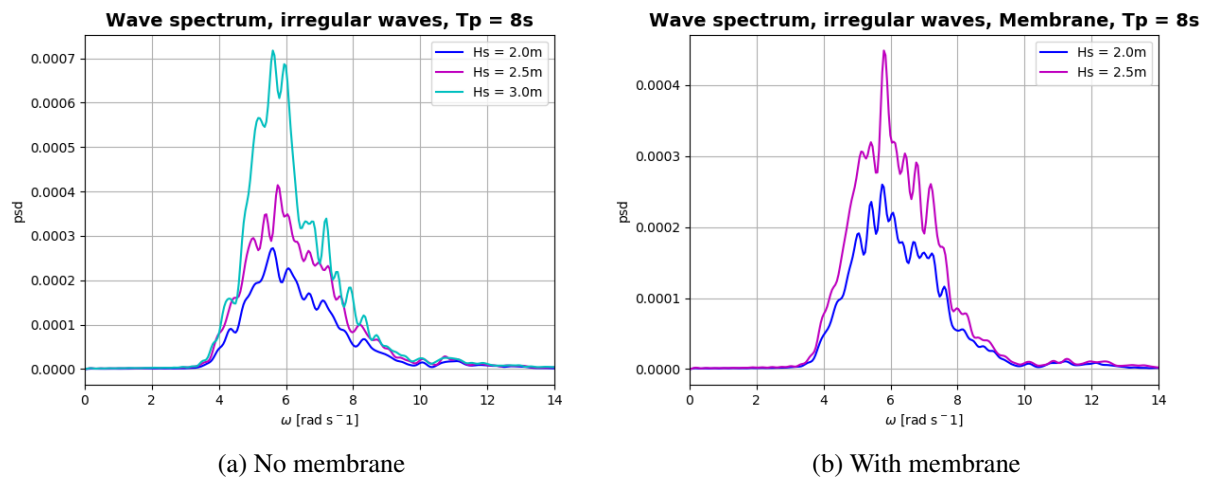
Figure F.9: The wave spectra from the tests with $T_p = 8$s and $H_s = 2.0$m, 2.5m and 3.0m are presented for the models with and without membrane. The largest H_s test with membrane suffered from measuring errors due to the Qualisys system falling out, and is therefore excluded from the results.

(a) No membrane   (b) With membrane
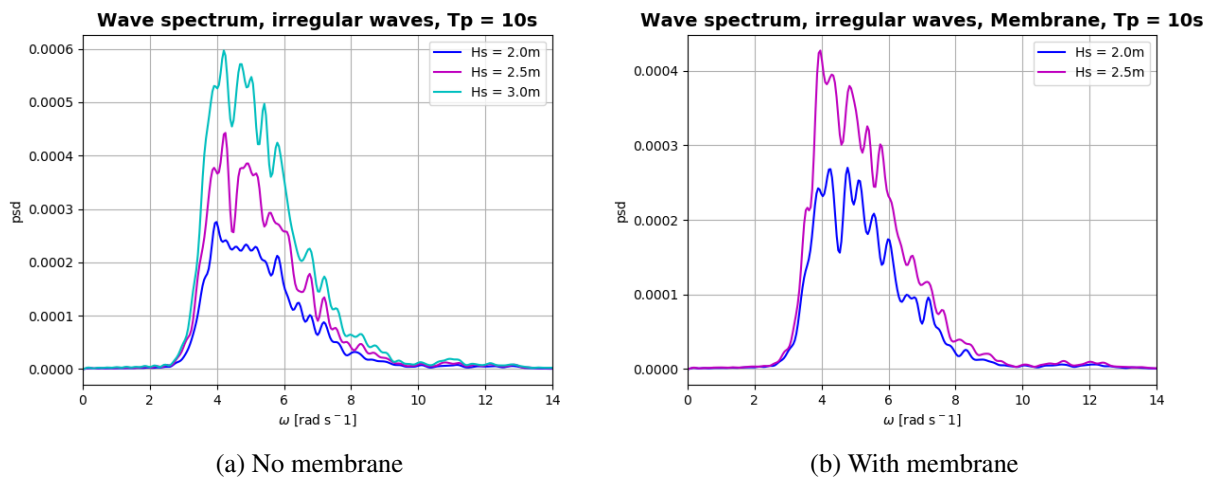
Figure F.10: The wave spectra from the tests with T_p = 10s and H_s = 2.0m, 2.5m and 3.0m are presented for the models with and without membrane. The largest H_s test with membrane suffered from measuring errors due to the Qualisys system falling out, and is therefore excluded from the results.

(a) No membrane   (b) With membrane
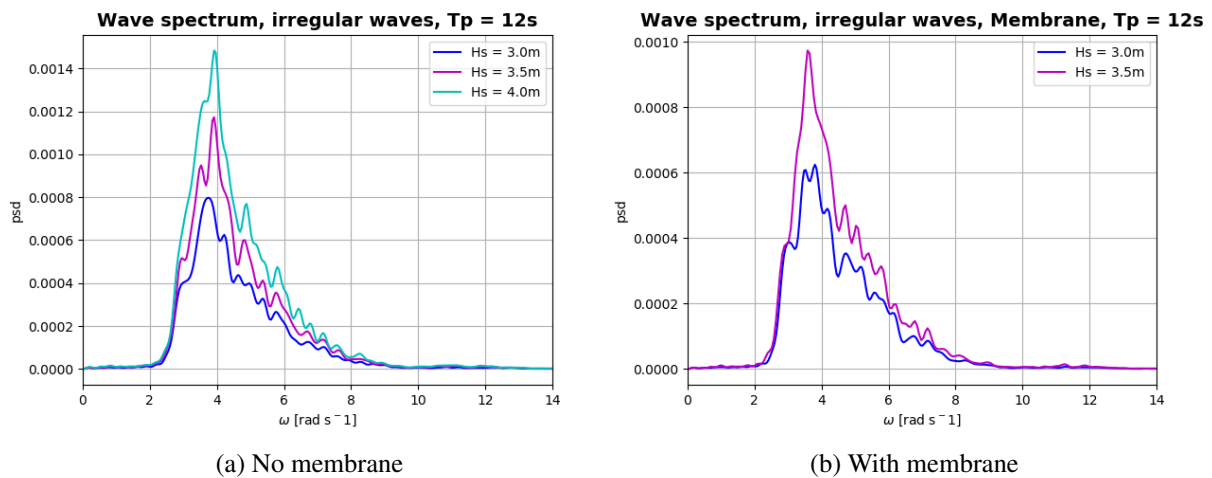
Figure F.11: The wave spectra from the tests with T_p = 12s and H_s = 3.0m, 3.5m and 4.0m are presented for the models with and without membrane. The largest H_s test with membrane suffered from measuring errors due to the Qualisys system falling out, and is therefore excluded from the results.

F.2.2 Response spectra
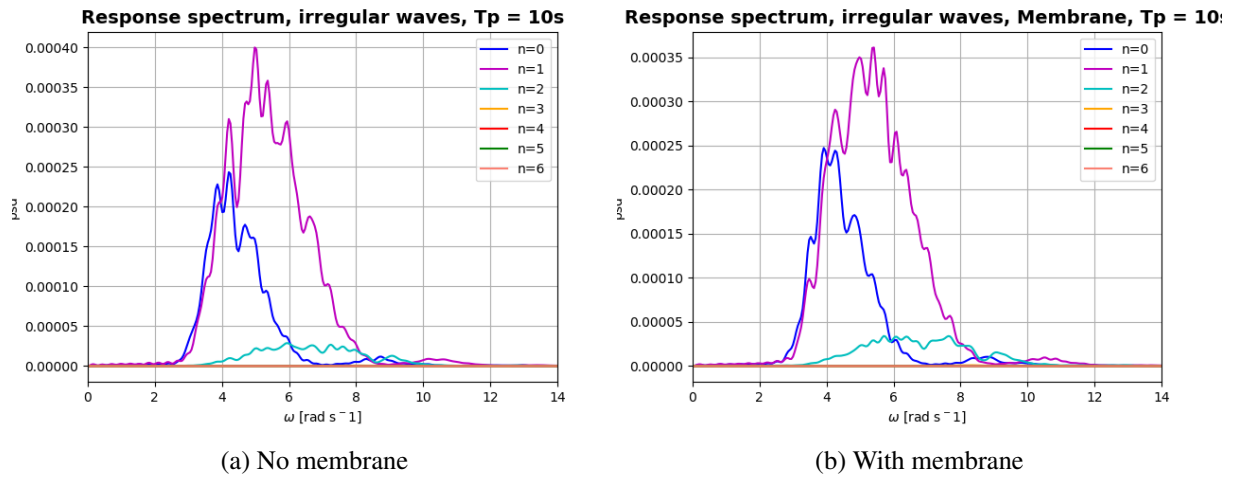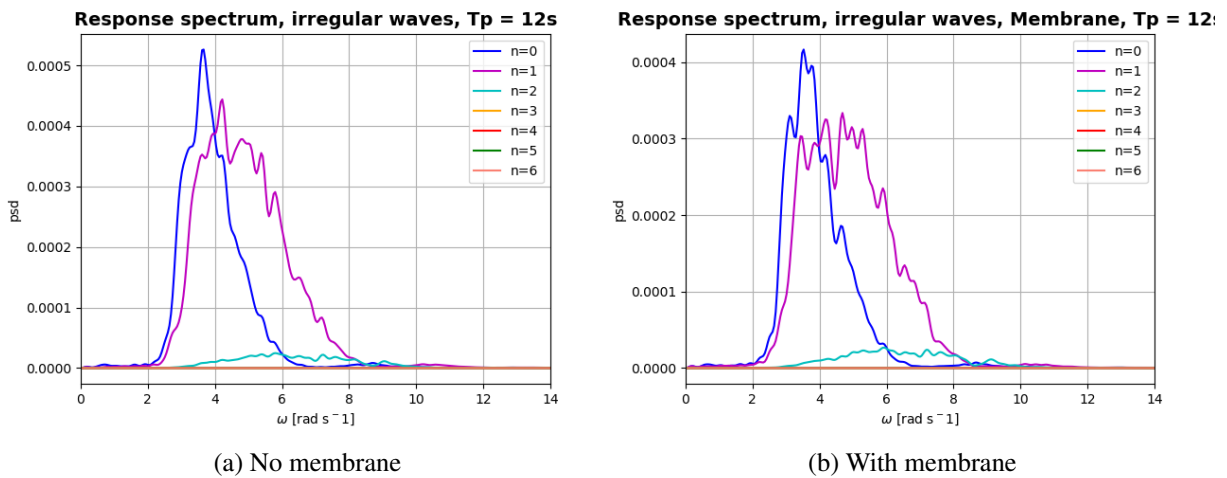
T_p = **6.0s**

(a) No membrane
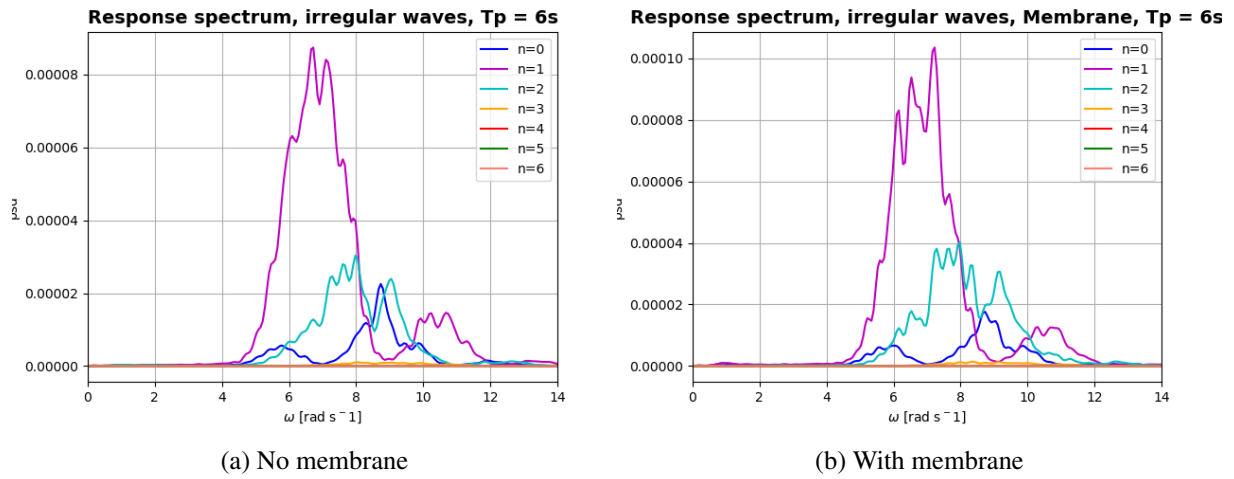
(b) With membrane

Figure F.12: Modal response spectra for mode 0-6 from irregular wave tests with T_p = 6s and H_s = 1.5m are presented in the figure for the model with and without membrane. Remark that the two vertical axis do not keep the same scale.
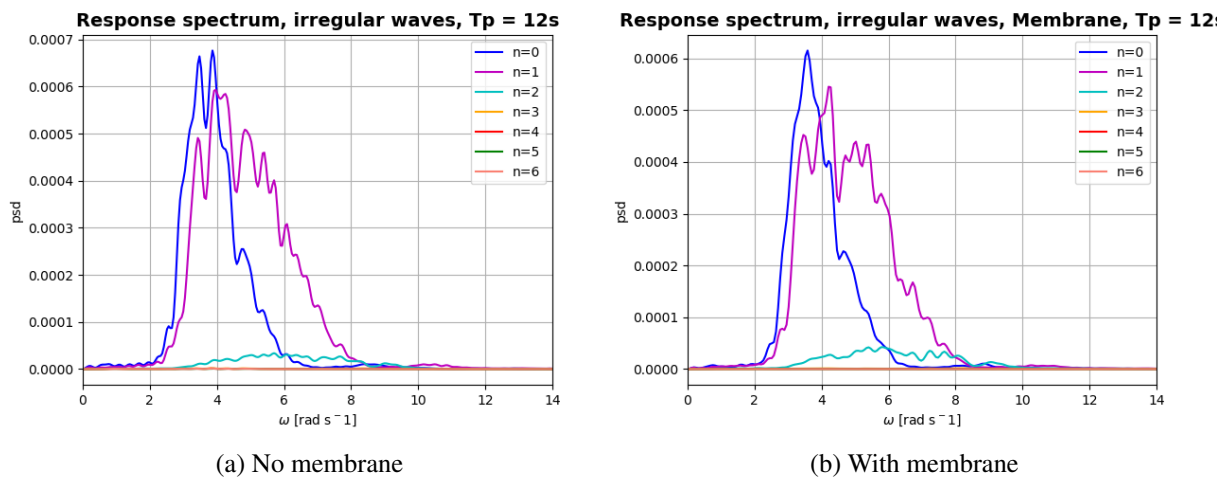
T_p = **8.0s**

(a) No membrane
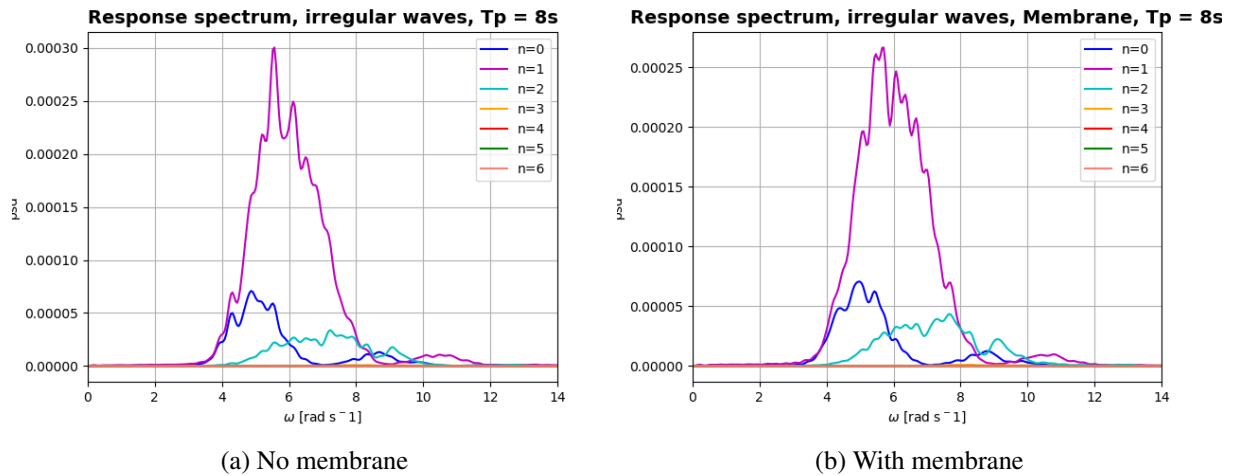
(b) With membrane

Figure F.13: Modal response spectra for mode 0-6 from irregular wave tests with T_p = 8s and H_s = 2.0m are presented in the figure for the model with and without membrane. Remark that the two vertical axis do not keep the same scale.

(a) No membrane
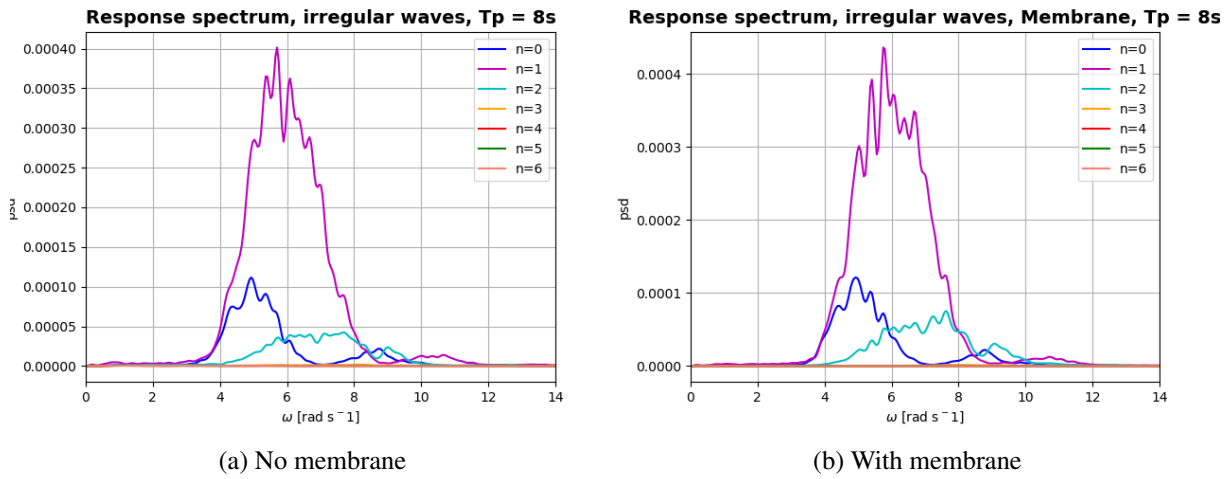
(b) With membrane

Figure F.14: Modal response spectra for mode 0-6 from irregular wave tests with T_p = 8s and H_s = 2.5m are presented in the figure for the model with and without membrane. Remark that the two vertical axis do not keep the same scale.

T_p = 10.0s

(a) No membrane
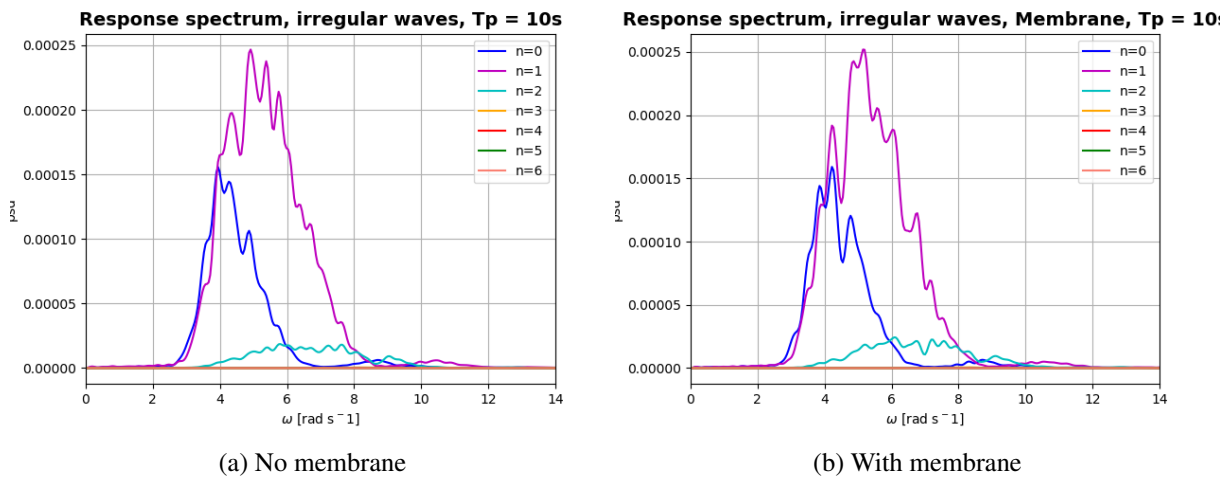
(b) With membrane

Figure F.15: Modal response spectra for mode 0-6 from irregular wave tests with T_p = 10s and H_s = 2.0m are presented in the figure for the model with and without membrane. Remark that the two vertical axis do not keep the same scale.

(a) No membrane

(b) With membrane

Figure F.16: Modal response spectra for mode 0-6 from irregular wave tests with T_p = 10s and H_s = 2.5m are presented in the figure for the model with and without membrane. Remark that the two vertical axis do not keep the same scale.

T_p = 12.0s

(a) No membrane

(b) With membrane

Figure F.17: Modal response spectra for mode 0-6 from irregular wave tests with T_p = 12s and H_s = 3.0m are presented in the figure for the model with and without membrane. Remark that the two vertical axis do not keep the same scale.

(a) No membrane

(b) With membrane

Figure F.18: Modal response spectra for mode 0-6 from irregular wave tests with T_p = 12s and H_s = 3.5m are presented in the figure for the model with and without membrane. Remark that the two vertical axis do not keep the same scale.

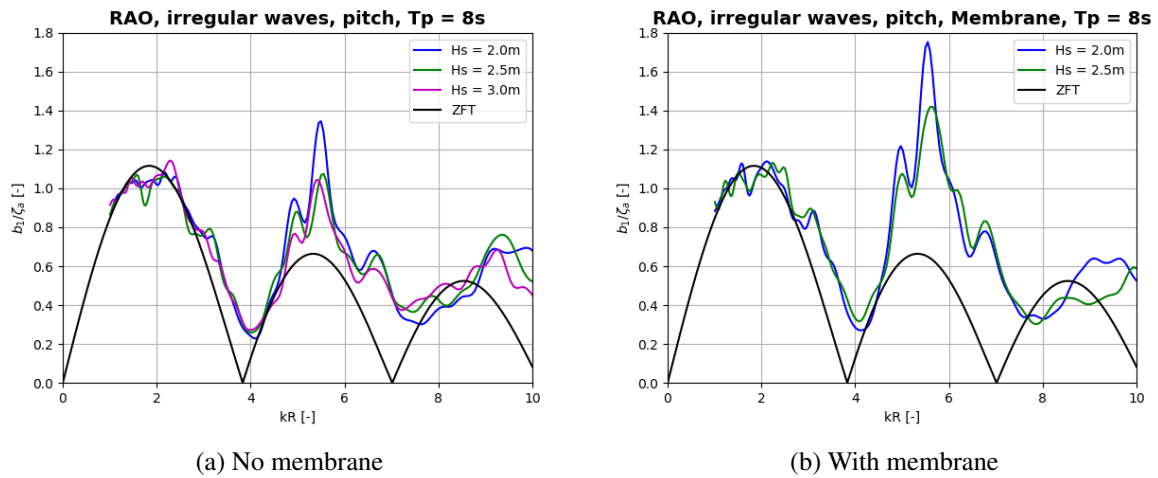## F.2.3 Heave irregular RAO

(a) No membrane
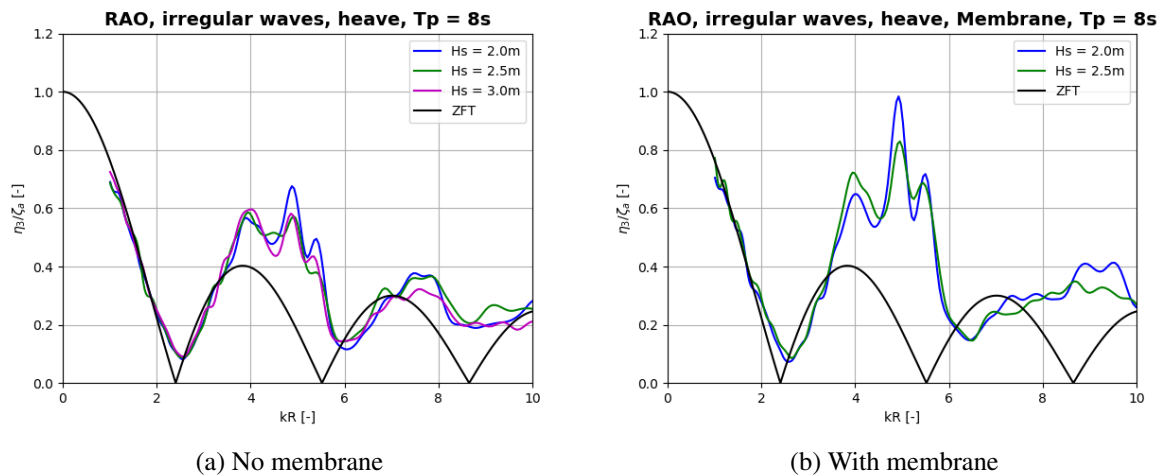
(b) With membrane

Figure F.19: The heave irregular RAO for tests with T_p = 8s and H_s = 2.0m, 2.5m, and 3.0m are presented in this figure, both for the model with and without membrane. The largest H_s test with membrane suffered from measuring errors due to the Qualisys system falling out, and is therefore excluded from the results.

(a) No membrane
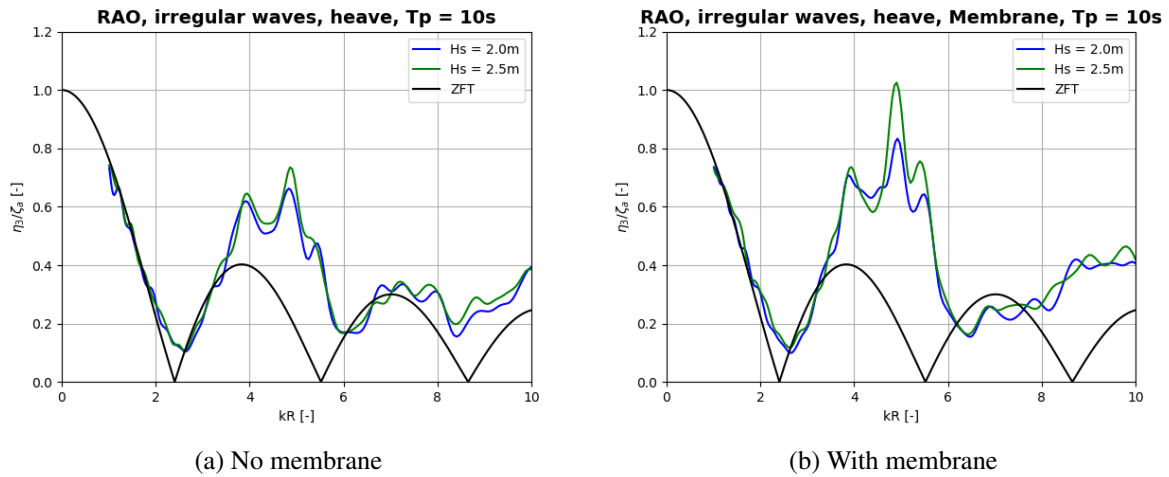
(b) With membrane

Figure F.20: The heave irregular RAO for tests with T_p = 10s and H_s = 2.0m, 2.5m and 3.0m are presented in this figure, both for the model with and without membrane. The largest H_s test with membrane suffered from measuring errors due to the Qualisys system falling out, and is therefore excluded from the results.
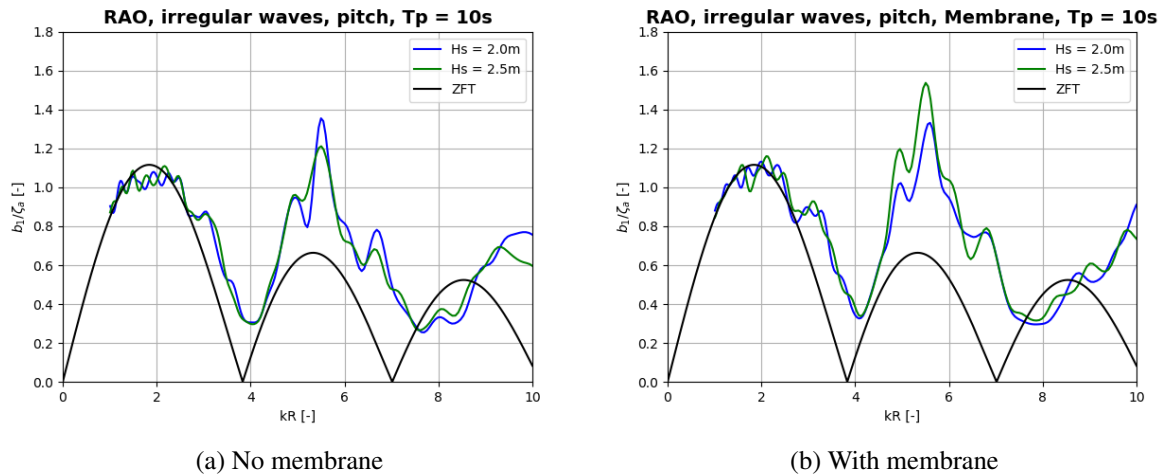

(a) No membrane
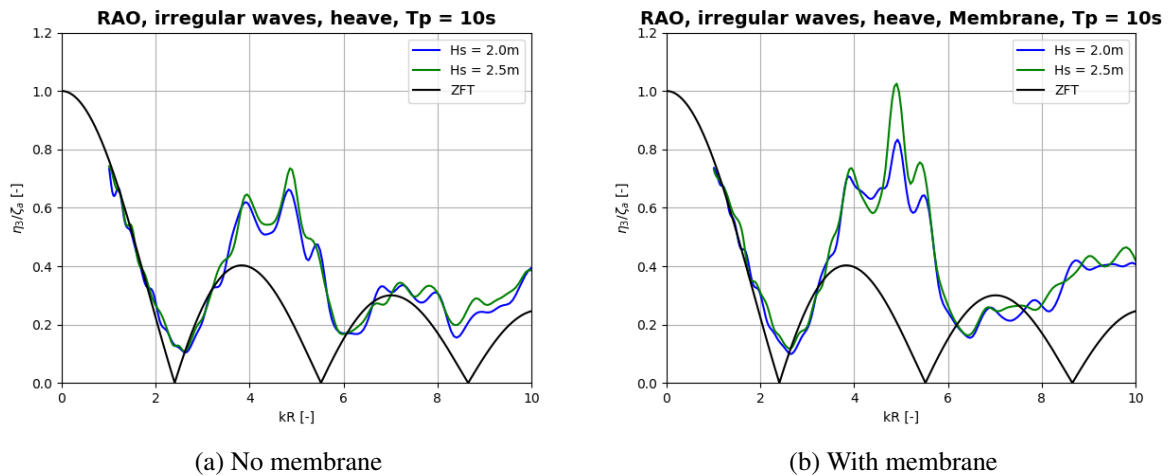
(b) With membrane

Figure F.21: The heave irregular RAO for tests with T_p = 12s and H_s = 3.0m, 3.5m and 4.0m are presented in this figure, both for the model with and without membrane. The largest H_s test with membrane suffered from measuring errors due to the Qualisys system falling out, and is therefore excluded from the results.
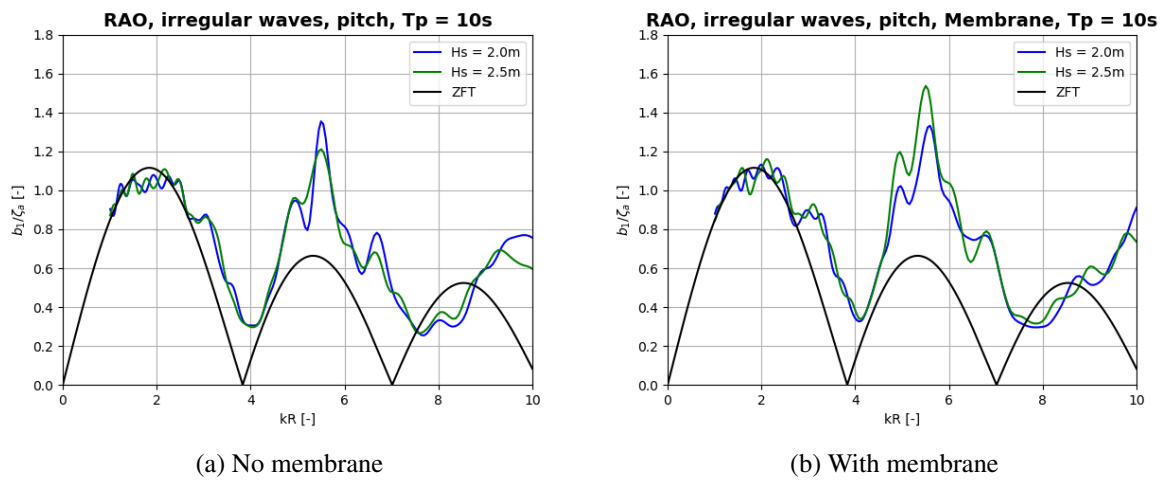
F.2.4   Pitch irregular RAO

(a) No membrane   (b) With membrane

Figure F.22: The pitch irregular RAO for tests with T_p = 8s and H_s = 2.0m, 2.5m, and 3.0m are presented in this figure, both for the model with and without membrane. The largest H_s test with membrane suffered from measuring errors due to the Qualisys system falling out, and is therefore excluded from the results.

(a) No membrane   (b) With membrane

Figure F.23: The pitch irregular RAO for tests with T_p = 10s and H_s = 2.0m, 2.5m and 3.0m are presented in this figure, both for the model with and without membrane. The largest H_s test with membrane suffered from measuring errors due to the Qualisys system falling out, and is therefore excluded from the results.

(a) No membrane (b) With membrane

Figure F.24: The pitch irregular RAO for tests with T_p = 12s and H_s = 3.0m, 3.5m and 4.0m are presented in this figure, both for the model with and without membrane. The largest H_s test with membrane suffered from measuring errors due to the Qualisys system falling out, and is therefore excluded from the results.
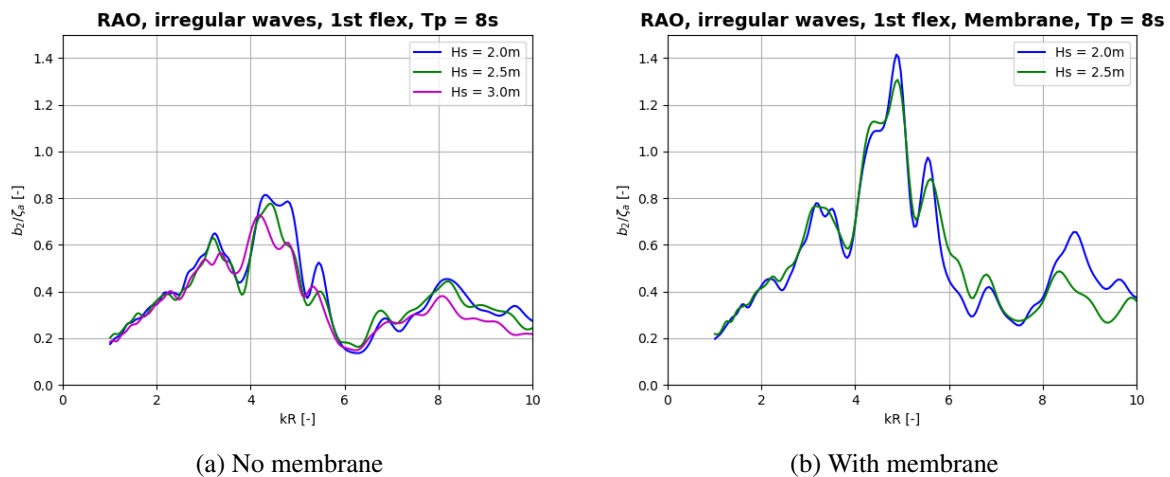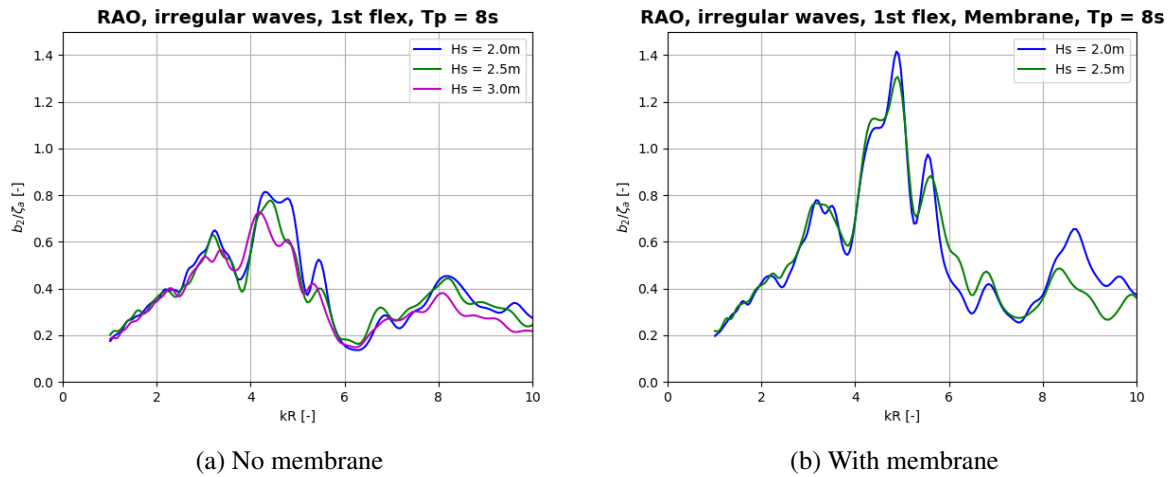
F.2.5 First flexible irregular RAO

(a) No membrane (b) With membrane

Figure F.25: The 1st flexible irregular RAO for tests with T_p = 6s and H_s = 1.0m, 1.5m,2.0m and 2.5m are presented in this figure, both for the model with and without membrane. The largest H_s test with membrane suffered from measuring errors due to the Qualisys system falling out, and is therefore excluded from the results.
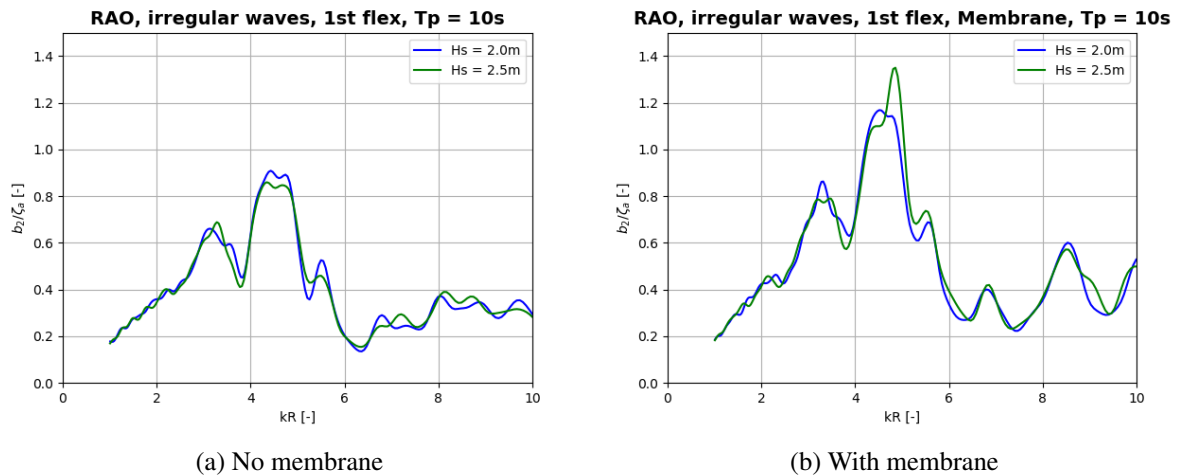
(a) No membrane

(b) With membrane

Figure F.26: The 1st flexible irregular RAO for tests with $T_p = 8$s and $H_s = 2.0$m, 2.5m, and 3.0m are presented in this figure, both for the model with and without membrane. The largest H_s test with membrane suffered from measuring errors due to the Qualisys system falling out, and is therefore excluded from the results.
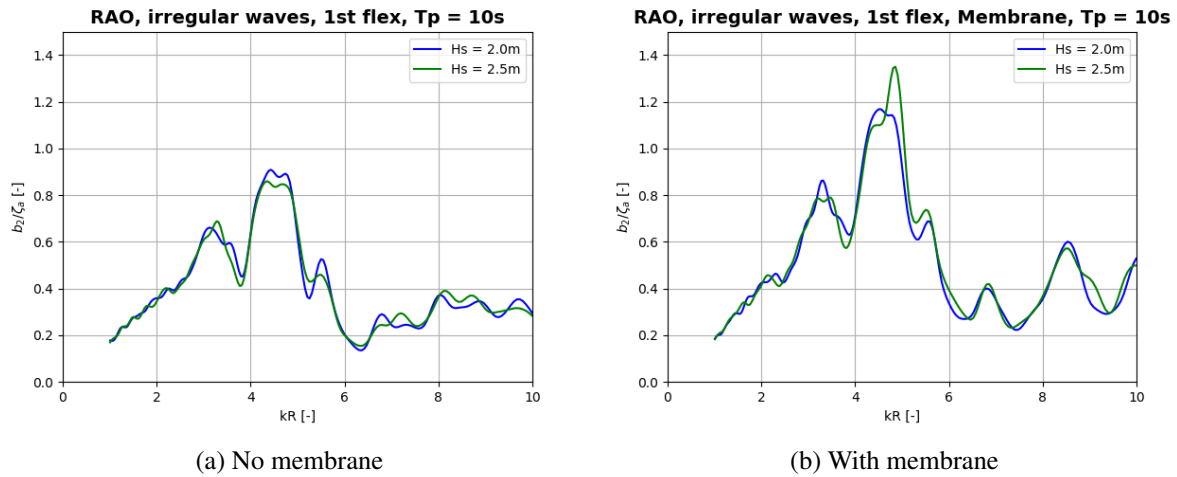

(a) No membrane

(b) With membrane

Figure F.27: The 1st flexible irregular RAO for tests with $T_p = 10$s and $H_s = 2.0$m, 2.5m and 3.0m are presented in this figure, both for the model with and without membrane. The largest H_s test with membrane suffered from measuring errors due to the Qualisys system falling out, and is therefore excluded from the results.

(a) No membrane

(b) With membrane

Figure F.28: The 1st flexible irregular RAO for tests with T_p = 12s and H_s = 3.0m, 3.5m and 4.0m are presented in this figure, both for the model with and without membrane. The largest H_s test with membrane suffered from measuring errors due to the Qualisys system falling out, and is therefore excluded from the results.
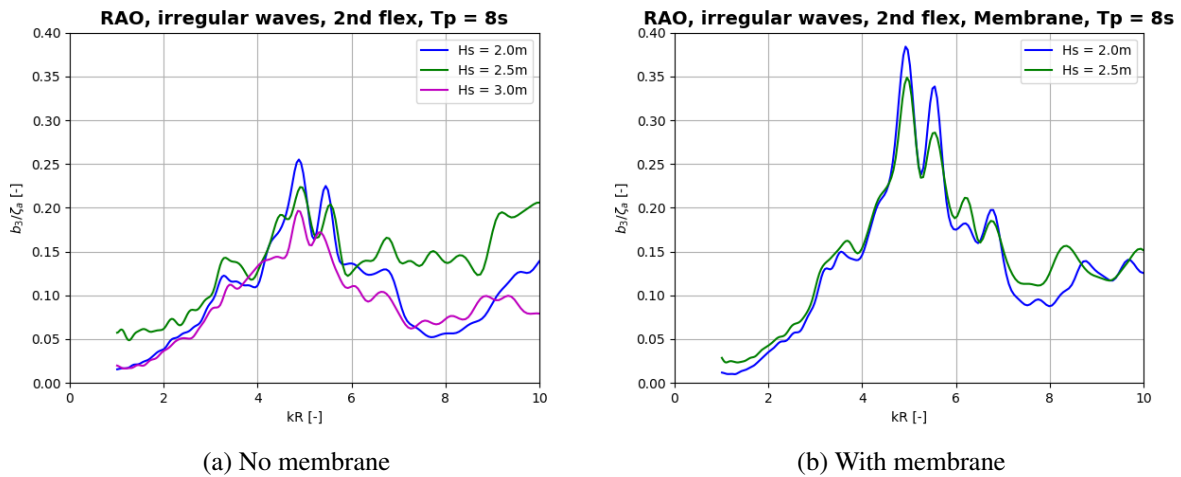
F.2.6   Second flexible irregular RAO

(a) No membrane

(b) With membrane

Figure F.29: The 2nd flexible irregular RAO for tests with T_p = 6s and H_s = 1.0m, 1.5m,2.0m and 2.5m are presented in this figure, both for the model with and without membrane. The largest H_s test with membrane suffered from measuring errors due to the Qualisys system falling out, and is therefore excluded from the results.
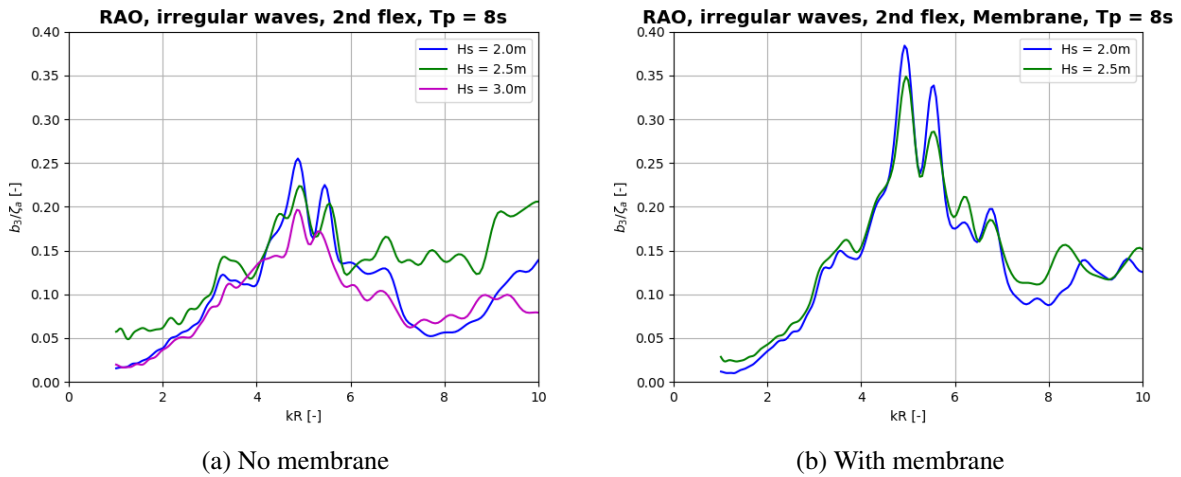
(a) No membrane

(b) With membrane

Figure F.30: The 2nd flexible irregular RAO for tests with T_p = 8s and H_s = 2.0m, 2.5m, and 3.0m are presented in this figure, both for the model with and without membrane. The largest H_s test with membrane suffered from measuring errors due to the Qualisys system falling out, and is therefore excluded from the results.
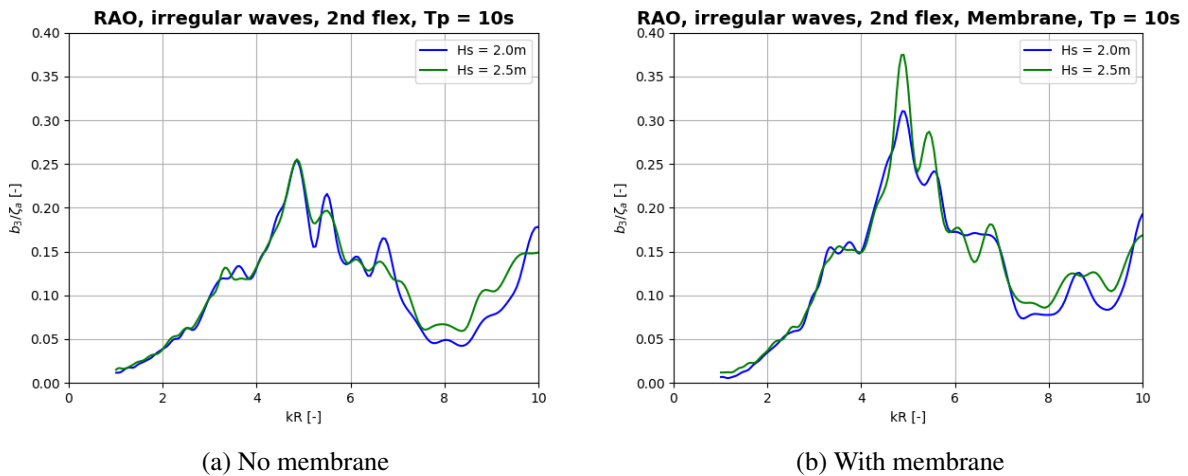

(a) No membrane

(b) With membrane

Figure F.31: The 2nd flexible irregular RAO for tests with T_p = 10s and H_s = 2.0m, 2.5m and 3.0m are presented in this figure, both for the model with and without membrane. The largest H_s test with membrane suffered from measuring errors due to the Qualisys system falling out, and is therefore excluded from the results.
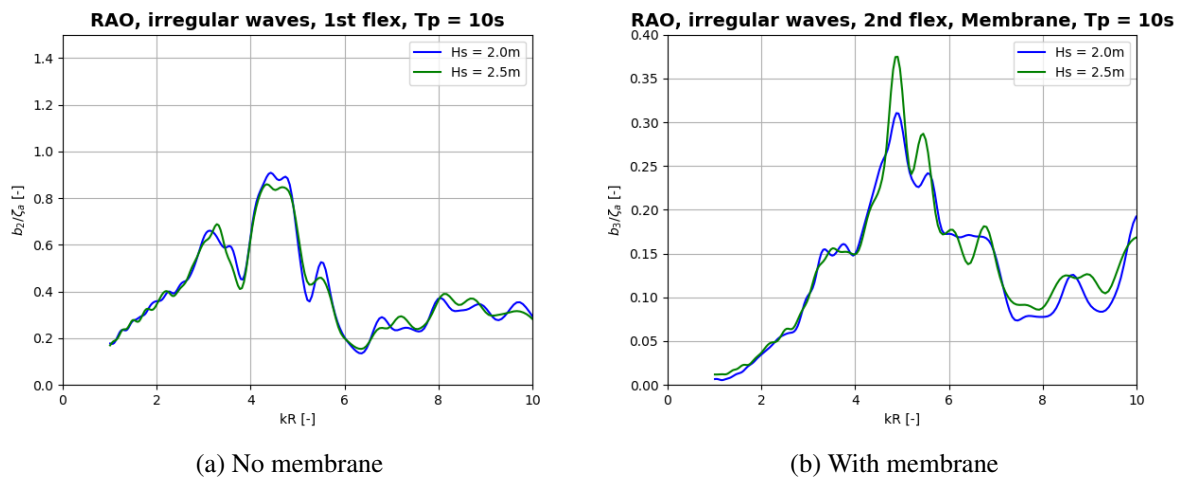
(a) No membrane

(b) With membrane

Figure F.32: The 2nd flexible irregular RAO for tests with $T_p = 12$s and $H_s = 3.0$m, 3.5m and 4.0m are presented in this figure, both for the model with and without membrane. The largest H_s test with membrane suffered from measuring errors due to the Qualisys system falling out, and is therefore excluded from the results.